

**Austenite decomposition in the coarse grain heat affected zone of
X80 line pipe steel**

by

Sabyasachi Roy

B.Tech., Indian Institute of Technology, Kharagpur, 2011

A THESIS SUBMITTED IN PARTIAL FULFILLMENT OF
THE REQUIREMENTS FOR THE DEGREE OF

MASTER OF APPLIED SCIENCE

in

THE FACULTY OF GRADUATE AND POSTDOCTORAL STUDIES
(MATERIALS ENGINEERING)

THE UNIVERSITY OF BRITISH COLUMBIA

(Vancouver)

September 2020

© Sabyasachi Roy, 2020

The following individuals certify that they have read, and recommend to the Faculty of Graduate and Postdoctoral Studies for acceptance, a thesis entitled:

Austenite decomposition in the coarse grain heat affected zone of X80 line pipe steel

submitted by Sabyasachi Roy in partial fulfillment of the requirements for

the degree of Master of Applied Science

In Materials Engineering

Examining Committee:

Prof. Matthias Militzer, Department of Materials Engineering
Supervisor

Prof. Warren J. Poole, Department of Materials Engineering
Supervisory Committee Member

Prof. Chad W. Sinclair, Department of Materials Engineering
Supervisory Committee Member

Abstract

Pipelines are used worldwide to transport oil and natural gas from their reserves to refineries and end users. Microalloyed line pipe steels are used to build these pipelines. The construction of pipelines involves welding pipes along the girth to join them. Welding of steels results in microstructure changes in the heat affected zone (HAZ). The coarse grain heat affected zone (CGHAZ), closest to the weld pool, experiences temperatures close to the melting point and is regarded as a potential region of lower toughness.

In the present work, austenite decomposition under continuous cooling conditions has been studied for simulated CGHAZ conditions in three different line pipe steels. Bulk samples were heat treated in a Gleeble 3500 thermo-mechanical simulator to replicate the austenite microstructure of the CGHAZ and subsequent cooling ranging from 3 to 100°C/s to simulate welding processes with different heat inputs. The investigated laboratory steels had systematically varied carbon and chromium contents. An increase in carbon content from 0.035 wt% to 0.061 wt% resulted in a reduction of the transformation start temperature by approximately 10°C at 3°C/s to 50°C at 100°C/s cooling rate. Further on, an increase in the chromium content from a residual amount to 0.24 wt% reduced the transformation temperature modestly by about 10°C for all cooling rates. Microstructure characterization and hardness testing confirmed that lower transformation temperatures are associated with finer bainitic microstructures and higher hardness values. Based on the experimental results a phenomenological model has been proposed to predict the transformation kinetics, microstructure and hardness as a function of cooling rate, and steel chemistry in terms of C and Cr content.

Lay Summary

Oil and natural gas remain important resources to meet global energy requirements. Pipelines are the safest, cost-effective, and efficient mode to transport oil and gas. The construction of pipelines involves welding of pipe segments, which results in the steel adjacent to the weld experiencing a rapid high temperature treatment. This leads to the formation of the heat affected zone (HAZ), which has different structures and properties compared to the as-rolled line pipe steel. Furthermore, different steel makers may use somewhat different steel chemistries for otherwise the same steel grade. Therefore, it is important to evaluate the HAZ properties as a function of steel chemistry. The present study deals with systematic laboratory simulations to determine the effect of two important alloying elements, carbon and chromium, on HAZ structures and properties. The knowledge gained from this work will help in designing line pipe steels with improved HAZ properties and increased safety specifications.

Preface

All research work including experimental design, heat treatment, metallography, hardness measurement, thermodynamic calculation, analysis and interpretation of the data and writing the thesis were carried out at the Department of Materials Engineering at The University of British Columbia, Vancouver by the author under the supervision of Professor Matthias Militzer.

Samples were machined at the UBC Machine Shop in the Materials Engineering department, from steels that were cast and rolled at CanmetMATERIALS in Hamilton, Ontario. The Gleeble experiments were conducted by the author with training from Brian Tran. Thermodynamic calculations presented in Chapters 4 and 6 were carried out using TCFE7 database in Thermo-Calc software.

Table of Contents

Abstract.....	iii
Lay Summary	iv
Preface.....	v
Table of Contents	vi
List of Tables	ix
List of Figures.....	x
List of Symbols	xiv
List of Abbreviations	xvi
Acknowledgements	xviii
Dedication	xix
Chapter 1: Introduction	1
Chapter 2: Literature review	4
2.1 Line pipe steels	4
2.1.1 Introduction.....	4
2.1.2 Classification of line pipe steels	4
2.1.3 Overview of line pipe steel chemistry	5
2.1.4 Welding of line pipe steel	8
2.2 The heat affected zone	10
2.2.1 HAZ formation.....	9
2.2.2 Relevance of the coarse grain heat affected zone	12
2.3 Continuous cooling transformation of austenite	15

2.3.1	Polygonal ferrite and pearlite.....	15
2.3.2	Irregular ferrite.....	16
2.3.3	Bainite.....	16
2.3.3.1	Orientation relationship (OR) between product and parent austenite.....	18
2.3.4	Martensite	21
2.3.5	Martensite/Austenite constituent (M/A)	21
2.4	Microstructure modelling.....	22
Chapter 3: Scope and Objectives.....		27
Chapter 4: Materials and experimental methodology		28
4.1	Materials	28
4.2	Continuous cooling transformation tests	29
4.2.1	Thermal simulations.....	29
4.2.2	Thermal cycles	31
4.2.3	Dilatometry	32
4.3	Microstructure characterization	34
4.3.1	Sample preparation	34
4.3.2	Optical microscopy imaging.....	35
4.3.3	Microstructure imaging using Electron Backscattered Diffraction	36
4.3.4	Hardness measurement	37
4.4	Modelling.....	38
Chapter 5: Experimental results and discussion		40
5.1	Continuous cooling test.....	40
5.2	Effect of cooling rate on austenite decomposition kinetics	45

5.3	Effect of carbon content on austenite decomposition kinetics.....	49
5.4	Effect of chromium content on austenite decomposition kinetics	50
5.5	Optical microstructure characterization	51
5.6	EBSD characterization of transformation products	52
5.6.1	Inverse pole figure maps	52
5.6.2	Retained austenite	54
5.6.3	Orientation relationship between parent and product phase	55
5.6.4	Spatial distribution of misorientation.....	59
5.7	Hardness.....	65
5.8	Microstructure-property relationship	66
5.9	Discussion	68
Chapter 6: Modelling		74
6.1	Introduction.....	74
6.2	Bainite start	74
6.3	Bainite growth.....	76
6.4	Structure and property calculation	80
6.5	Discussion	83
Chapter 7: Summary and Future work		85
7.1	Summary	85
7.2	Future work.....	86
Bibliography		88

List of Tables

Table 2.1: Twenty-four variants of the K-S orientation relationship and the corresponding CP group, Bain group and misorientation (Reprinted with permission [80]).....	19
Table 4.1: Chemical composition in wt. % and Ae_3 temperature of the investigated steels	28
Table 5.1: Metallographic and LUMet [57] measurement of PAGES.....	41
Table 5.2: Variability during multiple tests for same steel and thermal cycle	45
Table 5.3: Chemical composition in wt. % for the steels studied by Reichert [40] and Mandal [10]	70
Table 6.1: Bainite nucleation temperature (T_N) based on driving pressure of 400 J/mol.....	74
Table 6.2: Fit parameter to calculate the bainite start temperature.....	75
Table 6.3: Fit parameter to calculate the austenite decomposition kinetics	77

List of Figures

Figure 2.1: Schematic showing the different regions in the HAZ and the associated peak temperature during single torch weld pass, adapted from [50].....	11
Figure 2.2: Schematic showing the microstructure and thermal cycle during multipass welds, adapted from [55].....	12
Figure 2.3: Schematics showing the variant pairing within a prior austenite grain indicating frequently occurring variant pair (a) Bainite formed at high temperature (b) bainite formed at intermediate temperature (c) lath martensite formed at low temperature, each color represent a single Bain group, white and black line represent low and high angle grain boundaries respectively (Reprinted with permission [80]).....	20
Figure 4.1: Gleeble setup used for austenite decomposition tests on tubular samples	30
Figure 4.2: Tubular sample geometry used for Gleeble simulation (a) front view (b) side view.....	30
Figure 4.3: Schematic of thermal cycle to simulate austenite decomposition in CGHAZ.....	32
Figure 4.4: Schematic of dilation curve obtained during cooling of Gleeble sample.....	33
Figure 4.5: Schematic of fraction transformed as a function of temperature obtained by applying the lever rule on dilation data.....	34
Figure 5.1: Micrograph showing the prior austenite grain boundaries in a L04C08NbMoCr sample	40
Figure 5.2: Thermal cycle of 30°C/s cooling rate test (a) complete cycle, (b) during isothermal hold and (c) during cooling.....	42

Figure 5.3: Thermal cycle of 50°C/s cooling rate test (a) complete cycle, (b) during isothermal hold and (c) during cooling.....	43
Figure 5.4: Deviation of cooling rate from target cooling rate for (a) 50°C/s and (b) 100°C/s....	44
Figure 5.5: Repeat tests at 30°C/s for L06C06NbMo showing test to test variability	45
Figure 5.6: Effect of cooling rate on austenite decomposition kinetics in L06C06NbMo	46
Figure 5.7: Effect of cooling rate on transformation start temperature (5%) for the three steels.	47
Figure 5.8: Effect of cooling rate on 50% transformation temperature for the three steels	48
Figure 5.9: Effect of cooling rate on 95% transformation temperature for the three steels	48
Figure 5.10: Effect of carbon content on transformation kinetics at different cooling rates	49
Figure 5.11: Effect of chromium content on transformation kinetics at different cooling rates ..	50
Figure 5.12: Optical microstructure for L06C06NbMo at different cooling rates (a) 3°C/s, (b) 10°C/s, (c) 30°C/s and (d) 100°C/s	51
Figure 5.13: Inverse pole figure map for L06C06NbMo at different cooling rates (a) 3°C/s, (b) 10°C/s, (c) 30°C/s and (d) 100°C/s	53
Figure 5.14: Inverse pole figure map at 100°C/s for (a) L04C04NbMo and (b) L04C08NbMoCr	53
Figure 5.15: Retained austenite in L06C06NbMo at different cooling rates (a) 3°C/s, (b) 10°C/s, (c) 30°C/s and (d) 100°C/s.....	54
Figure 5.16: (a) IPF map and (b) IPF map for retained austenite, with a selected prior austenite grain shown in dotted line; (c) theoretical (001) pole figure (black circles indicating the 24 KS variants and green dots indicate the orientation of parent grain); (d) (001) pole figure of selected grain overlaid on theoretical pole figure; (e) Bain map for the selected grain. (For L04C08NbMoCr cooled at 3°C/s).....	56

Figure 5.17: Bain group maps and corresponding pole figures for L06C06NbMo cooled at (a, b) 3°C/s, (c, d) 10°C/s, (e, f) 30°C/s and (g, h) 100°C/s.....	58
Figure 5.18: Bain group maps and corresponding pole figures cooled at 100°C/s for (a, b) L04C04NbMo and (c, d) L04C08NbMoCr	59
Figure 5.19: Misorientation angle maps for L06C06NbMo at different cooling rates (a) 3°C/s, (b) 10°C/s, (c) 30°C/s and (d) 100°C/s.....	60
Figure 5.20: Misorientation angle maps at 100°C/s for (a) L04C04NbMo and (b) L04C08NbMoCr	61
Figure 5.21: Distribution of misorientation angle for the three steels at different cooling rates (a) 3°C/s, (b) 10°C/s, (c) 30°C/s and (d) 100°C/s.....	62
Figure 5.22: High angle grain boundary density in the product microstructure for the three steels at different cooling rates	63
Figure 5.23: Relation between high angle grain boundary density and transformation start temperature	64
Figure 5.24: Vickers hardness of product microstructure for the three steels at different cooling rates.....	65
Figure 5.25: Hardness related to the high angle grain boundary density of different microstructures.....	66
Figure 5.26: Relation between hardness and transformation start temperature.....	67
Figure 5.27: CCT diagram showing the transformation start (solid lines) and transformation finish (dashed lines) and hardness for the three steels. Data of previous work on similar steel by Reichert [40] is included in blue.....	71

Figure 5.28: Comparison between present work (circular markers) and previous work by Mandal [10] and Reichert [40] (triangular marker) on relation between transformation start temperature and hardness.....	73
Figure 6.1: Model prediction and experimentally measured bainite start temperature for the three steels.....	76
Figure 6.2: Comparison between experimentally measured transformation kinetics and model prediction for L04C08NbMo	79
Figure 6.3: Comparison between experimentally measured transformation kinetics and model prediction for L06C06NbMo	79
Figure 6.4: Comparison between calculated and experimentally measured 25% (square marker), 50% (circular marker) and 75% (triangular marker) transformation temperature for all three steels. L04C08NbMo, L04C08NbMoCr and L06C06NbMo shown in green, black and red, respectively	80
Figure 6.5: Comparison between experimental result and model calculation for high angle grain boundary density (dashed lines shows $0.2\mu\text{m}^{-1}$ scatter band).....	81
Figure 6.6: Comparison between experimental result and model calculation for hardness (dashed lines shows 5% scatter band).....	82

List of Symbols

A^α	Area of ferrite grain
D	Diffusivity
d_{avg}	Average diagonal length of indent
E	Activation energy
F	Force applied
f	Fraction transformed
H_v	Vickers hardness
l	Characteristic length scale
M	Interface mobility
M_0	pre-exponent factor for mobility
n	JMAK exponent
R	Universal gas constant
T	Temperature
T_5	Transformation start temperature (°C)
T_{50}	50% transformation temperature (°C)
T_{95}	95% transformation temperature (°C)
T_N	Bainite nucleation temperature (°C)
t	time
$t_{8/5}$	Cooling time from 800 to 500°C
V^α	Volume of ferrite grain
X_C	Weight % carbon

X_{Cr}	Weight % chromium
α_1 and α_2	Bainite start fit parameters
β	JMAK rate parameter
β_1 and β_2	Bainite growth fit parameters
ϕ	Cooling rate
χ	Driving pressure per unit concentration difference

List of Abbreviations

API	American Petroleum Institute
ASME	American Society of Mechanical Engineers
ASTM	American Society for Testing and Materials
BCC	Body-centered cubic
CCT	Continuous cooling transformation
CGHAZ	Coarse grain heat affected zone
CI	Confidence index
CTE	Coefficient of thermal expansion
EBSD	Electron back scattered diffraction
EQAD	Equivalent area diameter
FCC	Face-centered cubic
FGHAZ	Fine grain heat affected zone
GMAW	Gas metal arc welding
HAGB	High angle grain boundary
HAZ	Heat affected zone
ICCGHAZ	Intercritically reheated coarse grain heat affected zone
ICHAZ	Intercritical heat affected zone
IPF	Inverse pole figure
IQ	Image quality
JMAK	John-Mehl-Avrami-Kolmogorov
KS	Kurdjumov-Sachs

LAGB	Low angle grain boundary
LUMet	Laser ultrasonics in metallurgy
M/A	Martensite/Austenite
OIM	Orientation imaging microscopy
OR	Orientation relationship
PAGB	Prior austenite grain boundary
PAGS	Prior austenite grain size
RA	Retained austenite
SAW	Submerged arc welding
SCHAZ	Sub-critical heat affected zone
SEM	Scanning electron microscope
TMCP	Thermomechanical controlled processing
TRIP	Transformation induced plasticity

Acknowledgements

It is my great pleasure to thank everyone who has been a part of my M.A.Sc. journey at The University of British Columbia. Firstly, I would like to express my sincere gratitude to my supervisor, Professor Matthias Militzer, for giving me the opportunity to work with him and for his continuous support and guidance. Special thanks to Professor Warren Poole for his valuable feedback during the group meetings. I am grateful to NSERC, TC Energy and Evraz Inc. NA for their generous financial support.

Special thanks to Brian Tran for his invaluable support in the Gleeble lab. I am grateful to Heli Eunike for training me on the FEGSEM facility. I would like to thank the staff of the Materials Engineering department, especially Michelle Tierney for her continued support in all administrative matters, as well as Marlon Blom from Stores and Ross Mcleod, David Torok and Carl Ng from the Machine Shop for their continuous help.

It was a pleasure to be a part of the Microstructure group, and I thoroughly enjoyed the company of everyone in the group. I really appreciate all the help and discussions, technical or otherwise, with my officemates, Maddie, Nicolas, Sudipta, Tianbi, Mariana, Rosanne and Kaiya. I will forever cherish the coffee breaks and the endless discussions with Ayush, Hari, Naveen, Wendel, Zhuo and Sudipta. Special thanks to Jasnoor for the mini trips around Vancouver and making my stay in Vancouver memorable. I really appreciate all my friends in India, especially Aman, Ankush, Brijesh, Khushboo, Nisha, Pallavi, Prashant, Priyanka, Shekhar, Snigdha and Suprita, who were just a phone call away, round the clock.

Finally, I want to sincerely thank my family, especially my parents, my sister and my cousin, for being by my side through thick and thin.

Dedicated to my parents

Chapter 1: Introduction

Oil and natural gas are important resources to meet the energy requirements of the world. According to an International Energy Agency report, oil and natural gas contributed 31.4% and 22.9%, respectively, as global primary energy resource in 2018 [1]. It was also reported that the global demand for oil and natural gas is projected to increase by 9% and 36%, respectively, by 2040 [2]. Natural gas and crude oil amounted to 24.1% and 32.4%, respectively, of the primary energy source in Canada and together contributed 5.6% to the Canadian GDP in 2018 [3].

One of the major challenges is transportation of oil and gas from the reserves to refineries, distribution centers and the end customer. Pipelines are the safest, most cost-effective and efficient mode of oil and gas transportation. In Canada alone, there is more than 830,000 kilometers of pipelines, with approximately 100,000 kilometers of large-diameter transmission pipelines, 250,000 kilometers of small diameter gathering pipelines, 25,000 kilometers of feeder pipelines and 450,000 kilometers of distribution pipelines [4]. With a continuous increase in the demand of oil and gas, the industry is moving towards larger diameter pipelines and/or increasing the operating pressure to have higher transmission capacities. Higher strength steels are developed to minimize pipeline wall thickness, thereby reducing the construction cost. Microalloyed low carbon steels are used as line pipe steels, due to a combination of high strength, toughness and good weldability. Pipelines are frequently installed in remote and challenging regions, including the Arctic, where they have to operate safely at extreme conditions. Therefore, it is important to design the steel to withstand a wide variety of operating conditions without failure.

The construction of pipelines involves welding in the field to join pipes together. The welding process heats up the steel adjacent to the weld pool to high temperature, resulting in

changes in the structure and properties of the region. This region affected by the high temperature is called the heat affected zone (HAZ). The change in the properties of the HAZ makes it a region with low toughness; therefore, it is crucial to understand the changes in the microstructure and properties taking place in the HAZ. In addition, different welding processes have different thermal paths, which may result in differences in the final properties of the HAZ.

Pipes are fabricated to meet specific strength requirements. The same grade of steel can be achieved over a range of chemistries. Different steel producers use different alloying strategies based on their casting and rolling capabilities, thereby introducing variability in the chemistry of the pipeline. Typically, the alloying content in line pipe steels ranges from 0.03 to 0.1 wt% for carbon, up to 0.3 wt% for chromium and molybdenum, 0.03 to 0.11 wt% for niobium, 0.01 to 0.02 wt% titanium, 0 to 0.1 wt% vanadium and 1.4 to 2 wt% manganese. In addition, there can be other alloying elements, such as silicon, nickel and copper. The 2nd West East Gas Pipeline project in China used X80 grade steel with molybdenum ranging from residual to 0.25wt%, niobium between 0.095 and 0.11 wt% and carbon around 0.035 to 0.04 wt%. Manganese and silicon content were maintained at about 1.75 wt% and 0.22 wt%, respectively [5]. The differences in chemistry may affect the microstructural changes in the HAZ.

Welding of a pipeline is an important aspect in successfully transporting oil and gas over long distances. As previously discussed, welding results in microstructural changes, which affect the final mechanical properties, potentially leading to regions of lower toughness. Therefore, the welding process, the location in the HAZ and its chemistry determine the final microstructure and properties making it necessary to understand the effect of these parameters in order to improve the safety of pipelines.

In the present work, a systematic study on the effect of carbon and chromium content on microstructure and hardness in the coarse grain heat affected zone (CGHAZ) was carried out. The CGHAZ is the HAZ region closest to the weld pool, and it experiences temperatures close to the melting point of steel. Several researchers have shown that the CGHAZ can lead to failure due to its low toughness and high ductile to brittle transition temperature, which provides the motivation to carry out a systematic study into the microstructural changes occurring in this region [6–10]. This work is part of a larger ongoing project between TC Energy, Evraz NA and The University of British Columbia which attempts to develop a chemistry-sensitive model linking microstructure and properties in the HAZ during pipeline welding.

Chapter 2: Literature review

2.1 Line pipe steels

2.1.1 Introduction

Line pipe steels are microalloyed steels suitable for manufacturing pipelines to transport oil and gas. These steels have lower carbon content (between 0.03 – 0.1 wt%) resulting in improved toughness and weldability. The loss in strength due to reduction in carbon is recovered by addition of alloying elements such as niobium, vanadium, titanium, molybdenum, and through thermomechanical controlled processing (TMCP) which increases the strength by (a) grain size refinement, (b) precipitation strengthening, and (c) solute solution strengthening [11–13]. Increasing the operating pressure of the pipelines can result in an increase in the amount of oil and gas transported in a given time. This is made possible by continuous improvement in the strength of line pipe steels. Higher strength allows fabrication of thinner pipeline walls with larger diameters, effectively reducing the cost of construction, while increasing transportation volume[11].

2.1.2 Classification of line pipe steels

Line pipe steels are classified based on their yield strength according to the American Petroleum Institute (API) standard. For example, line pipe steel referred to as API X80 indicates a minimum required yield strength of 80 ksi (kilo-pounds per square inch). The first microalloyed X52 steel introduced in 1953 was vanadium strengthened. There has been a continuous improvement in the strength from 52 ksi in 1950 to 120 ksi presently [14]. X70 and X80 grade line pipe steels are still predominantly used in pipeline construction, and X65 grade is used in sour service, whereas X100 grade and above are in development phase [15,16]. The third West-East

Gas Pipeline in China, completed recently, used X90 steel for some sections. Advancements in microalloying, improvements in thermomechanical controlled processing, reduction of carbon content, as well as developments in the field of welding, have led to the improvement in properties of line pipe steels and their potential commercial application [17].

The microstructure of initial grades, X52 and X65, consisted of polygonal ferrite and pearlite, resulting in limited strength [18]. Improved microalloying strategy combined with thermomechanical controlled processing resulted in improvement in strength and toughness in X70 steel due to grain refined non-polygonal irregular ferritic or bainite microstructure [19]. Further advancement in rolling with accelerated cooling led to X80 steel, consisting of fine-grained irregular ferrite or bainite with randomly distributed martensite/austenite (M/A) islands and other precipitates [19,20]. X100 and higher grade line pipe steels consist of highly dislocated bainitic or acicular ferritic microstructures with M/A islands, which provide the increase in strength [19–22]. Grade X100 and above are susceptible to brittle fracture in addition to potential undetectable strain-aging during service, and these problems have prevented their commercial application [23–26].

2.1.3 Overview of line pipe steel chemistry

The properties of steel for structural application, such as strength and toughness, can be improved by developments in processing, as is the case in TMCP, or by suitable alloying. Alloying in combination with the processing can increase strength by grain refinement, precipitation strengthening or solid solution strengthening [11]. In addition to increasing strength, the steel has to be designed to facilitate fabrication and weldability.

Carbon exists in steel either in solid solution or as precipitates. It occupies the octahedral interstitial sites and provides significant solid solution strengthening. Carbon also forms brittle

carbide precipitates which hamper the toughness [27]. This results in a need to find an optimum carbon content to achieve acceptable compromise between strength and toughness. Modern line pipe steels have a low carbon content in the range of 0.03 to 0.1 wt% in order to improve the weldability and low temperature fracture toughness [28]. Weldability may be improved by maintaining the carbon content close to the lower limit of 0.03wt%. However, it is important to systematically examine the implication of varying the carbon content on the microstructure and properties of the line pipe steel. This provides the motivation to study the effect of carbon content on the microstructure and properties upon welding.

The effect of other alloying elements on the weldability is defined by the carbon equivalent of the steel. For low carbon steel containing less than 0.18 wt% carbon, Ito and Bessyo [29] proposed carbon equivalent in weight % as:

$$CE = C + \frac{V}{10} + \frac{Mo}{15} + \frac{Si}{30} + \frac{Cr + Cu + Mn}{20} + \frac{Ni}{60} + 5B \quad (2.1)$$

This demonstrates that other alloying elements also affect the weldability, but the effect of carbon is the most pronounced amongst commonly used alloying elements and signifies the need to have low carbon content in the line pipe steel. This equation is valid for boron content less than 0.005 wt%.

Austenite decomposes upon cooling to different daughter products such as ferrite, pearlite, bainite and martensite. The alloying elements present in the steel affect this transformation behaviour. For equilibrium transformation, alloying elements such as carbon, manganese, nickel and cobalt decrease the austenite to ferrite transformation temperature. These elements are referred to as austenite stabilizers. On the other hand, ferrite stabilizers are alloying elements such as molybdenum, vanadium, niobium or silicon, which increase the austenite to ferrite transformation temperature. However, during continuous cooling, alloying elements such as niobium,

molybdenum, etc., decrease the transformation rate, thereby reducing the austenite to ferrite transformation temperature significantly. They can segregate to austenite grain boundaries, lowering their energy, thereby delaying nucleation of new phases. In solution, alloying element such as niobium causes solute drag on the interface, thereby reducing the mobility of the interface [30]. These kinetic factors result in lowering of the austenite to ferrite transformation temperature during continuous cooling transformation, promoting formation of bainitic or martensitic structures.

Niobium is an important microalloying element added to line pipe steel to retard recrystallization of austenite and grain growth during hot rolling of slabs. The mechanism involved is reduction of interface mobility due to the solute drag effect and Zener pinning of the boundaries. This results in pancaking of the austenite grains, which provides additional nucleation sites, thereby promoting formation of fine ferritic structure upon cooling [31]. In addition, niobium precipitates as NbC and Nb(CN) in ferrite, providing additional precipitation strengthening [31–33]. Niobium is typically present in the range 0.03 – 0.11 wt% in line pipe steel.

Titanium is another microalloying element added to line pipe steel. It forms TiN precipitates, which are very stable and exist up to the melting point of steel [34,35]. The stability of TiN limits austenite grain growth by pinning austenite grain boundaries during reheating as well as in the heat affected zone very close to the weld pool. It is important to maintain the weight ratio of Ti to N below 3.4 (atomic ratio below 1) to avoid formation of larger TiN precipitate. Large TiN precipitates above 500 nm act as crack initiation sites and also result in loss of Zener pinning due to reduction in TiN distribution density [36].

Vanadium forms almost no precipitates in austenite and is available for precipitate formation during and after the austenite to ferrite transformation. Depending on the rolling

schedule and chemical composition of the steel, V(C,N) precipitates form in ferrite and provide significant precipitation strengthening [11,37,38]. Microalloying elements are also added in combination, leading to Nb-Ti or Nb-Ti-V line pipe steel. These microalloying elements, in addition to elements like molybdenum, form complex precipitates with different morphologies and dimensions and have potential advantages due to the interaction between the alloying elements[11,35,38].

Molybdenum is known to suppress the austenite to ferrite transformation temperature, resulting in formation of irregular ferritic or bainitic microstructure [39,40]. The addition of Mo also promotes finer Nb(C,N) precipitates in ferrite, resulting in greater precipitation strengthening [41]. Manganese is an austenite stabilizer, provides solid solution strengthening and increases hardenability. Manganese forms manganese sulphide, thereby preventing iron sulphide inclusions which can cause hot shortness and hamper the toughness [27].

Chromium is a carbide former which contributes to the strength of the steel. Chromium also introduces solute drag effect, which delays austenite decomposition [42]. It is an important alloying element added to improve the corrosion resistance of steel. However, there is scarcity of a systematic study on the effect of chromium content on continuous cooling austenite decomposition of line pipe steel.

2.1.4 Welding of line pipe steel

The microstructure of line pipe steel is tailored by carefully designed TMCP. Refined microstructure and desirable precipitate state are obtained via TMCP, resulting in superior mechanical properties [43]. These coils or plates of steel produced by TMCP go through a pipe forming process where they are welded spirally or longitudinally, usually by a submerged arc

welding (SAW) process [44,45]. These pipes are then transported to the construction site where they are joined end to end along the girth, commonly using gas metal arc welding (GMAW). The welding processes create a heat affected zone (HAZ) close to the fusion line, which experiences high temperature, resulting in changes in the microstructure and properties in the affected region.

The SAW process has a high heat input, resulting in a larger HAZ and slower cooling rates. For SAW, Kulakov [46] experimentally found that the average cooling rate is approximately 5°C/s in the temperature range 800°C to 500°C, which is the relevant temperature range for austenite decomposition. The advantage of SAW is its high weld deposit rate, making it a more productive welding route. The high heat input associated with SAW results in a large HAZ, with potentially detrimental microstructure development, leading to softening of the region or a reduction in toughness[47–49].

GMAW on the other hand has relatively low heat input, resulting in a smaller HAZ and faster cooling rate. GMAW is generally carried out by a single torch to deposit weld metal, with an inert gas surrounding the arc to stabilize the arc and prevent oxidation. There have been developments in the field of GMAW to increase the productivity. Dual torch GMAW uses a second torch closely following the first to increase the weld deposit rate [47]. Tandem GMAW uses a dual feed wire in a single torch to increase productivity [50]. Gaudet [51] measured the average cooling rate to be approximately 50°C/s for cooling from 800 to 500°C in the case of GMAW.

There have been other advances in welding processes like laser welding, forge welding, induction welding and resistance welding [52]. All these processes have different heat input and scale of operation, resulting in varied extent of the HAZ and cooling rates. This variability in the welding processes can lead to very different microstructures. A model targeted at predicting microstructural evolution of the HAZ should consider the wide spectrum of heat input, which in

turn means a range of cooling rates. The next section discusses more about the heat affected zone developed as a result of welding of line pipe steel.

2.2 The heat affected zone

2.2.1 HAZ formation

Welding is a necessary process that pipelines undergo. This results in molten metal in the fusion zone and high temperature experienced by the metal adjacent to the fusion line. The extremely high temperature experienced by steel results in microstructural changes and the region is called the heat affected zone. Microstructural changes and the extent of the HAZ depends on the steel chemistry and the welding heat input. The peak temperature and cooling rate at a specific location in the HAZ determine the extent of precipitate dissolution and grain growth, which in turn determine the microstructure upon cooling [35,53,54]. This results in a graded microstructure in the HAZ on moving away from the fusion line. During a single pass weld, the HAZ has four distinct regions shown schematically in Figure 2.1. As one moves away from the fusion line, these regions are the coarse grain heat affected zone (CGHAZ), the fine grain heat affected zone (FGHAZ), the intercritical heat affected zone (ICHAZ) and the subcritical heat affected zone (SCHAZ)[50].

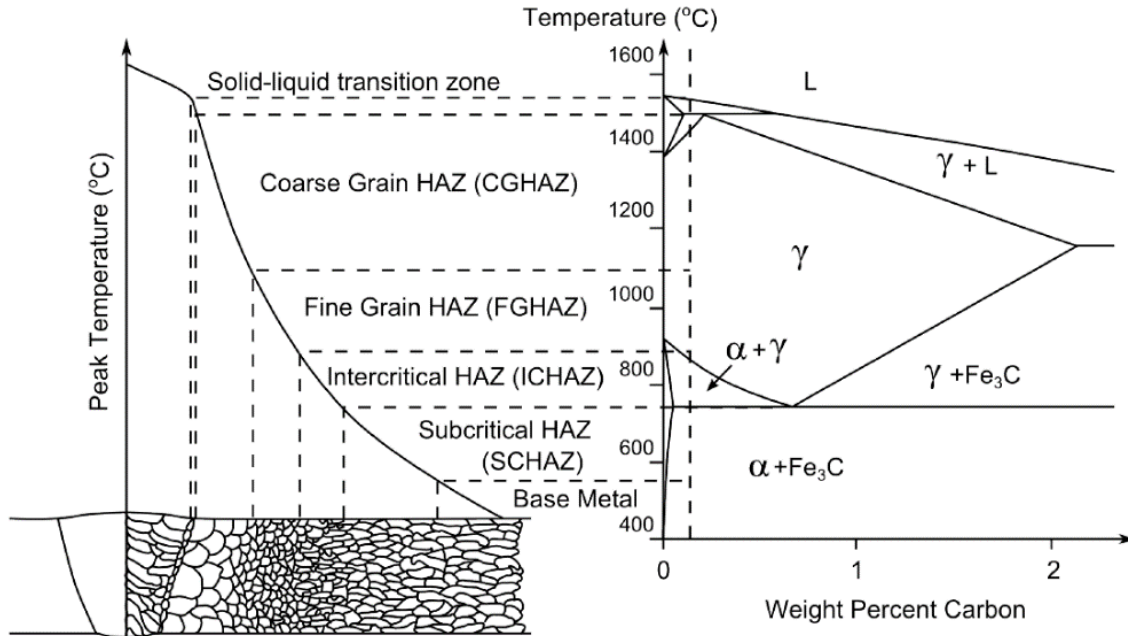


Figure 2.1: Schematic showing the different regions in the HAZ and the associated peak temperature during single torch weld pass, adapted from [50]

The region closest to the fusion line experiences very high temperature, leading to complete austenite formation, coarsening and dissolution of niobium precipitates, i.e. NbC and Nb(C,N), resulting in significant austenite grain growth, hence the name CGHAZ. TiN particles remain stable up to the melting temperature, controlling the limiting grain size in the CGHAZ by Zener pinning [34]. Coarse austenite grains promote formation of low temperature transformation products such as bainite along with martensite/austenite (M/A) constituents, which can be detrimental to the toughness of the weld region [8–10,54]. The next region in the HAZ is the FGHAZ which undergoes complete austenitization but experiences lower peak temperature. This leads to limited austenite grain growth and precipitate dissolution. The ICHAZ undergoes partial austenitization due to lower peak temperature, resulting in carbon-rich austenite, which promotes the formation of martensite/austenite constituents on cooling and can be detrimental to the toughness. The SCHAZ is furthest from the fusion line where the peak temperature lies in the

ferrite field, resulting in no phase transformation. The microstructure in this region is tempered and coarsening of carbides may occur.

Multi-pass welding leads to a more complex microstructure distribution due to interaction between the HAZ of the different passes. Figure 2.2 shows a schematic of the microstructure in the HAZ of a dual pass weld [55]. In addition to the four zones discussed above, other regions of interest, like the intercritically reheated CGHAZ (ICCGHAZ) develop due to the combined effect of the passes. When the CGHAZ of the first pass experiences the intercritical temperature in the second pass, M/A constituents can form along the prior austenite grain boundaries upon cooling. The ICCGHAZ is a potential region of fracture and failure in the weld [10,56].

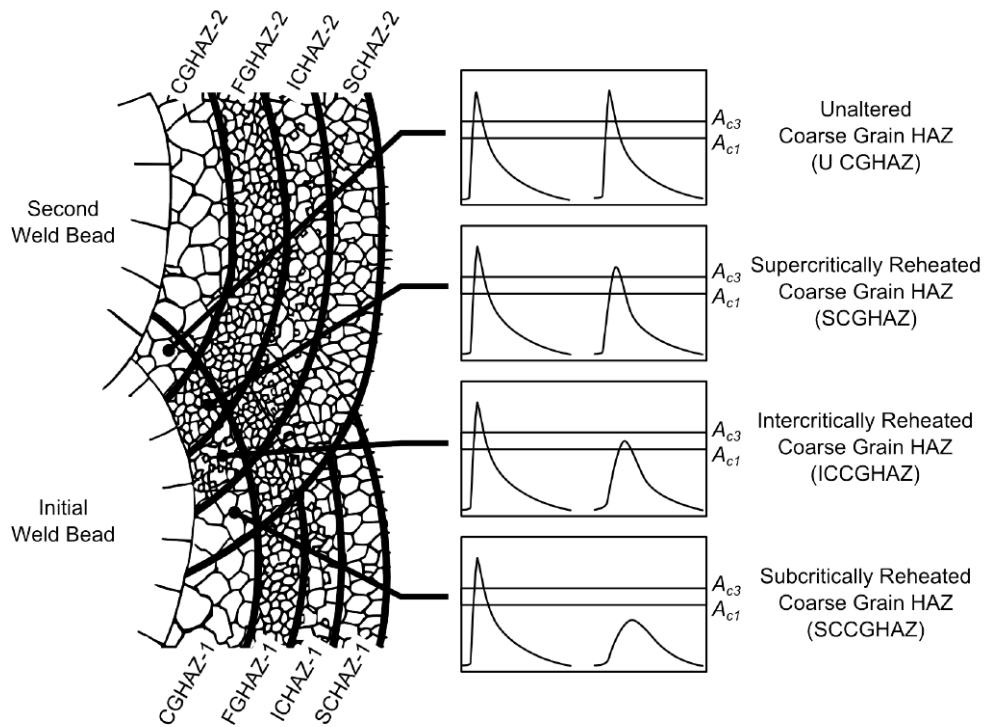


Figure 2.2: Schematic showing the microstructure and thermal cycle during multipass welds, adapted from [55]

2.2.2 Relevance of the coarse grain heat affected zone

The CGHAZ lies adjacent to the fusion line and experiences extreme temperature close to the melting point of steel. This causes dissolution of most precipitates and significant grain growth of the austenite grains [57,58]. The austenite decomposition product depends on the chemistry, including the amount of alloying elements like niobium, molybdenum, carbon and titanium, and their state (precipitate or in solution), the heat input of weld which determines the cooling rate, and the prior austenite grain size. Depending on the aforementioned parameters, the decomposition products in the CGHAZ for X70 and X80 line pipe steels are generally found to be irregular ferrite or bainite [6,10,40,58–62]. In addition, M/A particles form with different amounts and morphologies as explained later in section 2.3.5. Polygonal ferrite, pearlite and martensite are not commonly observed in X70/X80 CGHAZ for heat input relevant to pipeline welding.

Several researchers have shown that the microstructure in CGHAZ can lead to failure due to low toughness and high ductile to brittle transition temperature [6–8,10,63]. Multiple studies suggest that the M/A constituent deteriorate toughness by acting as cleavage crack nucleation sites and facilitating debonding [64–66]. Some other researchers have presented results suggesting that M/A does not always hamper toughness and the morphology of M/A determines its effect on toughness [6,67]. Yang et al. [67] reported islands of M/A in CGHAZ arrest cracks and improve toughness, whereas coarse stringers or massive M/A constituents can crack and debond from the matrix, leading to reduction in toughness. Furthermore, it has been reported that faster cooling rates result in an increase in the density of high angle grain boundaries, which act as obstacles to crack propagation, thereby improving the toughness [7,10].

Zhu et al. [61] examined the influence of heat input on the microstructure of the CGHAZ in X80 steel. The microstructure consisted of completely bainitic ferrite and a small amount of

M/A constituent at a heat input of 0.8 kJ/mm ($t_{8/5} = 4.4\text{s}$). On increasing the heat input to 1.7 kJ/mm ($t_{8/5} = 18.4\text{s}$), the microstructure consisted of granular bainite and M/A. At even higher heat input of 2.5 kJ/mm ($t_{8/5} = 38.6\text{s}$) and 3.5 kJ/mm ($t_{8/5} = 76.6\text{s}$), the microstructure was predominantly granular bainite with M/A constituents and a small amount of polygonal ferrite. The hardness decreased from about 255 Hv to 210 Hv as heat input increased from 0.8 to 2.5 kJ/mm, and remained around 210 Hv for higher heat inputs. Similarly, Miao et al. [68] reported that an increase in heat input from 1.6 to 5.8 kJ/mm resulted in a transition from lower bainite with greater high angle grain boundary (HAGB) density to granular bainite with reduced HAGBs in the CGHAZ of X80 steel with 0.1 wt% Nb. The morphology and distribution of M/A constituent was described qualitatively. The M/A was fine and more uniformly distributed at heat input less than 3kJ/mm, whereas islands of coarse M/A constituents were observed at higher heat input. The impact toughness at -20°C decreased from about 270 to 30 J on increasing the heat input from 1.6 to 5.8 kJ/mm.

In a recent study, Singh et al. [69] looked into continuous cooling in the CGHAZ of an X80 grade steel with a cooling rate ranging from 3 to 100°C/s . The dominant transformation products for all cooling rates were bainite with some M/A constituent. At cooling rates below 5°C/s , some ferrite and pearlite were observed in addition to bainite and M/A. The transformation start temperature was lowered from 660 to 545°C as the cooling rate increased from 3 to 100°C/s . Tafteh [58] reported that the transformation start temperature is suppressed from 600 to 550°C on increasing the cooling rate from 3 to 100°C/s for an X80 steel with 0.06wt% carbon. The microstructure changed from granular bainitic microstructure at 3°C/s to granular bainite with increasing amounts of lower bainite, as cooling rate increased from 10 to 60°C/s , to completely lower bainite at 100°C/s . Less than 2% M/A was reported at all cooling rates.

Mandal [10] reported bainitic microstructure with M/A constituents in the CGHAZ of X80 line pipe steels. The study found that increasing the carbon content from 0.03 to 0.06wt% changed the microstructure of simulated CGHAZ significantly, causing an increase in high angle grain boundary density and improving the toughness. Ma et al. [70] studied the role of carbon for low heat input girth welds on X80 grade steel and found the increase in carbon promotes transformation at a lower temperature and a microstructure consisting of bainitic laths with a high density of high angle misorientation boundaries in the CGHAZ. The information on the effect of chromium on microstructure and properties in the CGHAZ is scarce. A recent study found the increase in chromium from 0.33 to 1.02wt%, at heat input between 20 kJ/cm (~28°C/s cooling rate) and 200 kJ/cm (~2.8°C/s cooling rate), resulted in a decrease in acicular ferrite and an increase in M/A content, resulting in a drop in impact toughness [71].

It is evident that the CGHAZ has a complex behavior due to varied microstructure possibilities, depending on chemistry and thermal cycle. This makes the CGHAZ an important field for further research. A systematic study into the effect of carbon and chromium content, two important alloying elements, over a wider range of cooling rates, on the CGHAZ microstructure using advanced microscopy can potentially provide useful insights and better understanding of the CGHAZ.

2.3 Continuous cooling transformation of austenite

2.3.1 Polygonal ferrite and pearlite

Austenite can transform into a variety of microstructures upon cooling, depending on the cooling rate, alloying elements and their state as precipitate or in solution, prior austenite grain size and the state of stress in the austenite grains. Polygonal ferrite, pearlite, irregular ferrite,

bainite or martensite are the possible microstructures which can form individually or as mixed microstructures. It is worth mentioning that the microstructure of the CGHAZ in X70 and X80 line pipe steels consists predominantly of bainite or irregular ferrite with some M/A constituent, as discussed in Section 2.2.2.

Polygonal ferrite forms at high temperature when austenite is cooled at sufficiently slow cooling rate. Ferrite nucleates at prior austenite grain boundaries and grain corners, and grows as equiaxed ferrite grains, alternatively named polygonal ferrite [72,73]. The solubility of carbon in ferrite is significantly lower than in austenite. Long-range diffusion of carbon atoms from the newly formed ferrite into the austenite and the transfer of substitutional atom across the austenite-ferrite interface controls the growth of polygonal ferrite. In low carbon steels, partitioning of substitutional atoms at the austenite-ferrite interface may slow down the growth process significantly [72]. As more austenite transforms into ferrite, the carbon concentration in the remaining austenite increases due to the rejection of carbon from ferrite. Eventually the austenite reaches the eutectoid composition and pearlite formation can take place. Pearlite contains alternate lamella of ferrite and cementite, and its growth is controlled by carbon diffusion. As the temperature decreases, the driving force for austenite decomposition increases but the diffusivity of carbon decreases, resulting in finer pearlite lamella [74]. In addition, the interfacial energy between the ferrite and the cementite also influences the interlamellar spacing. An increase in the interfacial energy results in a coarser pearlite in order to minimize the interfacial surface area.

2.3.2 Irregular ferrite

With increasing cooling rate, the transformation temperature is pushed to a lower temperature, and an irregular ferrite microstructure is obtained. The microstructure has an intergranular substructure due to higher dislocation density compared to polygonal

ferrite[39,72,75]. In addition, M/A constituents are found and their origin is suggested to be carbon-rich triple junctions where the ferrite interfaces converge [75]. The irregular appearance is a consequence of several factors, including the anisotropy in elastic energy and interfacial energy, as well as the morphological instability of the austenite-ferrite interface due to partitioning of solute atoms at the boundaries and substructure. The increase in dislocation density results in an increased hardness in irregular ferrite compared to the polygonal structure [39]. It is worth mentioning that there are inconsistencies with the nomenclature of ferrite phases in the literature, with names like acicular ferrite and granular ferrite used to describe microstructure similar to an irregular ferrite microstructure[39,72,73].

2.3.3 Bainite

Upon increasing the undercooling further, the driving force for austenite decomposition increases, whereas the diffusivity decreases. On achieving sufficient undercooling, a lath or plate type microstructure called bainite is obtained. There are two schools of thought about bainitic transformation. One assumes diffusion driven transformation and the other favors displacive transformation. According to the diffusion-controlled transformation theory, the growth of bainite occurs with carbon diffusion and formation of carbide simultaneously during austenite decomposition [72,76]. The second theory suggests that bainite is formed by a displacive mechanism, followed by the partitioning of carbon, and carbide formation is a secondary step after bainite has already formed. The carbon diffuses into inter-lath regions or precipitates within the lath [77,78].

Irrespective of the mechanism of bainite formation, researchers have generally agreed on classification of bainite into upper and lower bainite. Upper bainite is formed at higher temperatures compared to lower bainite. The carbides in upper bainite form from enriched

austenite, such that the upper bainitic ferrite itself is essentially carbide free. This results in carbides being present between bainite laths. Since the lower bainite is formed at lower temperatures, the diffusivity is lower, resulting in carbide precipitation within the ferrite laths, in addition to some inter-lath carbide precipitation from enriched austenite [78]. It is also observed that the upper bainite has a higher proportion of low angle grain boundaries, whereas lower bainite has more high angle grain boundaries, resulting in higher strength and fracture toughness of lower bainitic microstructures, due to crack deflection by high angle boundaries [40,80]. The microstructure of both upper and lower bainite can appear similar under the optical microscope, and it may be difficult to differentiate between the two. The scanning electron microscope (SEM) and electron backscattered diffraction (EBSD) are now commonly used to characterize bainitic microstructures. Mandal [10] in a recent work used EBSD to compute a ‘characteristic length scale’, defined as the inverse of the high angle grain boundary density, to describe different bainitic microstructures.

2.3.3.1 Orientation relationship (OR) between product and parent austenite

Bainitic transformation products are found to have specific orientation relationships with the parent austenite. This relationship is described by the misorientation between the parent and daughter lattices expressed in terms of planes and directions of the two phases [7,80,81]. Several orientation relationships have been observed in austenite to ferrite transformation including Bain, Pitch, Greninger-Troiano, Nishiyama-Wassermann (NW) and Kurdjumov-Sachs (KS) [67]. KS and NW are the commonly observed orientation relationships. The KS orientation relationship requires the $\langle 110 \rangle$ directions of $\{111\}$ planes of the parent austenite phase to be parallel to the $\langle 111 \rangle$ directions of the $\{110\}$ planes of the daughter ferrite. The NW orientation relationship

exists when the $\langle 112 \rangle$ directions of the $\{111\}$ planes of parent austenite phase are parallel to the $\langle 111 \rangle$ directions of the $\{110\}$ planes of the daughter ferrite.

Based on cubic symmetry, there are 24 possible KS orientation relationships, as shown in Table 2.1 [7,80,82]. The 24 variants are divided into four closed packed (CP) groups, with each group having six variants sharing the same parallel relationship of closed packed planes with austenite. The KS orientation can also be grouped into three Bain groups based on distinctive Bain correspondence ($[001]_{\gamma} // [001]_{\alpha}$, $[100]_{\gamma} // [110]_{\alpha}$, $[010]_{\gamma} // [\bar{1}10]_{\alpha}$), with each Bain group having eight possible KS orientation relationships[65]. Variants within the same Bain group are separated by low misorientation angles, whereas regions belonging to different Bain groups are separated by high misorientation angles.

Table 2.1: Twenty-four variants of the K-S orientation relationship and the corresponding CP group, Bain group and misorientation (reprinted with permission from [80])

Variant no.	Plane parallel	Direction parallel	CP group	Bain group	Misorientation from VI (°)
V1	$(111)_{\gamma} // (011)_{\alpha}$	$[\bar{1}01]_{\gamma} // [\bar{1}\bar{1}\bar{1}]_{\alpha}$	CP1	B1	–
V2		$[101]_{\gamma} // [\bar{1}\bar{1}\bar{1}]_{\alpha}$		B2	60.0
V3		$[01\bar{1}]_{\gamma} // [\bar{1}\bar{1}\bar{1}]_{\alpha}$		B3	60.0
V4		$[011]_{\gamma} // [\bar{1}\bar{1}\bar{1}]_{\alpha}$		B1	10.5
V5		$[1\bar{1}0]_{\gamma} // [\bar{1}\bar{1}\bar{1}]_{\alpha}$		B2	60.0
V6		$[\bar{1}\bar{1}0]_{\gamma} // [\bar{1}\bar{1}\bar{1}]_{\alpha}$		B3	49.5
V7	$(\bar{1}\bar{1}1)_{\gamma} // (011)_{\alpha}$	$[10\bar{1}]_{\gamma} // [\bar{1}\bar{1}\bar{1}]_{\alpha}$	CP2	B2	49.5
V8		$[101]_{\gamma} // [\bar{1}\bar{1}\bar{1}]_{\alpha}$		B1	10.5
V9		$[\bar{1}\bar{1}0]_{\gamma} // [\bar{1}\bar{1}\bar{1}]_{\alpha}$		B3	50.5
V10		$[\bar{1}\bar{1}0]_{\gamma} // [\bar{1}\bar{1}\bar{1}]_{\alpha}$		B2	50.5
V11		$[011]_{\gamma} // [\bar{1}\bar{1}\bar{1}]_{\alpha}$		B1	14.9
V12		$[01\bar{1}]_{\gamma} // [\bar{1}\bar{1}\bar{1}]_{\alpha}$		B3	57.2
V13	$(\bar{1}11)_{\gamma} // (011)_{\alpha}$	$[0\bar{1}1]_{\gamma} // [\bar{1}\bar{1}\bar{1}]_{\alpha}$	CP3	B1	14.9
V14		$[0\bar{1}\bar{1}]_{\gamma} // [\bar{1}\bar{1}\bar{1}]_{\alpha}$		B3	50.5
V15		$[\bar{1}01]_{\gamma} // [\bar{1}\bar{1}\bar{1}]_{\alpha}$		B2	57.2
V16		$[\bar{1}0\bar{1}]_{\gamma} // [\bar{1}\bar{1}\bar{1}]_{\alpha}$		B1	20.6
V17		$[110]_{\gamma} // [\bar{1}\bar{1}\bar{1}]_{\alpha}$		B3	51.7
V18		$[110]_{\gamma} // [\bar{1}\bar{1}\bar{1}]_{\alpha}$		B2	47.1
V19	$(111)_{\gamma} // (011)_{\alpha}$	$[\bar{1}10]_{\gamma} // [\bar{1}\bar{1}\bar{1}]_{\alpha}$	CP4	B3	50.5
V20		$[110]_{\gamma} // [\bar{1}\bar{1}\bar{1}]_{\alpha}$		B2	57.2
V21		$[0\bar{1}\bar{1}]_{\gamma} // [\bar{1}\bar{1}\bar{1}]_{\alpha}$		B1	20.6
V22		$[\bar{1}\bar{1}0]_{\gamma} // [\bar{1}\bar{1}\bar{1}]_{\alpha}$		B3	47.1
V23		$[101]_{\gamma} // [\bar{1}\bar{1}\bar{1}]_{\alpha}$		B2	57.2
V24		$[101]_{\gamma} // [\bar{1}\bar{1}\bar{1}]_{\alpha}$		B1	21.1

During austenite decomposition to bainite, variant pairs belonging to the same Bain group are separated by low angle grain boundaries, whereas variant pairs belonging to different Bain groups are separated by high angle grain boundaries. The strain induced during bainite formation can be accommodated either by the plastic deformation of austenite or by the formation of variant pairing which favors self-accommodation of the strain [80,115]. At high temperature transformation, the softer austenite can accommodate transformation strain by deforming. Therefore, at high temperature, low misorientation angle variant pair like V1/V4 or V1/V8 which belong to the same Bain group are preferred, as shown in Figure 2.3a. This results in coarse regions of a Bain group [80]. As the transformation temperature decreases, accommodation of plastic strain becomes increasingly difficult due to an increase in the flow stress of austenite. Under such condition, variant pairs like V1/V2, which favor self-accommodation of strain are formed, resulting in type II microstructure as shown in Figure 2.3b [80].

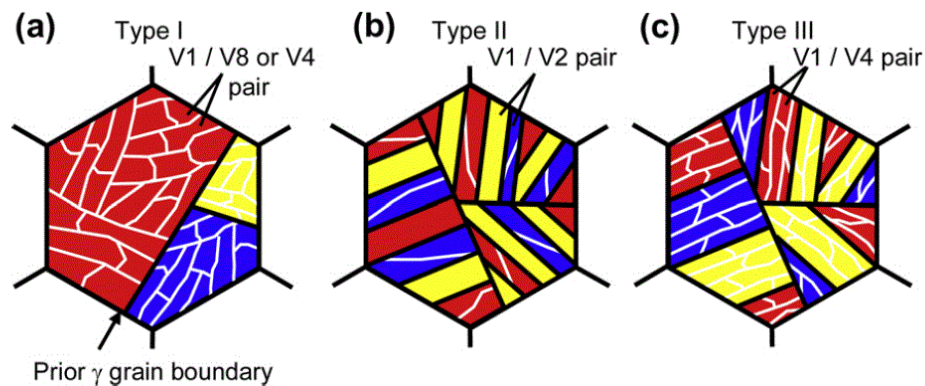


Figure 2.3: Schematics showing the variant pairing within a prior austenite grain indicating frequently occurring variant pair (a) Bainite formed at high temperature (b) bainite formed at intermediate temperature (c) lath martensite formed at low temperature, each color represent a single Bain group, white and black line represent low and high angle grain boundaries respectively (reprinted with permission from [80])

On lowering the transformation temperature below the martensite start temperature, type III martensitic microstructure is obtained. Similar to type II, same CP group variants form adjacent to each other. However, within a single CP group, sub-blocks of different variants belonging to the same Bain group form [80].

2.3.4 Martensite

At temperatures below the martensite start temperature, sufficient driving force is available for displacive transformation of austenite into martensite. Martensite has a body centered tetragonal (BCT) structure. This change in structure from face centered cubic (FCC) to BCT introduces shear as well as an increase in the volume. The morphology of martensite depends on the chemistry, especially the carbon content. Generally, in low carbon steels, the transformation product appears as lath. Each lath is a result of homogeneous shear, and a bunch of parallel laths form a packet containing high dislocation density. Several packets exist within a single prior austenite grain as seen in Figure 2.3(c). Most of the laths are submicron in width, and the fine structures have very high dislocation density [83]. Plate martensite is observed in the case of carbon rich steel, commonly greater than 1 wt% carbon and is characterized by non-parallel plates. The plates which are first formed normally traverse through the prior austenite grain, thereby limiting the length of subsequent plates, leading to a range of plate size. A consequence of impingement of non-parallel plates is the development of microcracks within the large plates. The substructure of plate martensite constitutes micron-sized deformation twins or dislocation arrays [83,84].

2.3.5 Martensite/Austenite constituent (M/A)

During austenite decomposition to ferrite or bainite, carbon is rejected into austenite, causing carbon enrichment and stabilization of the austenite. This can result in some austenite

retained at room temperature and some of it partially transformed to martensite on cooling below the martensite start temperature, forming M/A constituent. The literature suggests that the morphology and amount of M/A depend on multiple factors, including but not limited to the cooling rate, chemistry and transformation temperature. Wang and Yang [85] demonstrated that an increase in the austenite stabilizer content resulted in a greater M/A fraction. In an X80 steel, Reichert [40] found that low temperature bainitic transformation below 550 °C resulted in less than 3% M/A constituent, whereas transformation around ~580 – 600 °C resulted in 12% M/A. The morphology consisted of elongated particles with an aspect ratio of ~3 at the grain boundary, while the grain interior had relatively spherical M/A particles. For the same steel, Mandal[10] reported M/A fraction less than 3.5% for transformation temperature below 560°C, whereas a maximum of 6.5% was reported for transformation starting at 585°C. Li et al. [6] found that an increase in cooling rate results in the change of M/A morphology from massive blocky shape to elongated rods in the CGHAZ.

2.4 Microstructure modelling

The experimental results for austenite decomposition have been previously described using phenomenological models. A way to describe isothermal kinetics of phase transformation was proposed by Johnson and Mehl [86], Avrami [87] and Kolmogorov [88], and is known as the JMAK or Avrami relation:

$$f = 1 - \exp(-\beta t^n) \quad (2.2)$$

where f is the fraction transformed at any given time t , β is a temperature dependent rate parameter and n is the JMAK exponent which depends on the growth geometry and nucleation condition. In practice, the values of n and β are empirically determined. The principle of additivity can be

applied to describe the decomposition kinetics during continuous cooling, if it is an isokinetic reaction [89]. A process is isokinetic when the rate of transformation can be expressed as a product of two separate functions; one dependent on the fraction transformed and the other on the temperature only [89,90]. The differential form of JMAK, as expressed in the following equation, satisfies the criteria for additivity if n is a constant and β is a function of temperature:

$$\frac{df}{dt} = (\beta)^{\frac{1}{n}} \left\{ n (1 - f) \left(\frac{1}{\ln(1 - f)} \right)^{\frac{n-1}{n}} \right\} \quad (2.3)$$

Militzer et al. [91,92] presented a microstructure model to describe austenite decomposition to ferrite for HSLA steel accounting for different cooling rates, prior austenite grain size and retained strain. The transformation start was modelled using carbon diffusion-controlled growth of ferrite nucleated at austenite grain corners. Ferrite nucleation was presumed to stop once a critical carbon concentration was reached in the entire grain boundary area, and this condition was considered to represent the measurable transformation start temperature (e.g. 5% transformed). The growth of ferrite was modelled using the JMAK model with additivity. In a later work [93] the transformation start temperature model was expanded to include the solute drag effect due to niobium.

The austenite decomposition can result in different transformation products such as ferrite, pearlite, bainite and martensite; therefore, they can be modelled to occur either simultaneously [94] or sequentially [95–97]. Generally, there is little overlap between different product formation, making the sequential approach more attractive due to its ease of formulation using individual JMAK models for each product separated by suitable transition conditions. Militzer et al. [98] extended their previous work [93] to include austenite decomposition into bainite. The work was divided into five sub-models including ferrite start temperature, ferrite growth, bainite start

temperature, bainite growth and M/A fraction. The ferrite start temperature and ferrite growth were based on previous work [93] as discussed above. The bainite start model proposed in this work used empirically determined parameters and thermodynamically calculated bainite nucleation temperatures based on a critical driving pressure as proposed by Bhadeshia [78]. The proposed bainite growth model used JMAK with additivity. A model to describe the continuous cooling decomposition of vanadium microalloyed steel using JMAK with additivity was also presented by Azghandi[97]. The model had sequential sub-models on ferrite start temperature, ferrite growth, pearlite start temperature, pearlite growth, bainite start temperature, bainite growth and martensite start temperature.

Jia et al. [99] presented a new modelling method for continuous cooling transformation when the JMAK rate parameter is not only a function of temperature but also a function of the fraction transformed. This work presented a numerical approach to find the JMAK exponent and express the rate parameter as a product of one function solely dependent on temperature and another function dependent on the fraction transformed. Using this method, the ferrite transformation in a TRIP steel and the bainite transformation in a CP steel during continuous cooling was successfully described.

The JMAK based growth models are empirical models where the rate parameter and the JMAK exponent are fit parameters without physical meaning. There has been work towards the development of physical models to describe austenite decomposition. Vandermeer [100] developed a grain boundary nucleated, long range diffusion-controlled growth model to describe the austenite decomposition into pro-eutectoid polygonal ferrite in Fe-C. This model successfully captured the effect of temperature, overall carbon concentration, prior austenite grain size and carbon buildup within austenite grains. Models based on long range carbon diffusion are effective

when the interface mobility is sufficiently high. However, when the mobility of the austenite-ferrite interface is low, the diffusion-based model predicts transformation rates that are too high. The mixed-mode model was thus proposed to account for interface mobility as well as carbon diffusion.

Krielaart et al. [101] presented a mixed-mode model that takes into account the non-equilibrium condition at the moving austenite-ferrite interface during austenite decomposition in a binary Fe-C alloy. The migration of the austenite-ferrite interface is driven by the chemical potential difference between the austenitic and ferritic lattice across the interface. This model looks into the effect of grain size, carbon concentration and temperature on the interface migration behavior. The interface mobility is described by an Arrhenius-type temperature dependent equation:

$$M = M_o \exp\left(-\frac{E}{RT}\right) \quad (2.4)$$

with two fit parameters M_o and E , where, M_o is a pre-exponent factor and E is activation energy. The model was able to reasonably reproduce the thickening and lengthening of ferrite particles, both in diffusion-controlled and interface-controlled transformation regimes. Kop et al. [102] developed a mixed-mode model for austenite to ferrite transformation, taking into account interface mobility, austenite grain size, composition effects and nucleus density. This model was able to adequately reproduce the transformation rates for three low C - Mn steels over a wide range of cooling rates between 0.05 to 60°C/s. Fazeli and Militzer [103] presented a physically based mixed-mode model for low carbon steel, applicable to industrial heat-treatment conditions. This model accounted for carbon diffusion, partitioning of alloying elements and solute drag due to solute elements. The model satisfactorily replicated ferrite growth for a C-Mn steel and two multiphase steels.

Another mixed-mode model was developed by Sietsma and Van der Zwaag [104], where the author introduced a single parameter Z to describe the transformation kinetics. Z is expressed as:

$$Z = \frac{D}{M\chi} \frac{A^\alpha}{V^\alpha} \quad (2.5)$$

where, D is diffusivity of partitioning element, M is the interface mobility, χ is a thermodynamic parameter describing the driving pressure per unit of concentration difference, A^α is the area of the newly growing ferrite grain and V^α is the volume of the growing ferrite grain. Z tends to zero for diffusion-controlled and to infinity for interface-controlled transformation. Decomposition of Fe-C steel with very low carbon content is not necessarily diffusion-controlled. For very low carbon steel transformation starts as interface-controlled transformation, however, as the transformation progress, it moves towards diffusion-controlled transformation. This effect is captured by the model, as the value of Z changes from a very large value at start of transformation due to large A^α / V^α , to a smaller value as the ferrite phase starts to grow. Toloui [105] developed a phase field model coupled with carbon diffusion and interface mobility to describe austenite decomposition in X80 line pipe steel. This model accounted for thermal and microstructural gradients, and the results were validated with observations made from a weld trial.

Chapter 3: Scope and Objectives

Pipelines are joined together by welding, which results in a heat affected zone adjacent to the weld pool, thereby causing microstructural changes. The coarse grain heat affected zone, which is closest to the fusion line, has been identified as a potential region of failure in the literature.

The objective of this work is to use laboratory simulations to develop a model that accounts for the role of carbon and chromium on CGHAZ microstructure and hardness of X80 line pipe steel. The overall goal of this project is sub-divided into the following sub-objectives:

1. To quantify the effect of cooling rate, carbon content and chromium content on the continuous cooling austenite decomposition kinetics in the CGHAZ.
2. To quantify the microstructure obtained after austenite decomposition using optical microscopy and the advanced electron backscattered diffraction technique.
3. To measure the hardness of the decomposition products and quantitatively link it to the microstructural features to establish a structure-property relationship.
4. To expand an existing phenomenological austenite decomposition model to include the effect of carbon and chromium content on (a) bainite start temperature and (b) bainite growth kinetics for different cooling rates.

Chapter 4: Materials and experimental methodology

4.1 Materials

The steels used in this study are laboratory steels which were cast and hot rolled at CanmetMATERIALS in Hamilton, ON. The chemistries are shown in Table 4.1 and were tailored to study the effect of carbon and chromium on austenite decomposition for CGHAZ conditions, typical for X80 grade line pipe steel. The A_{e3} temperatures for the steels were calculated using Thermo-Calc (TCFE7 database) and are reported in Table 4.1. It can be seen that the A_{e3} is very close for all three steels. Note that the addition of chromium results in slight dip in A_{e3} temperature. Chromium is typically considered as a ferrite stabilizer, but at low chromium content reduces the A_{e3} temperature[106–109]. The steels are named as shown in Table 4.1. The nomenclature of one of the steels, L04C08NbMo is explained here; ‘L’ indicates laboratory cast steel, 04C and 08Nb indicate approximately 0.04 wt% carbon and 0.08wt% niobium respectively, whereas Mo indicates presence of molybdenum.

Table 4.1: Chemical composition in wt. % and A_{e3} temperature of the investigated steels

Steel	C	Cr	Nb	Mo	Mn	Ti	N	Si	Al	A_{e3}
L04C08NbMo	0.035	0.023	0.080	0.250	1.72	0.015	0.0055	0.25	0.024	854 °C
L04C08NbMoCr	0.035	0.240	0.083	0.250	1.76	0.014	0.0058	0.26	0.016	849 °C
L06C06NbMo	0.061	-	0.063	0.250	1.63	0.018	0.0055	0.26	0.044	851 °C

All three steels have similar levels of Mo, Mn and Si, and similar Ti/N ratio. Steel L04C08NbMo and L04C08NbMoCr have different amounts of chromium with other alloying elements essentially the same, so they were compared to evaluate the effect of chromium on austenite decomposition. L04C08NbMo and L06C06NbMo vary in carbon content and were compared to study the effect of carbon. It is worth noting that the niobium level varies in these two

steels, but Isasti [110] reported that an increase in niobium from 0.03wt% to 0.06wt% resulted in little variation on austenite decomposition kinetics. This suggests any further increase in niobium may have little effect on austenite decomposition kinetics, if any. Therefore, it is assumed in the present work that any change in austenite decomposition behaviour between L04C08NbMo and L06C06NbMo may be attributed to a change in carbon content.

4.2 Continuous cooling transformation tests

4.2.1 Thermal simulations

Continuous cooling transformation (CCT) tests were carried out to study the effect of cooling rate and carbon and chromium content on the austenite decomposition kinetics. The focus of this study is the austenite decomposition behaviour in the CGHAZ. Thus, heat treatments were conducted to bring Nb into solution and to produce a prior austenite grain size (PAGS) of 80 μ m, typically observed in the CGHAZ [58]. CCT tests were carried out in a GleebleTM 3500 thermomechanical simulator to simulate the CGHAZ microstructure. It can be programmed to undergo thermal cycles with rapid heating rates, isothermal holding at high temperatures and rapid cooling using either gas or water quenching. Tests were carried out under high vacuum ($\sim 2 \times 10^{-5}$ torr). Copper jaws remove heat from the sample by conduction, which is sufficient to maintain 3°C/s cooling rate under vacuum, without the need of helium quench, whereas faster cooling rates need helium quench to maintain the cooling rates. Figure 4.1 shows the setup used for the CCT tests in the Gleeble.

Tubular samples with 8 mm outer diameter, 1 mm wall thickness and 20 mm length, as shown in Figure 4.2, were used to facilitate uniform high cooling rates. Helium was purged through the tube to extract heat and provide fast and uniform cooling.

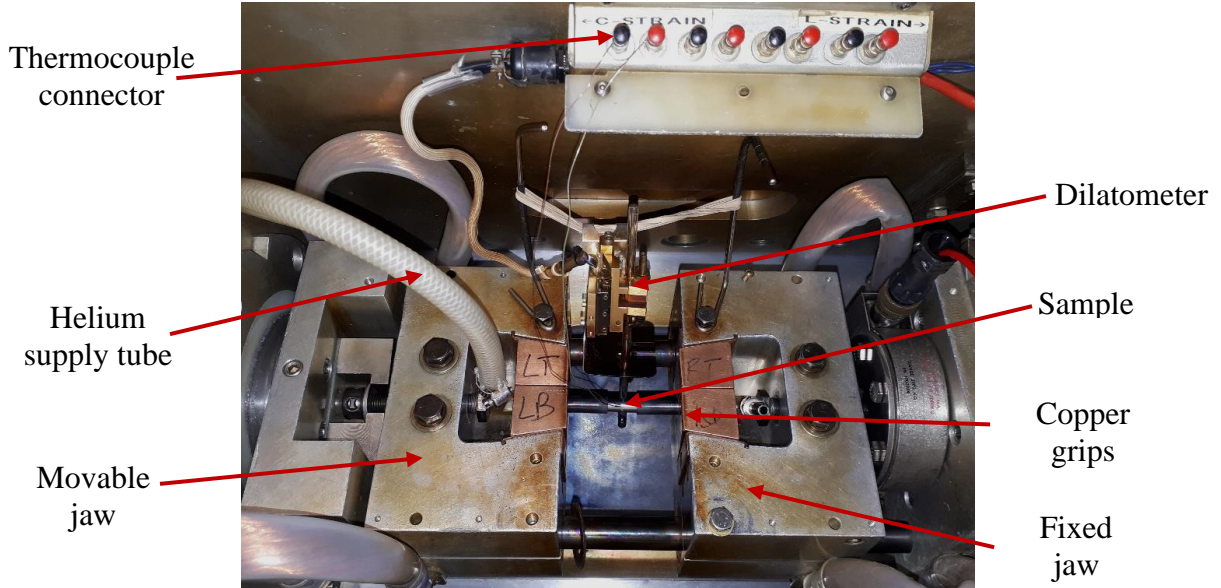


Figure 4.1: Gleeble setup used for austenite decomposition tests on tubular samples

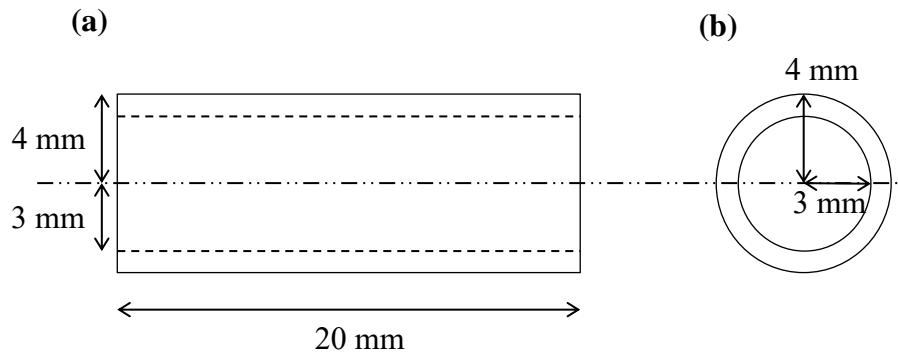


Figure 4.2: Tubular sample geometry used for Gleeble simulation (a) front view (b) side view

Temperature was measured using a K-type thermocouple spot welded at the centre of the sample. The recorded temperature provides feedback to the Gleeble to alter the current in order to maintain the programmed thermal cycle. The Gleeble uses resistance heating to heat the sample; therefore, the heat input can be modified by changing the current supplied through the sample.

4.2.2 Thermal cycles

Thermal cycles were designed to study the effect of carbon, chromium and cooling rate on austenite decomposition in the CGHAZ. Previous work has shown that the cooling rate varies significantly depending on the welding procedure. Kulakov [46] and Gaudet [51] reported that the cooling rates from 800 to 500°C during submerged arc welding (SAW) and gas metal arc welding (GMAW) is approximately 5°C/s and 50°C/s, respectively. In order to model the complete spectrum of welding scenarios, cooling rates of 3, 5, 10, 30, 50 and 100°C/s were the selected.

Figure 4.3 shows the thermal cycle designed for this study. The samples were heated at 50°C/s to 1300°C, where they were isothermally held for 20s, 12s and 12s for L04C08NbMo, L04C08NbMoCr and L06C06NbMo, respectively. Grain growth studies based on LUMet by Romualdi [57] on the three steels showed that the aforementioned hold times at 1300°C result in Nb in solution and a prior austenite grain size of 80µm, typical for the CGHAZ[58]. The sample was then cooled to 900°C at 20°C/s under vacuum. It was observed that cooling to 900°C under vacuum resulted in less than 20µm decarburization. Below 900°C, the sample was cooled to room temperature at varying cooling rates. The cooling rate of 3°C/s was attained under vacuum, but faster cooling rates required quenching by helium. Cooling rates of 50°C/s and 100°C/s were not maintained once the transformation started due to the heat of transformation.

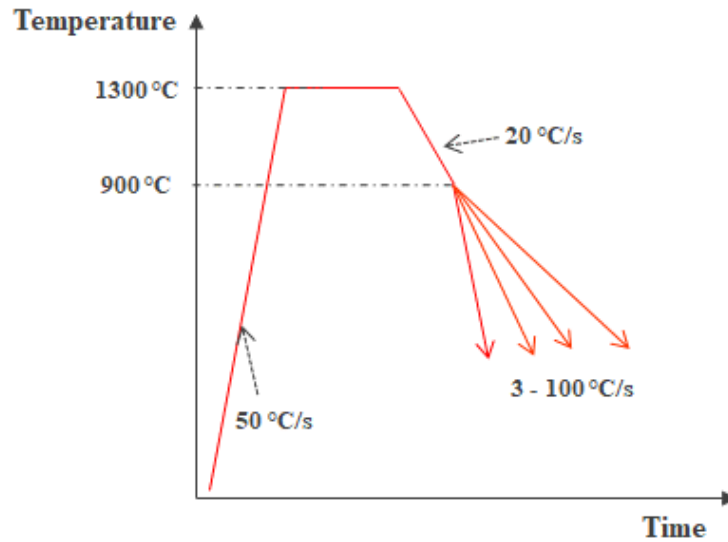


Figure 4.3: Schematic of thermal cycle to simulate austenite decomposition in CGHAZ

4.2.3 Dilatometry

The molar volume of austenite and the decomposition products are different, which results in volume change during austenite decomposition. This change in volume results in a change in dimension of the sample and is measured by a contact dilatometer. As shown in Figure 4.1, the dilatometer is placed at the centre of the sample on the same cross-section where the thermocouple is spot welded. Figure 4.4 shows an example of the dilation data obtained during the cooling of the sample, where the relative change of diameter is plotted against temperature. The relative change in diameter is calculated by normalizing the change in diameter measured by dilatometer with respect to the initial diameter, 8mm. The curve can be divided into two linear segments, one at higher temperature is due to the thermal contraction of the austenite phase, whereas the one at lower temperature is a result of the thermal contraction of the daughter phase(s). Austenite decomposition takes place in the non-linear region between these two linear segments.

The validity of a test is evaluated by measuring the coefficient of thermal expansion (CTE) of the product and parent phase from the dilatometric data. Zhao et. al. [111] measured the CTE for ferrite and austenite as $14.8 \times 10^{-6} \text{ }^\circ\text{C}^{-1}$ and $22.5 \times 10^{-6} \text{ }^\circ\text{C}^{-1}$, respectively, in low carbon steel. For the present study, a test was considered successful if the measured CTE measurements were within 5% of the aforementioned values. The slopes obtained for the example shown in Fig. 4.4 match the CTE within the acceptable error.

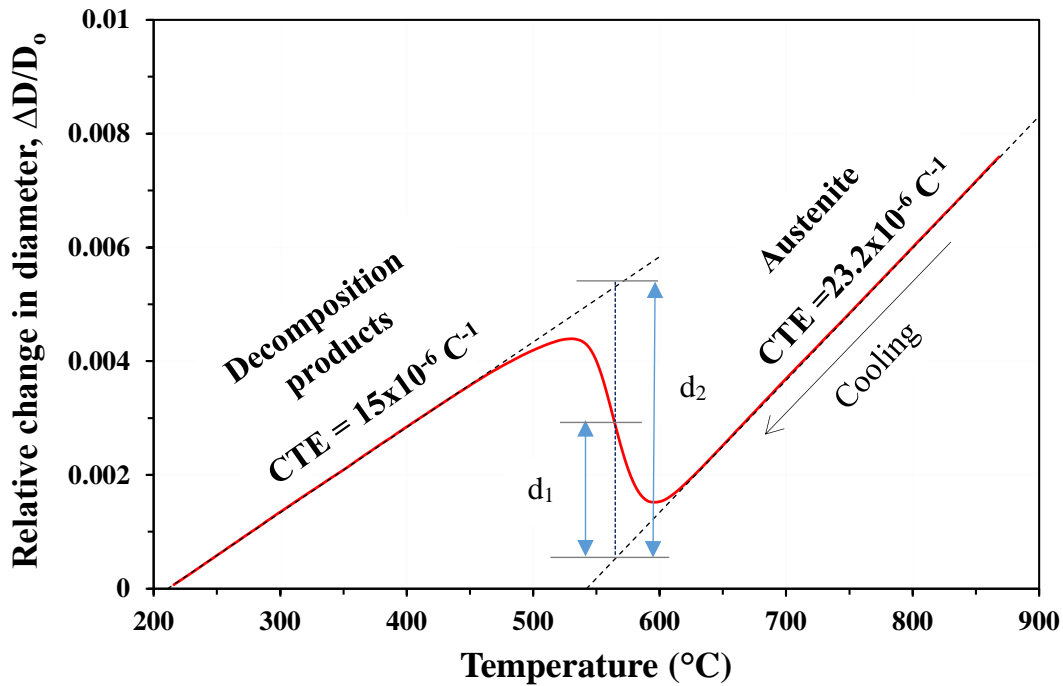


Figure 4.4: Schematic of dilation curve obtained during cooling of Gleeble sample

The Lever rule (ATSM 1033) was used to calculate the fraction transformed from the dilation data. Figure 4.4 shows how the lever rule is applied. At any given temperature, the fraction transformed is given by Equation 4.1.

$$\text{Fraction transformed} = \frac{d_1}{d_2} \quad (4.1)$$

Applying the lever rule over the complete temperature range results in fraction transformed as a function of temperature, which is shown in Figure 4.5. In this study, the temperature at which

5% and 95% transformation is complete is defined as the transformation start and transformation finish temperature, respectively.

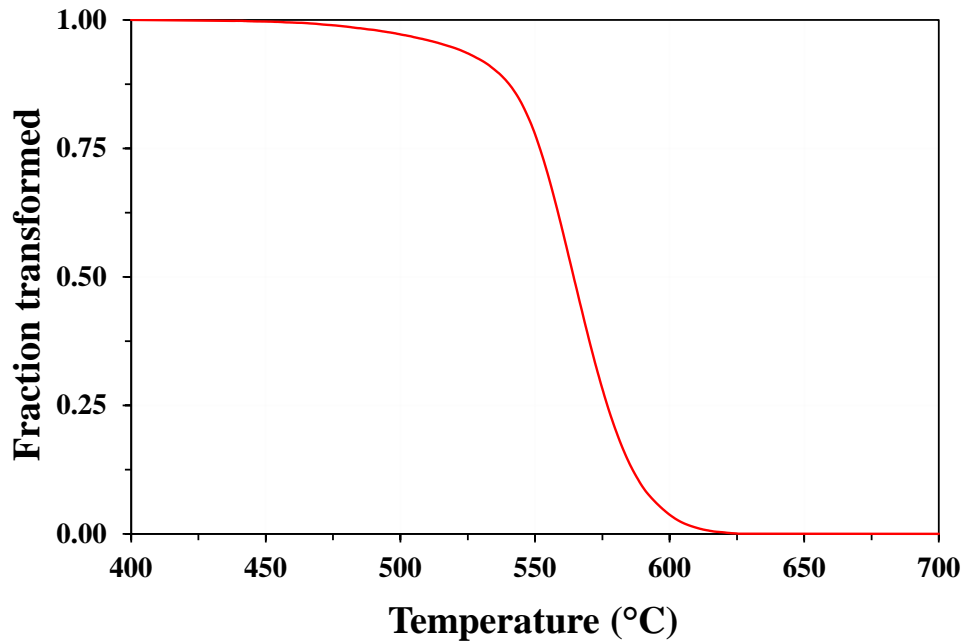


Figure 4.5: Schematic of fraction transformed as a function of temperature obtained by applying the lever rule on dilation data

4.3 Microstructure characterization

4.3.1 Sample preparation

Gleeble-treated tubular samples were sectioned at the centre where the thermocouples were spot welded. Each sample was mounted and then ground and polished on a Buehler polishing machine. Grinding was carried out on progressively finer silicon carbide paper with grit size 320, 600, 800 and 1200 with continuous water flow for lubrication. The sample was then polished using 6 μm followed by 1 μm diamond suspension and a lubricating agent. The sample was washed with liquid soap under running water and then dried with denatured ethyl alcohol after each stage of grinding and polishing to avoid contamination. The polished sample was then etched with 2%

Nital solution for 15 seconds, rinsed with water and denatured ethyl alcohol and then dried. The sample was then observed with a Nikon EPIPHOT 300 series inverted optical microscope to obtain optical images.

In order to measure prior austenite grain size, the prior austenite grain boundaries (PAGB) were revealed on an 1 μ m diamond polished sample by etching it using a solution of 50 ml picric acid, 0.5 gram sodium dodecylbenzenesulfonate and 0.5 ml hydrochloric acid. The etchant was heated to 50 $^{\circ}$ C and the sample was dipped for an interval of 30 seconds, followed by rinsing in water and drying. If the boundaries were not dark enough to be differentiated from the matrix under an optical microscope, the sample was etched for an additional 30 seconds.

The other half of the sectioned sample was mechanically polished till 1 μ m diamond polish, as previously explained. This sample was in an unmounted state and was prepared for EBSD imaging in a scanning electron microscope. The mechanical polishing of the sample resulted in a strained layer on the surface of the sample which was removed by electropolishing. This was pivotal in obtaining a sharp diffraction pattern which is representative of the unstrained material. Electropolishing was performed by dipping the sample in a solution of 95% acetic acid and 5% perchloric acid and applying a 15 V potential difference across the sample for 15 seconds. The sample was immediately washed in water, then rinsed in denatured ethanol and dried.

4.3.2 Optical microscopy imaging

A Nikon EPIPHOT 300 series inverted microscope attached with a digital camera was used to capture optical images. The multi-layer capture feature in the image capturing software, Clemex, was used to obtain focused images. Optical images of Nital etched samples were captured for a qualitative description of the microstructure.

Optical images were captured from the samples prepared to measure the prior austenite grain size. Equivalent area diameter (EQAD) was measured using the ASTM E112-13 standard. At least 250 grains were included for this measurement.

4.3.3 Microstructure imaging using Electron Backscattered Diffraction

EBSD measurements were conducted on the electropolished samples described in Section 4.3.1, using a Zeiss-Sigma field emission gun scanning electron microscope. Images were captured using a Nikon high-speed camera. The data acquisition was carried out by TSL OIM data collection software. The samples were tilted at 70° and a working distance of 10 mm was used to capture the EBSD patterns. An aperture size of 60 μm was used and 20kV accelerating voltage was applied. Diffraction patterns were captured using a binning size 8x8 and ~40 frames per second capture rate. Body centered cubic (BCC) and face centered cubic (FCC) phases were selected as the possible phases for automatic indexing by the OIM software. An area of ~ 200 μm x 150 μm was captured with a step size of 130 nm using a hexagonal grid, resulting in a 15-hour scan time. Finer resolution imaging with a step size of 50 nm was carried out on a smaller area (80 μm x 60 μm) for two conditions to measure the sensitivity of step size on phase fraction and misorientation calculation.

Each point captured by EBSD was assigned a phase, an orientation and parameters identifying the quality of data at that specific point, namely Confidence Index (CI) and Image Quality (IQ). The orientation values of adjacent points can be used to calculate the misorientation between the points. The misorientation information was used to identify grain boundaries and bainitic lath boundaries. Grain boundaries with misorientation between 2°-15° were considered as

low angle grain boundaries (LAGB), whereas those with misorientation $>15^\circ$ were considered as high angle grain boundaries (HAGB).

The post processing of the acquired data was carried out using TSL orientation imaging microscopy (OIM) data analysis software, version 6.2. For the quantification of retained austenite (RA), the RA was identified and separated from the other phases based on its FCC crystal structure. During EBSD ferrite (BCC) and austenite (FCC) phases were selected as the possible phases for automatic indexing by the OIM software. Based on the matching of the Kikuchi pattern, each point was indexed either as BCC or FCC. A cluster of two or more pixels was considered as an object, and the total area fraction of these objects provided the fraction of RA.

A single step cleaning process using grain dilation was used for grain boundary orientation distribution. The cleaning process was done using a grain tolerance angle of 5° and a minimum grain size of two pixels. The ferrite phase of the cleaned data was used to measure the high angle grain boundary density.

Bain group analysis was done using the EBSD data. The detailed process to obtain a Bain group map is discussed in Section 5.6.3.

4.3.4 Hardness measurement

Hardness was measured using a Micro-Vickers hardness indenter under 1 kgf load, applied for a 10 second dwell time. The diagonal length of the indent made by the pyramid-shaped diamond indenter was measured. The hardness value is calculated from the average diagonal length according to [112]

$$\text{Hardness } (Hv) = \frac{1.8544 F}{d_{avg}^2} \quad (4.3)$$

where, F is the load applied in kgf and d_{avg} is the average diagonal length in mm. An average value of a minimum of five indents was reported as the hardness. A minimum of 2.5 diagonal length was maintained between the indents to avoid incorrect hardness measurements as a result of work hardening caused by a previous indent. A gap of 2.5 diagonal lengths from the edge of the sample was maintained to measure the bulk hardness and avoid any edge effects.

4.4 Modelling

A model was developed to describe the austenite decomposition kinetics capturing the effect of carbon, chromium and cooling rate, starting from the previously proposed models by Garcin et al. [96] and Reichert [40], where they incorporated the effects of different levels of niobium in solution, prior austenite grain size and cooling rate. The model presented in this study is divided into two sub-models (a) Bainite start model and (b) Bainite growth model.

The bainite start temperatures (5% transformation) were obtained from the CCT tests for the three steels at six different cooling rates. Bhadeshia [78, 116] showed that bainite nucleation requires approximately 400 J/mol critical driving pressure. Thermo-Calc software (TCFE7 database) was used to calculate the bainite nucleation temperature for all three steels using the critical driving pressure. The bainite start model used the approach developed by Garcin et al. [96], and two fit parameters for each steel were calculated based on root mean square error minimization.

Johnson-Mehl-Avrami-Kolmogorov (JMAK) with the additivity principle was used to model the bainite growth. The rate parameter was expressed as an exponential function of temperature with two fit parameters for each steel. The fit parameters for each steel were calculated based on the least root mean squared error for 50% transformation temperature. An empirical

model was developed to describe the microstructure (HAGB density) and hardness of the steel based on cooling rate and chemistry. The details of this model will be discussed in Chapter 6.

Chapter 5: Experimental results and discussion

5.1 Continuous cooling transformation

This chapter presents the CCT test results for austenite decomposition and microstructural analysis of the decomposition products. A single prior austenite grain size (PAGS) of 80 μm , typically observed in the CGHAZ was chosen. Figure 5.1 shows a micrograph with the PAGB. At least six images were used to calculate the average PAGS for each steel.

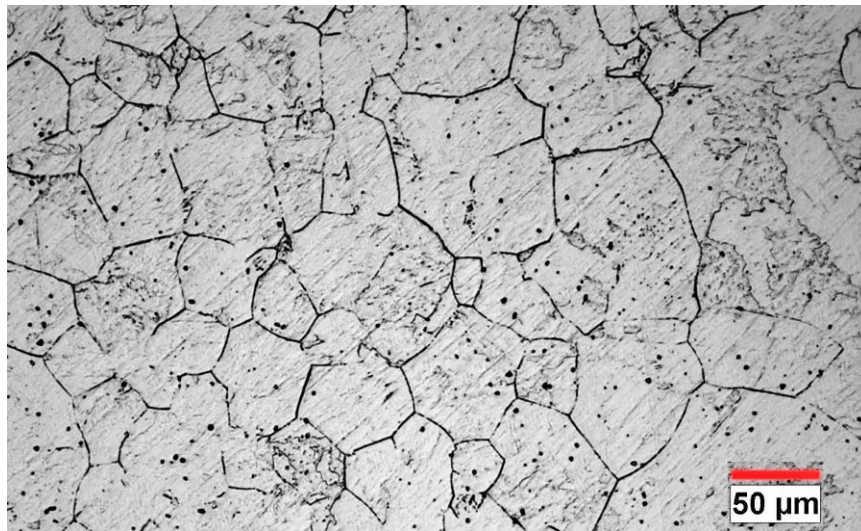


Figure 5.1: Micrograph showing the prior austenite grain boundaries in a L04C08NbMoCr sample

Table 5.1 summarizes the PAGS measured by metallography and by LUMet [57] measurement for all three steels. The EQAD error reported is the standard deviation in PAGS measurement over six micrographs. Romualdi [57] reported the LUMet measurement with the standard deviation due to the spread in the data.

Table 5.1: Metallographic and LUMet [57] measurement of PAGS

Steel	EQAD (μm)	LUMet (μm)
L04C08NbMo	79 \pm 4	80 \pm 6
L04C08NbMoCr	75 \pm 4	80 \pm 7
L06C06NbMo	78 \pm 6	80 \pm 6

For cooling rates up to 30°C/s, a constant cooling rate was maintained throughout the test. Figure 5.2 shows a thermal cycle obtained during the 30°C/s test for L06C06NbMo. A momentary overshoot of 3°C was observed when the programmed temperature reaches 1300°C, followed by $\pm 1^\circ\text{C}$ fluctuation during hold. Similar stability during hold at 1300°C was observed for all tests. Figure 5.2(c) shows that the cooling rate of 30°C/s is maintained throughout cooling.

For nominal cooling rates of 50°C/s and 100°C/s, the cooling rate was not maintained throughout the test as recalescence occurred due to the heat of transformation. Figure 5.3 shows the thermal history of a test carried out at 50°C/s. Similar to the example discussed for the 30°C/s cooling rate, in this case too, there is an initial overshoot of $\sim 3^\circ\text{C}$ on reaching 1300°C followed by a fluctuation of less than $\pm 1^\circ\text{C}$ during holding. During cooling, there is a deviation from the programmed thermal path below 500°C due to recalescence, as shown in Figure 5.3(c), therefore a cooling rate of 50°C/s and above is not maintained during the transformation.

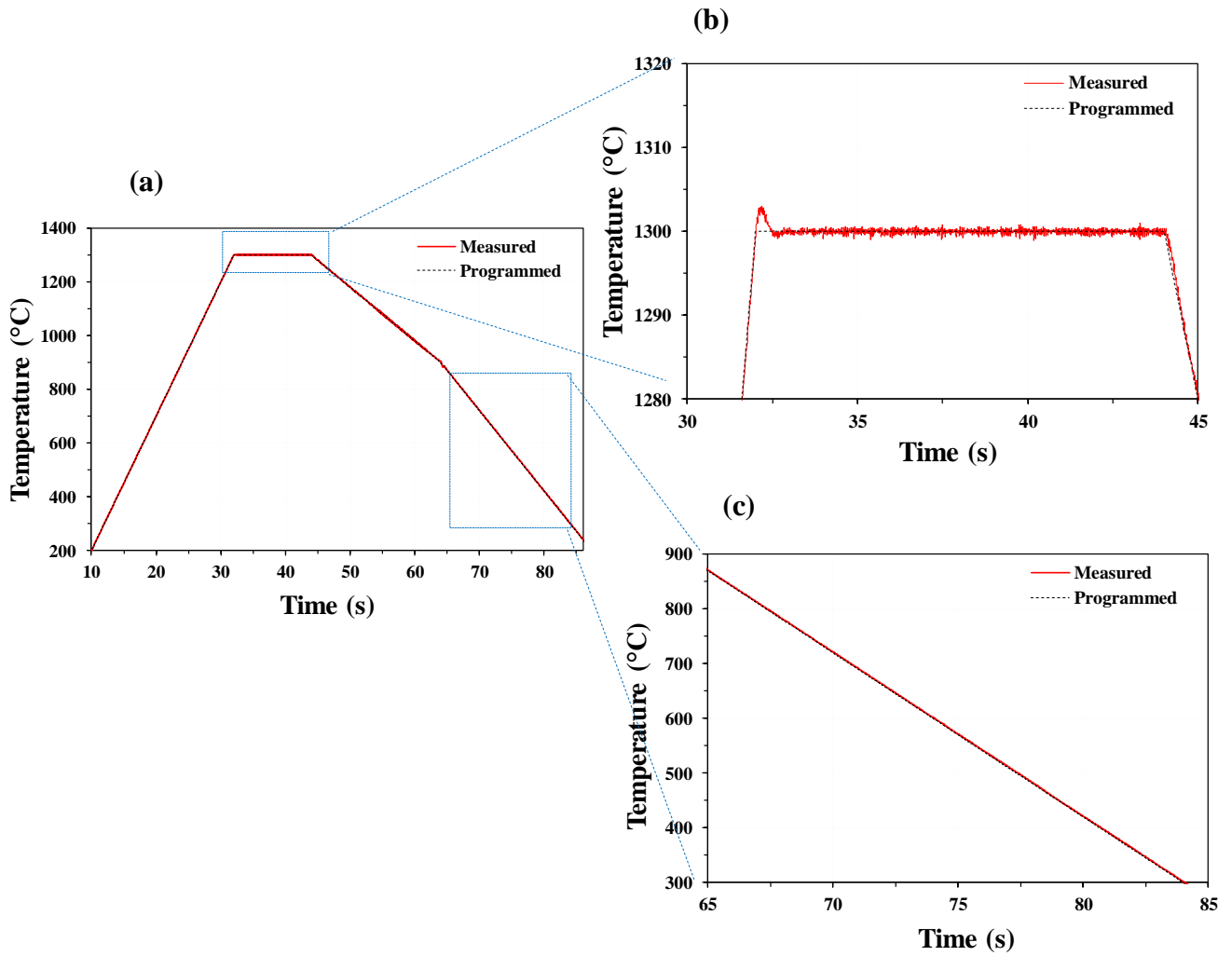


Figure 5.2: Thermal cycle of 30°C/s cooling rate test (a) complete cycle

(b) during isothermal hold (c) during cooling

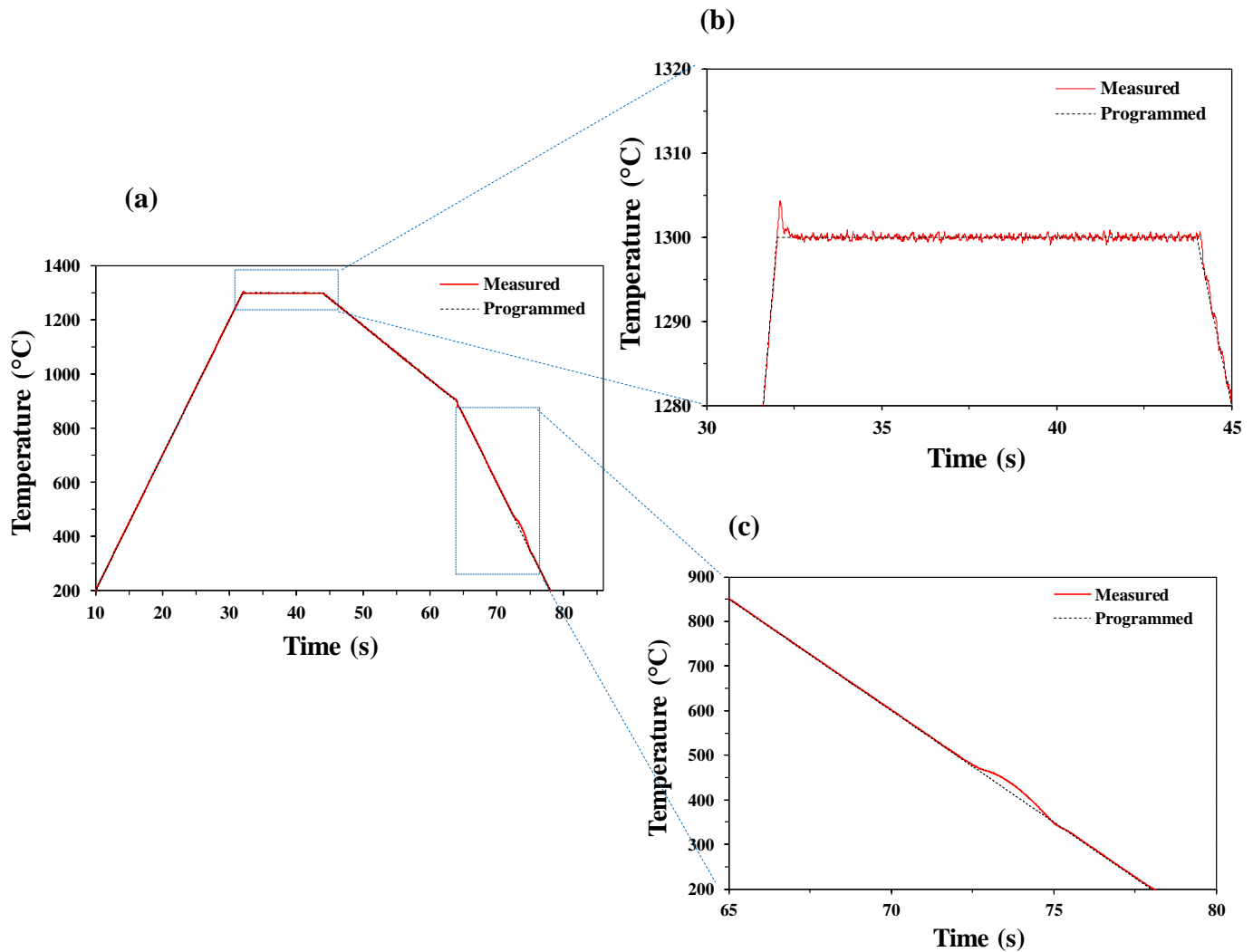


Figure 5.3: Thermal cycle of 50°C/s cooling rate test (a) complete cycle (b) during isothermal hold (c) during cooling

Figure 5.4 shows the deviation from the nominal cooling rates of 50 and 100°C/s. In the case of 50°C/s cooling rate, the actual cooling rate drops as the phase transformation proceeds due to the heat of transformation. On completion of transformation, the system catches up with the programmed path, resulting in a significant increase in cooling rate. Once the system catches up with the programmed path, it stabilizes back to the 50°C/s cooling rate. With the faster cooling

rate of 100°C/s, the heat of transformation is released over a shorter time, resulting in a significant drop in the actual cooling rate to as low as 16°C/s. The system is unable to catch up with the programmed path for the 100°C/s case even after the transformation is complete. This is potentially because the required cooling rate to catch up will be faster than 100°C/s, which the system cannot attain at such a low temperature. The cooling rate was calculated from the recorded time-temperature data. Using the time required for one degree Celsius reduction in temperature, the cooling rate was determined at that specific temperature. This process was repeated for one degree Celsius increments to obtain the complete cooling rate curve.

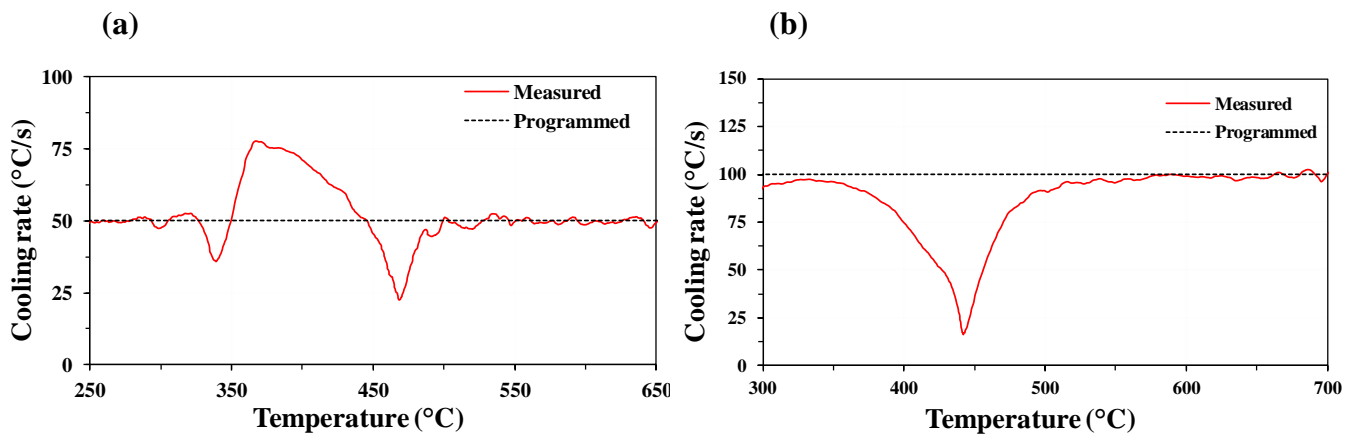


Figure 5.4: Deviation of cooling rate from target cooling rate for (a) 50°C/s and (b) 100°C/s

To determine the accuracy of the CCT tests, five tests were carried out for L06C06NbMo at 30°C/s. Figure 5.5 shows the fraction transformed as a function of temperature. It can be observed that the curves are very similar, and Table 5.2 shows the standard deviation and maximum difference for the 5% (T_5), 50% (T_{50}) and 95% (T_{95}) transformation temperature in these tests.

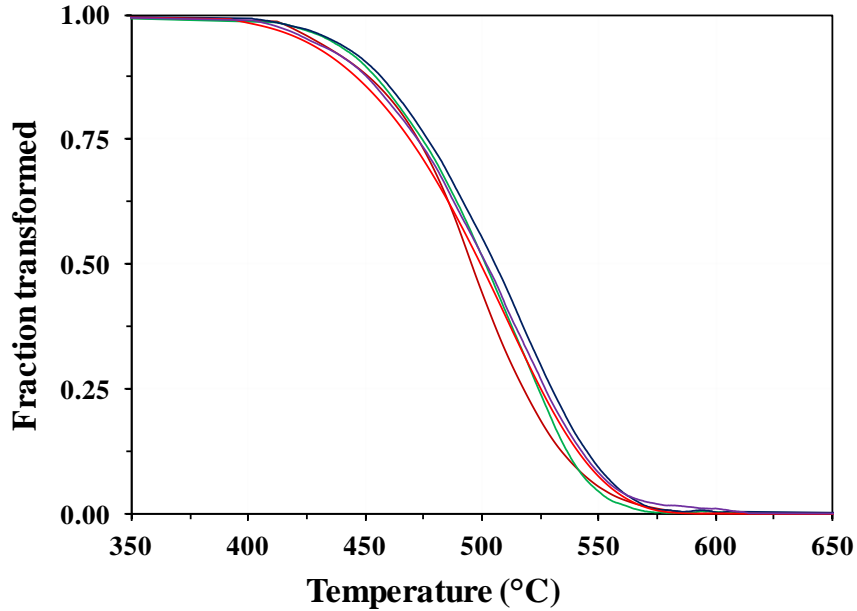


Figure 5.5: Repeat tests at 30°C/s for L06C06NbMo showing test to test variability

The maximum standard deviation of 5°C is obtained at 95% transformation temperature and this value is used to report the accuracy of transformation temperatures in the present work.

Table 5.2: Variability during multiple tests for same steel and thermal cycle

	Standard deviation (°C)	Maximum – minimum (°C)
T₅	4	10
T₅₀	3	10
T₉₅	5	12

5.2 Effect of cooling rate on austenite decomposition kinetics

Figure 5.6 shows the effect of cooling rate on austenite decomposition kinetics for the L06C06NbMo steel. With increasing cooling rate, the transformation is shifted to lower temperature, except at fractions transformed greater than 75% for 50°C/s and 100°C/s. For these high cooling rates, recalescence due to the heat of transformation results in a decrease of cooling rate once transformation starts, as shown in Figure 5.4. For the 50°C/s and 100°C/s nominal

cooling rates, the actual cooling rate drops as low as 22°C/s and 16°C/s, respectively. This significant drop in the cooling rate is due to the higher transformation rate for 50°C/s and 100°C/s compared to 30°C/s, resulting in the heat of transformation released over a short time interval. The system cannot extract this excess heat generated rapidly over a short time, leading to the cooling rate dropping even below 30°C/s. The significant decrease in cooling rate leads to an overlap of transformation curves for the 30, 50 and 100°C/s cases during the later stages of transformation.

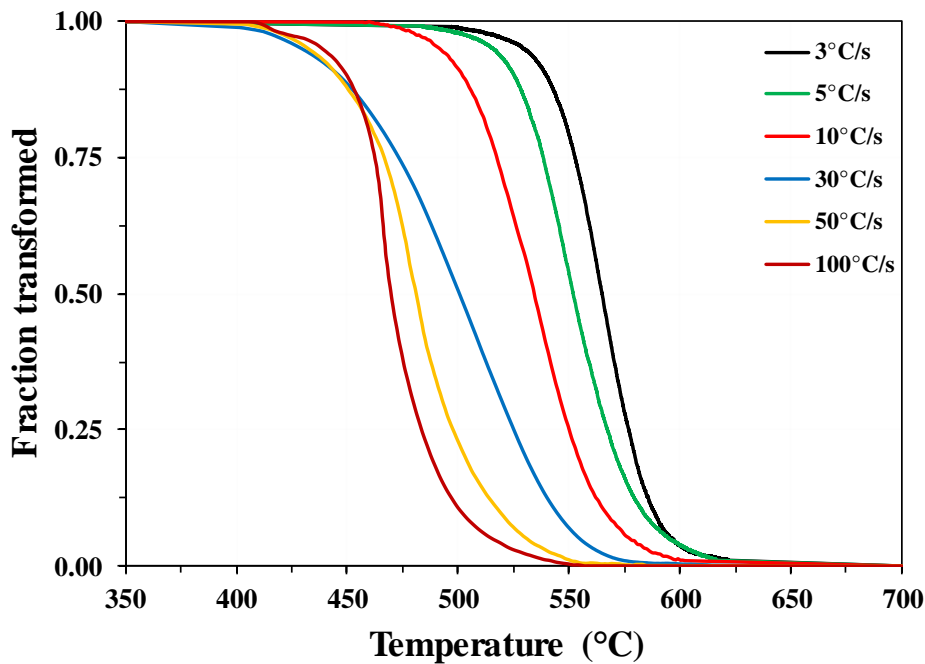
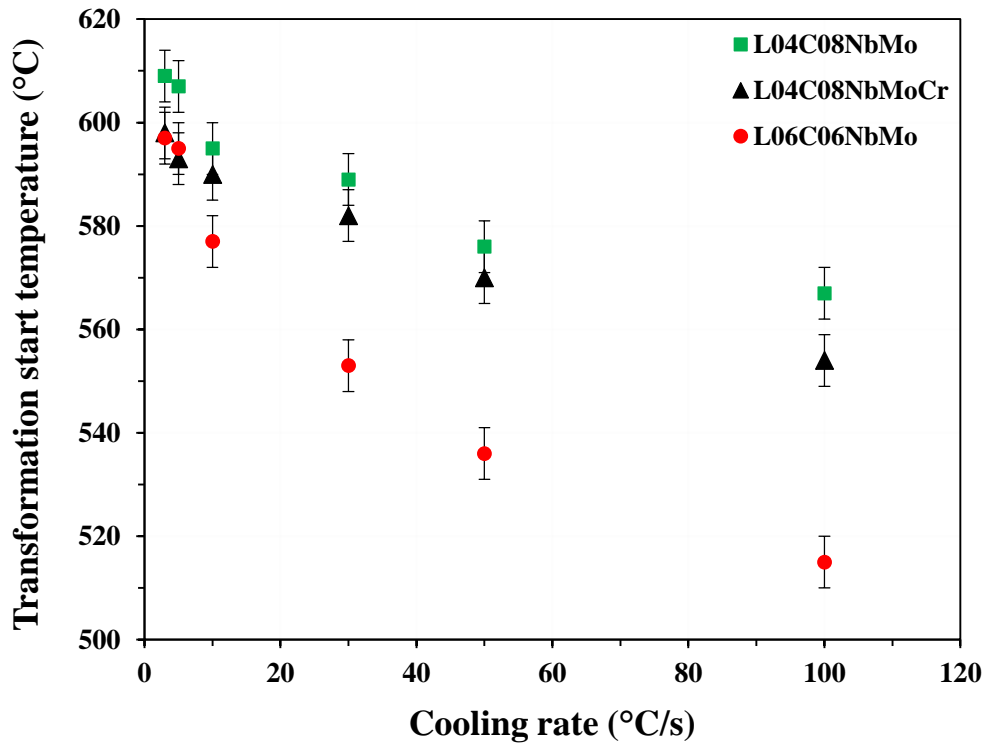


Figure 5.6: Effect of cooling rate on austenite decomposition kinetics in L06C06NbMo

The shift of transformation curves to lower temperature with increasing cooling rate is also observed for the other two steels, L04C08NbMo and L04C08NbMoCr, albeit the shift is less compared to L06C06NbMo. The effect of cooling rate on transformation start temperature (T_5) for all three steels is shown in Figure 5.7. There is a decrease in transformation start temperature with increase in cooling rate for all three steels. At the slowest cooling rate of 3°C/s, all three steels have similar transformation start temperatures, i.e. 609°C, 598°C and 597°C for L04C08NbMo, L04C08NbMoCr and L06C06NbMo, respectively. With an increase in the cooling rate from 3°C/s

to 100°C/s, there is a reduction in the transformation start temperature by 42°C, 44°C and 82°C for L04C08NbMo, L04C08NbMoCr and L06C06NbMo, respectively, indicating that the transformation start temperature decreases significantly more for the steel with higher carbon content.



**Figure 5.7: Effect of cooling rate on transformation start temperature (5%)
for the three steels**

The 50% transformation temperature and the 95% transformation temperature also decrease with increasing cooling rate, as shown in Figures 5.8 and 5.9. Cooling rates of 50°C/s and 100°C/s results are not included in these two plots, since those cooling rates could not be maintained during transformation, as discussed previously. Similar to the 5% transformation temperature, the 50% and 95% transformation temperatures also show a minute chemistry effect at lower cooling rates, whereas the effect of carbon content is more pronounced at higher cooling rates.

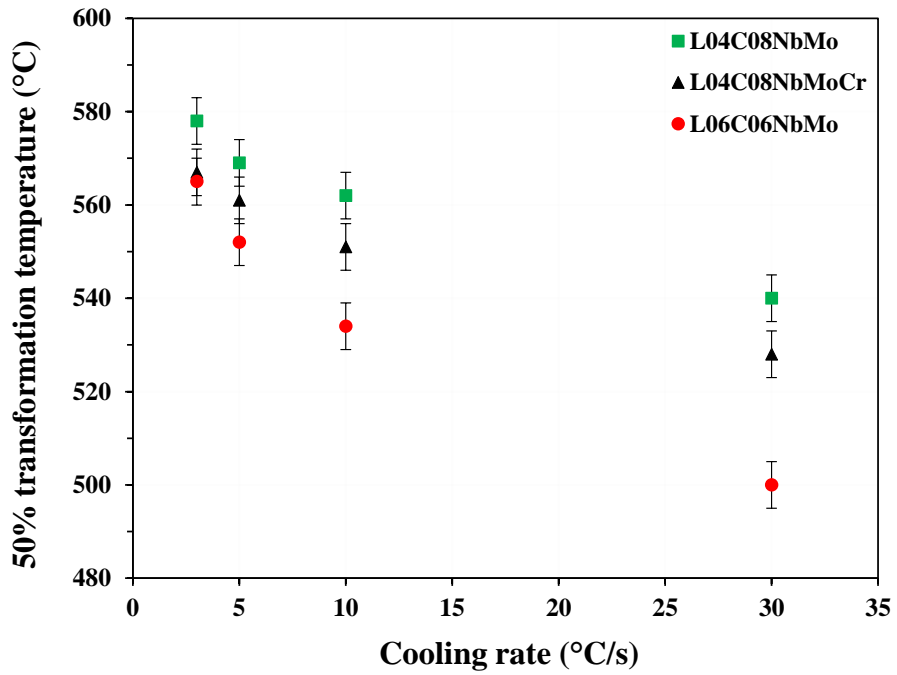


Figure 5.8: Effect of cooling rate on 50% transformation temperature for the three steel

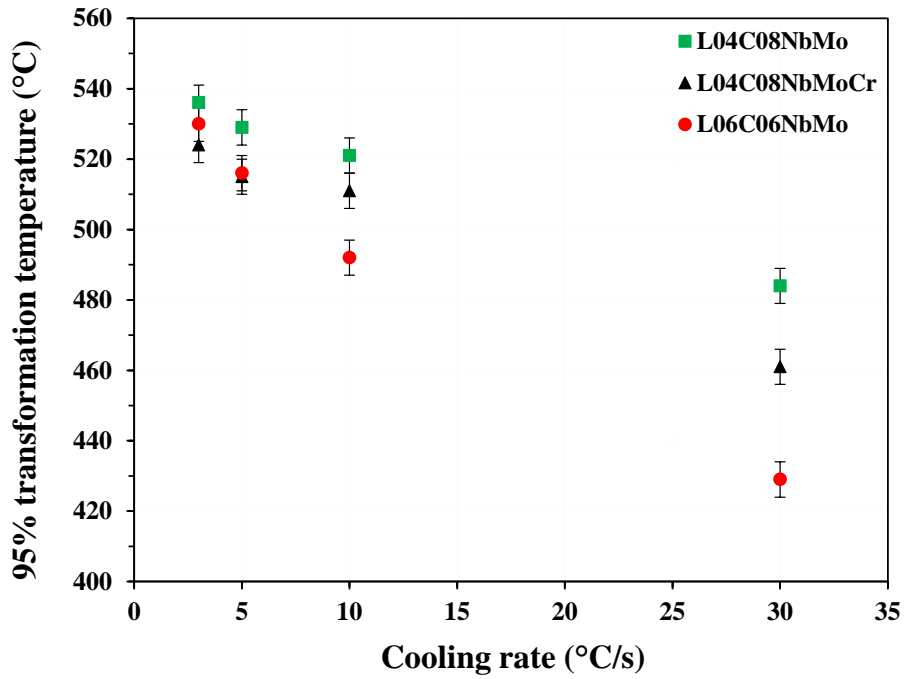


Figure 5.9: Effect of cooling rate on 95% transformation temperature for the three steels

5.3 Effect of carbon content on austenite decomposition kinetics

L04C08NbMo and L06C06NbMo are compared to study the effect of carbon content on austenite decomposition kinetics. Figure 5.10 shows that an increase in carbon content from 0.035wt% to 0.061wt% pushes the transformation temperature to a lower temperature for any given cooling rate. An increase in cooling rate results in a shift of the transformation curves to a lower temperature for both chemistries; however, the shift is more pronounced in the higher carbon steel. The increase in carbon content lowers the transformation start temperature by 12 °C for 3 °C/s and 52 °C for 100°C/s, respectively. Cooling rates faster than 30°C/s are not shown in Figure 5.9 since those cooling rates were not maintained throughout transformation, as discussed in section 5.2.

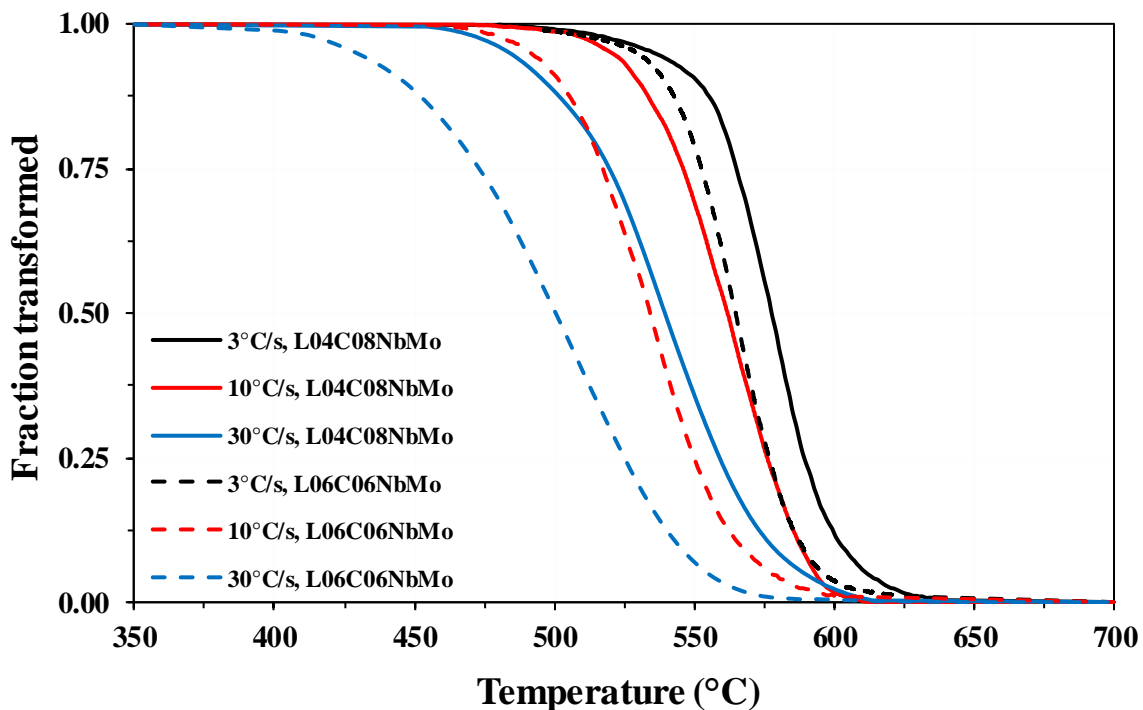


Figure 5.10: Effect of carbon content on transformation kinetics at different cooling rates

5.4 Effect of chromium content on austenite decomposition kinetics

The effect of chromium content is studied by comparing the transformation kinetics of L04C08NbMo and L04C08NbMoCr with chromium contents of 0.023wt% and 0.24wt%, respectively. Increase in chromium content results in a shift of the transformation curve to a lower temperature. The reduction in 5%, 50% and 95% transformation temperatures with an increase in chromium content is consistently close to 10°C, irrespective of cooling rate, as seen in Figure 5.11.

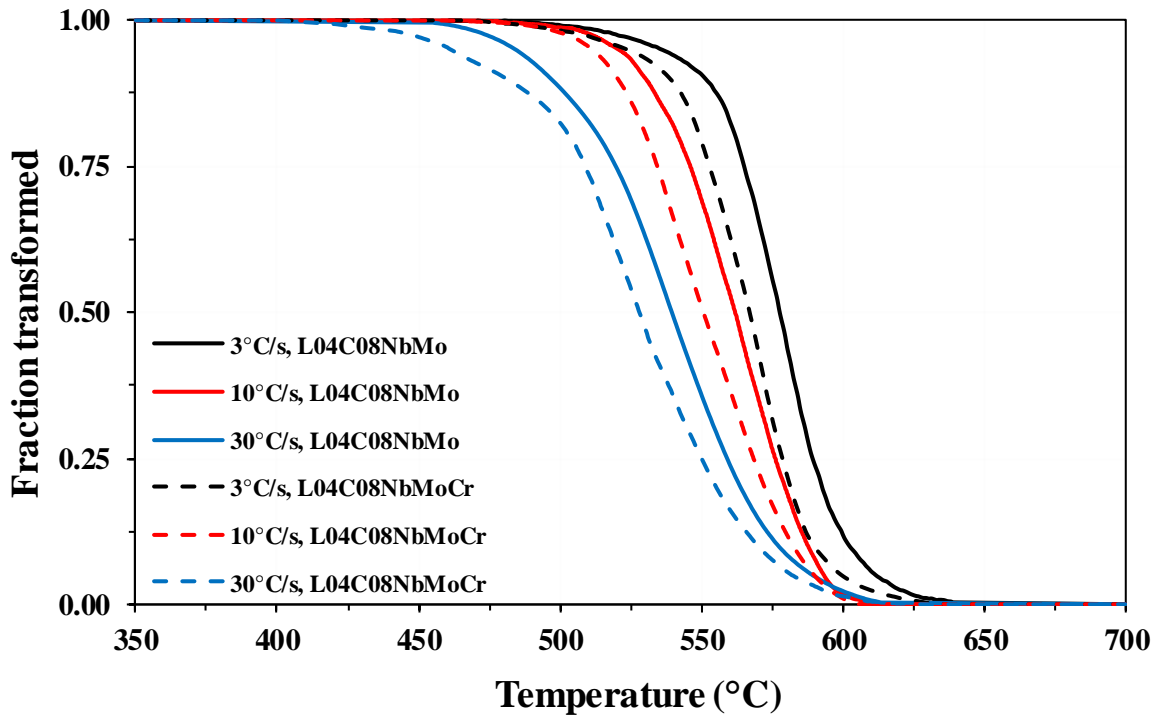


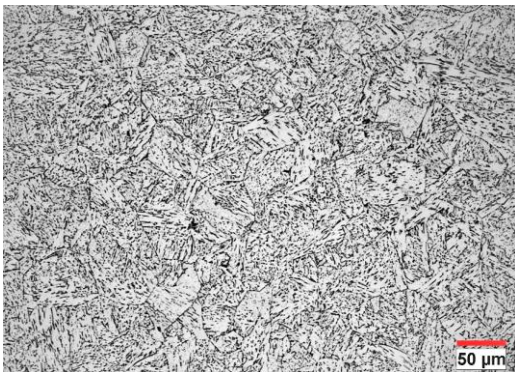
Figure 5.11: Effect of chromium content on transformation kinetics at different cooling rates

In contrast to the effect of carbon, where the increase in cooling rate resulted in a more pronounced effect on lowering of transformation temperature, the effect of chromium on lowering the transformation temperature is practically independent of the cooling rate.

5.5 Optical microstructure characterization

Figure 5.12 shows the optical micrographs for L06C06NbMo. It can be seen that the microstructure gets progressively refined as the cooling rate is increased from 3°C/s to 100°C/s. Refinement of microstructure is also observed for the other two steels as the cooling rate increased. A detailed comparison of microstructure between steels is presented in the following sections. It is necessary to be able to quantify the microstructure to gain better insight; therefore, advanced microstructure characterization using EBSD was carried out and the results are discussed in the following section.

(a) 3 °C/s



(b) 10 °C/s



(c) 30 °C/s



(d) 100 °C/s



Figure 5.12: Optical microstructure for L06C06NbMo at different cooling rates

(a) 3°C/s, (b) 10°C/s, (c) 30°C/s and (d) 100°C/s

5.6 EBSD characterization of transformation products

As seen in the previous section, optical micrography does not provide a quantitative way to describe the microstructure. Therefore, EBSD was used to provide a quantitative description of the microstructure of the different transformation products obtained. EBSD characterization was carried out for cooling rates of 3, 10, 30 and 100°C/s for each steel.

5.6.1 Inverse pole figure maps

Figure 5.13 shows the inverse pole figure (IPF) maps obtained for the decomposition products of L06C06NbMo cooled at 3, 10, 30 and 100°C/s. For slower cooling rates, the steel has a blocky structure with uniform color gradient within a block, indicating similar orientation within the block. For rapid cooling rates, finer elongated lath-like structures with different orientation in adjacent laths were observed. It was also seen that certain conditions led to mixed microstructure, with some regions showing blocky structures whereas other regions had lath-like structure. Examples of such mixed microstructures can be seen at 10 and 30°C/s for high carbon L06C06NbMo (Figure 5.13b-c).

Figure 5.14 shows the IPF map for the two lower carbon steels at 100°C/s. Both are visibly similar, having a mixed microstructure, with some regions having fine laths whereas other regions are blocky. When these two images are compared with the higher carbon steel at 100 °C/s (Figure 5.13d), it is observed that the increase in carbon results in a much finer microstructure. This indicates that an increase in chromium does not affect the microstructure significantly, whereas an increase in carbon content refines the microstructure.

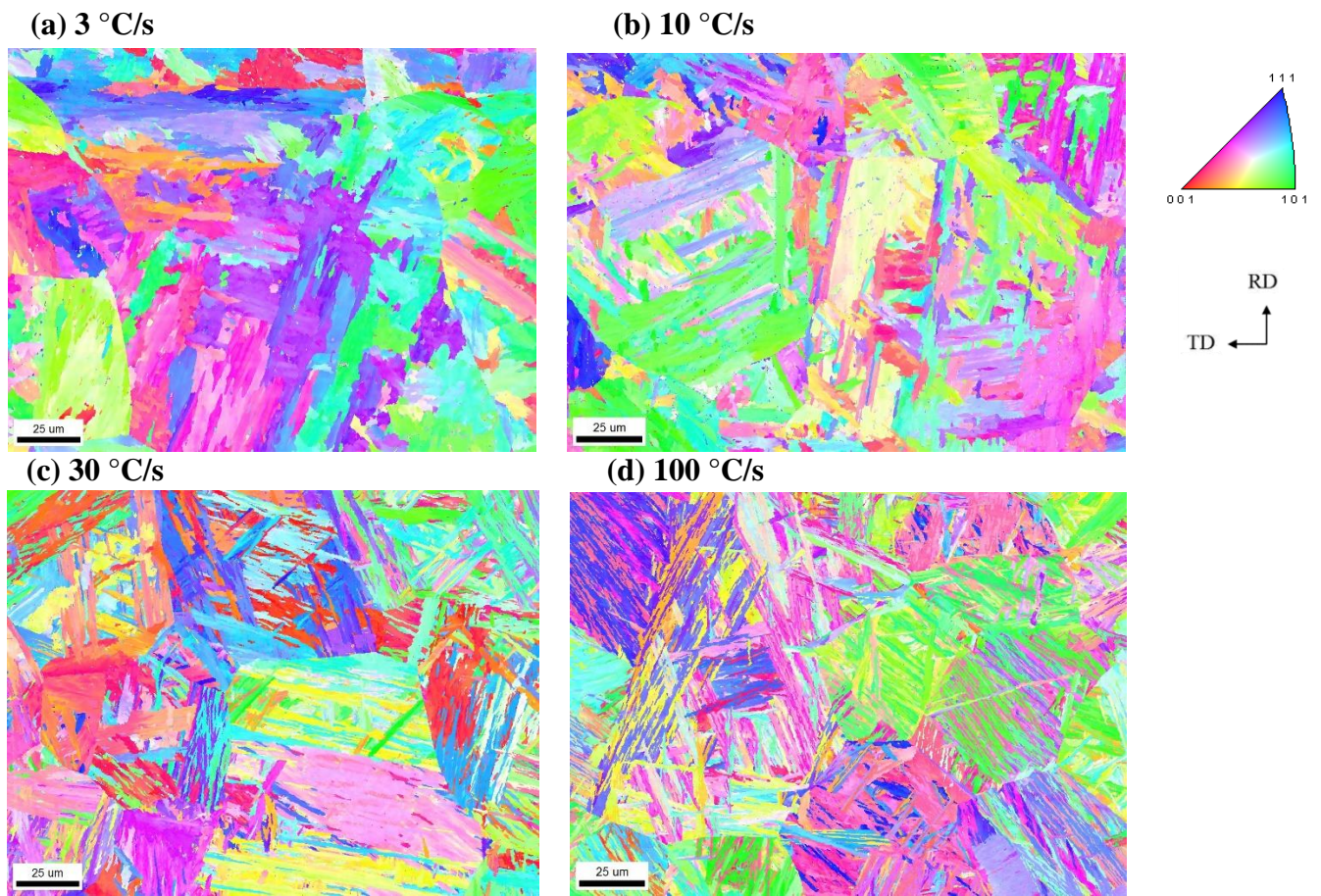


Figure 5.13: Inverse pole figure map for L06C06NbMo at different cooling rates

(a) 3°C/s, (b) 10°C/s, (c) 30°C/s and (d) 100°C/s

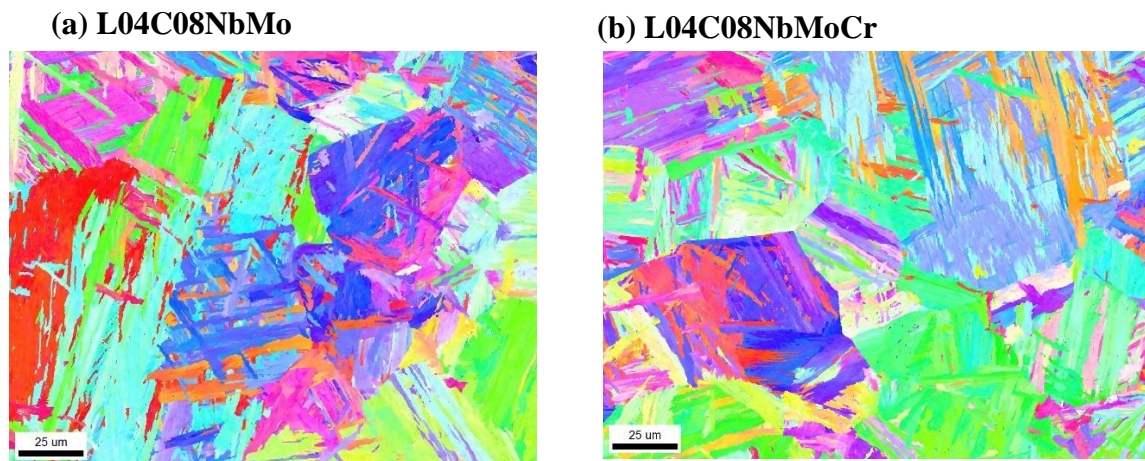


Figure 5.14: Inverse pole figure maps at 100°C/s for

(a) L04C08NbMo and (b) L04C08NbMoCr

5.6.2 Retained austenite

During cooling, austenite might not decompose completely, resulting in some retained austenite in the final microstructure. It was observed that the area fraction of retained austenite for all twelve conditions investigated was lower than 1.3%. Figure 5.15 shows the IPF maps for retained austenite in L06C06NbMo steel cooled at 3, 10, 30 and 100°C/s. The amount of retained austenite decreases from approximately 1% to 0.1% as the cooling rate increases from 3 to 100°C/s for all three steels studied. The retained austenite is useful for identifying the orientation of the parent material and is used during Bain group analysis discussed in the next section.

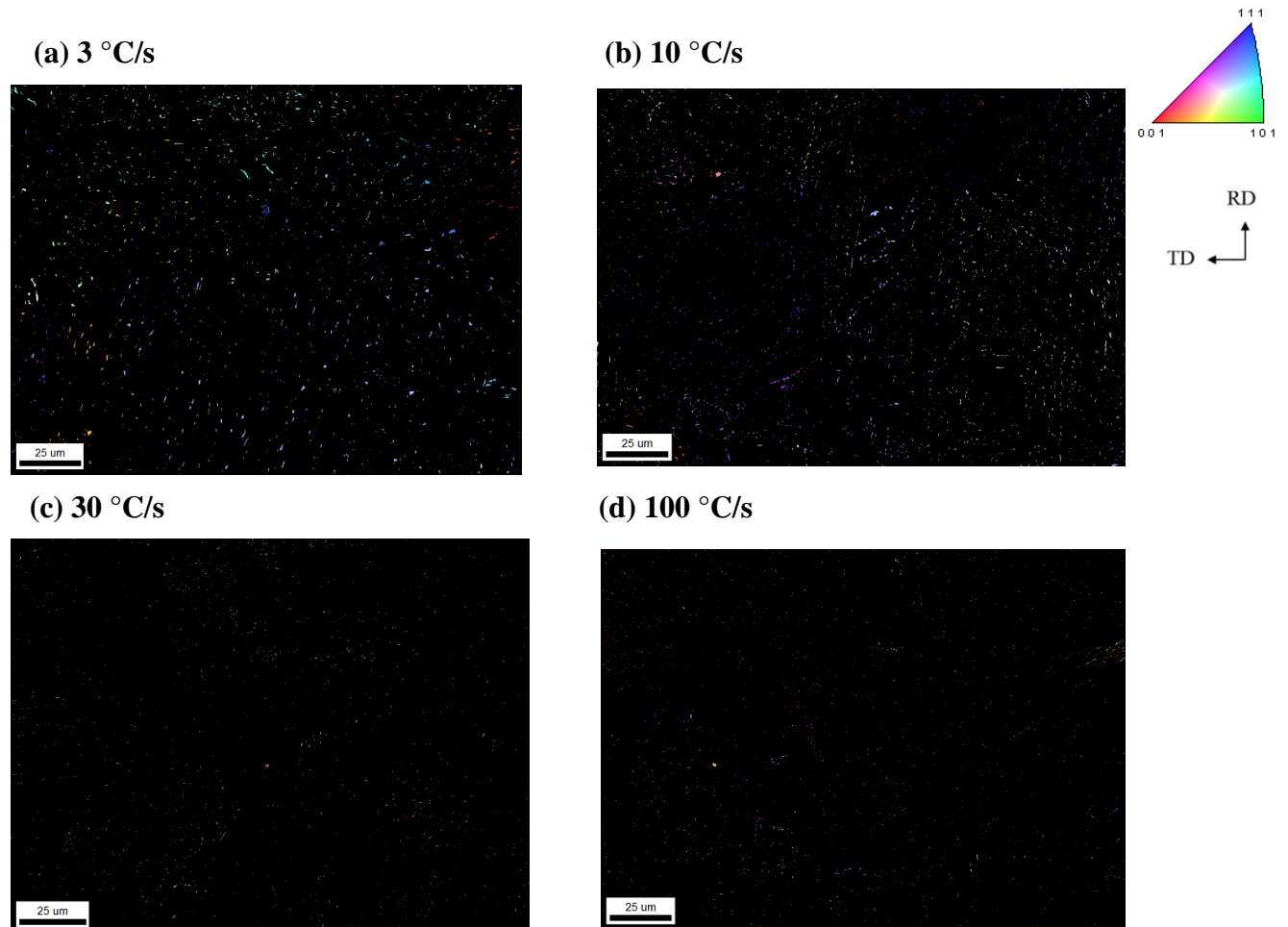


Figure 5.15: Retained austenite in L06C06NbMo at different cooling rates

(a) 3°C/s, (b) 10°C/s, (c) 30°C/s and (d) 100°C/s

5.6.3 Orientation relationship between parent and product phase

Austenite decomposes to bainitic ferrite with an orientation relationship close to the Kurdjumov-Sachs orientation relationship (KS OR). The presence of retained austenite helps identify the parent austenite orientation without the need for austenite reconstruction. In order to investigate the resultant orientation in the product, a single grain was identified within the EBSD map based on the retained austenite orientation. According to KS OR relationship, a particular orientation of parent austenite can result in 24 possible variants in the daughter phase, which is calculated theoretically fulfilling the $\{111\}_\gamma \parallel \{011\}_\alpha <101>_\gamma \parallel <111>_\alpha$ orientation relationship. Figure 5.16a shows the selected grain in the IPF map having the same orientation of retained austenite, as shown in Figure 5.16b, for L04C08NbMoCr cooled at 3°C/s. Figure 5.16c shows the theoretical orientation in a (001) pole figure. The orientation for parent austenite grain is shown with the three green dots, and the 24 possible transformation variants are shown as open circles. Figure 5.16d shows a comparison of the theoretical variants in the (001) pole figure overlaid with the orientation obtained from experiment. The 24 variants were grouped into three main Bain groups, each containing eight variants, shown in blue, red and yellow. It was found that the observed orientation matches very well with the theoretical orientation, indicating that bainitic ferrite following KS OR has been obtained. The Bain map shows all three Bain groups present for this condition, as shown in Figure 5.16e.

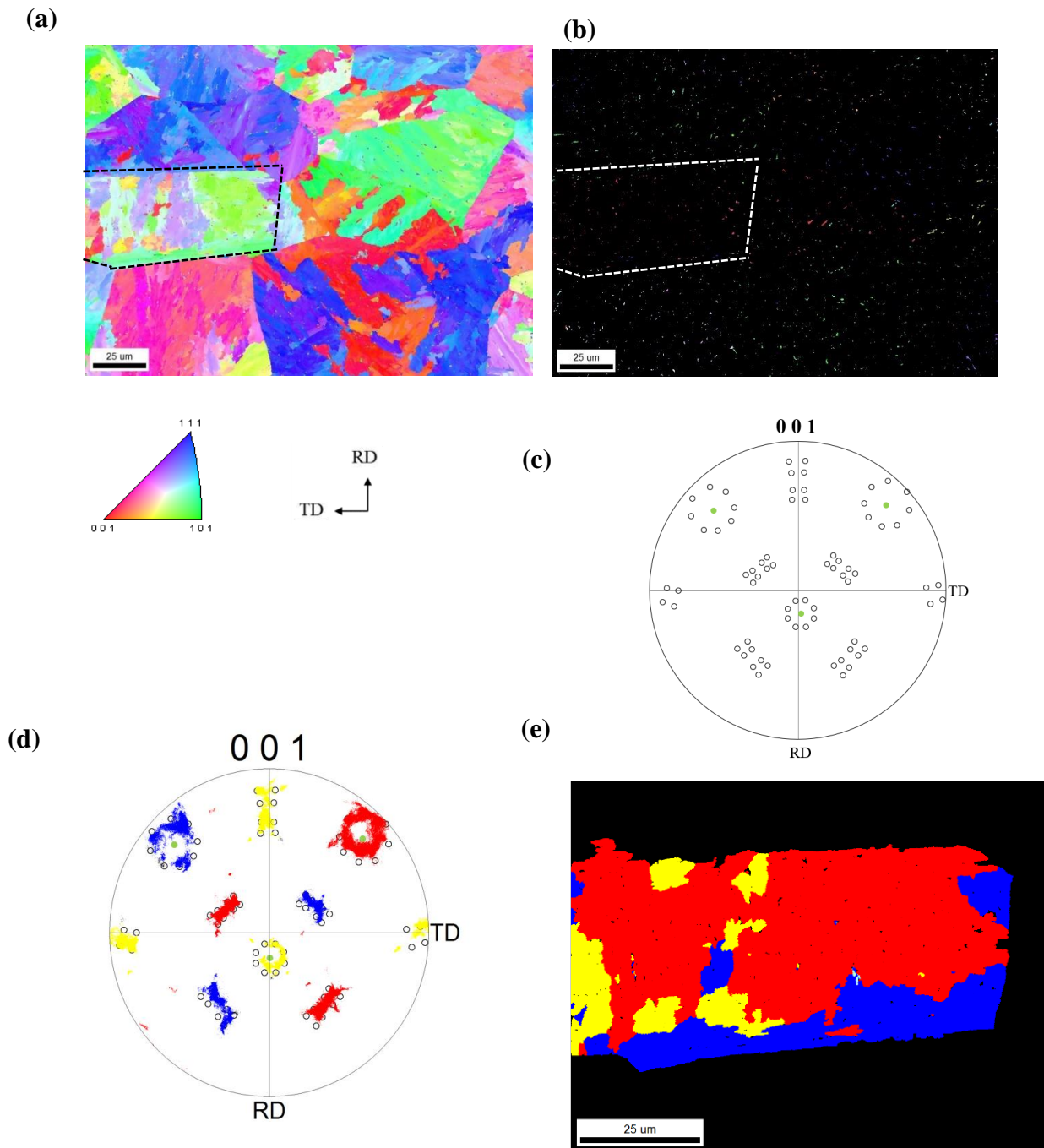


Figure 5.16: (a) IPF map and (b) IPF map for retained austenite, with a selected prior austenite grain shown in dotted line; (c) theoretical (001) pole figure (black circles indicating the 24 KS variants and green dots indicate the orientation of parent grain); (d) (001) pole figure of selected grain overlaid on theoretical pole figure; (e) Bain map for the selected grain. (For L04C08NbMoCr cooled at 3°C/s)

Bain group analysis was carried out for the three steels. Figure 5.17 shows the result obtained for one of the steels, L06C06NbMo. Some deviation from the ideal KS relationship is observed and this is consistent with the results reported by Takayama [80]. Larger deviation from ideal KS relation is observed at faster cooling rates, potentially due to the presence of more laths. All three Bain groups are observed at all cooling rates, albeit not all Bain groups are equally present in most of the cases. L06C06NbMo had coarse blocky regions of a Bain group at 3°C/s. Cooling rates of 10°C/s and 30°C/s resulted in a mixed microstructure with certain regions having blocky distributions of Bain groups, while others consisted of lath-like structures. The 100°C/s cooling rate for L06C06NbMo resulted in a fine lath-like structure with relatively similar amounts of all three Bain groups. This indicates an increase in cooling rate favours the formation of variants of different Bain groups adjacent to each other.

Figure 5.18 shows the Bain map for L04C08NbMo and L04C08NbMoCr at 100°C/s. Both of them have a similar mixed microstructure with certain regions having a blocky structure while other regions have a lath like structure. L04C08NbMo and L04C08NbMoCr resulted in similar Bain maps for a given cooling rate. Compared to the two lower carbon steels, L04C08NbMo and L04C08NbMoCr, the higher carbon steel, L06C06NbMo has a finer uniform lath like structure at 100°C/s (Figure 5.17g). This suggests that an increase in carbon results in a decrease in transformation temperature, which in turn favors variants of different Bain groups forming adjacent to each other more densely, whereas change in the chromium content does not affect the Bain group distribution considerably.

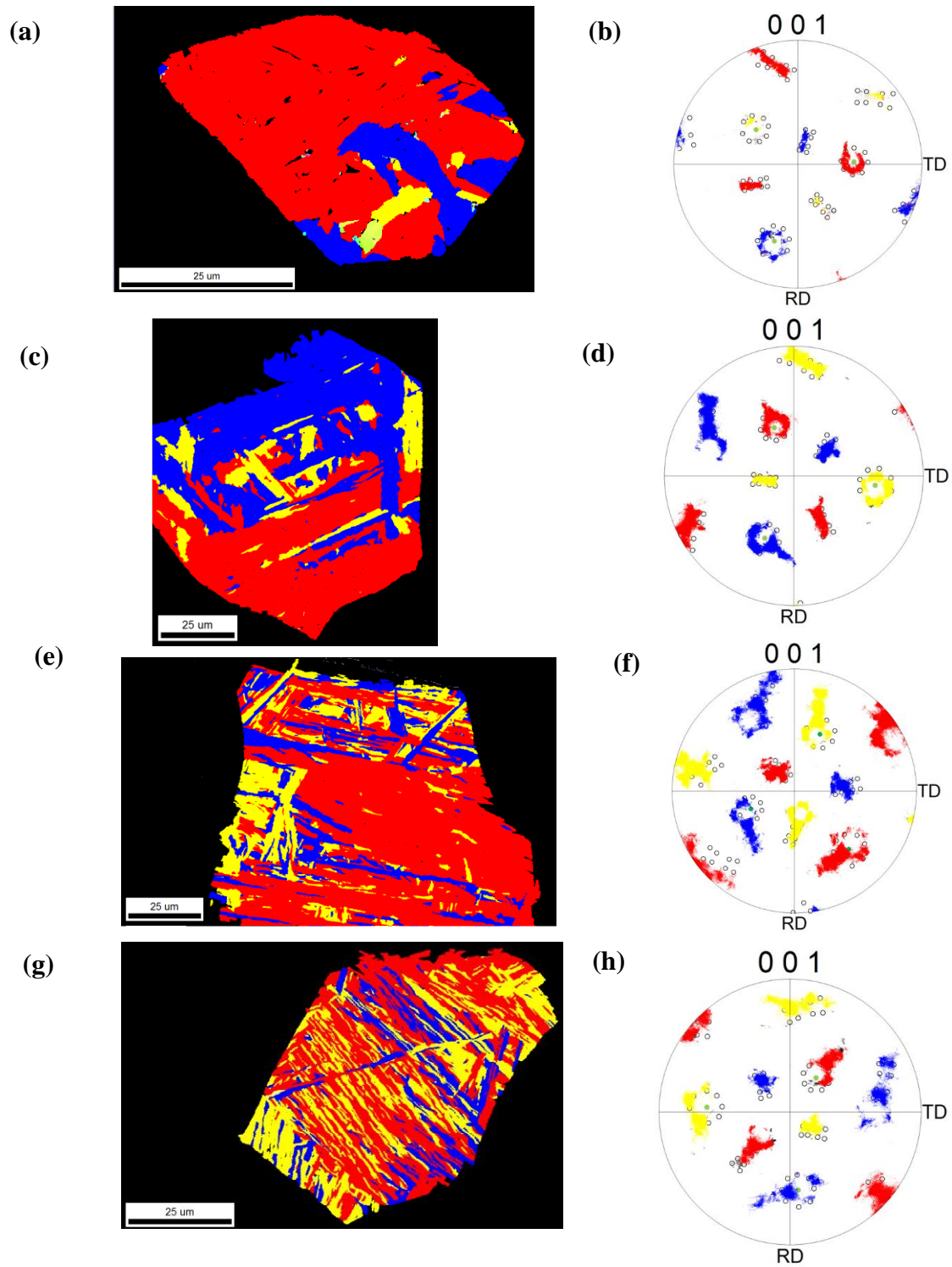


Figure 5.17: Bain group maps and corresponding pole figures for L06C06NbMo cooled at (a, b) 3°C/s, (c, d) 10°C/s, (e, f) 30°C/s and (g, h) 100°C/s

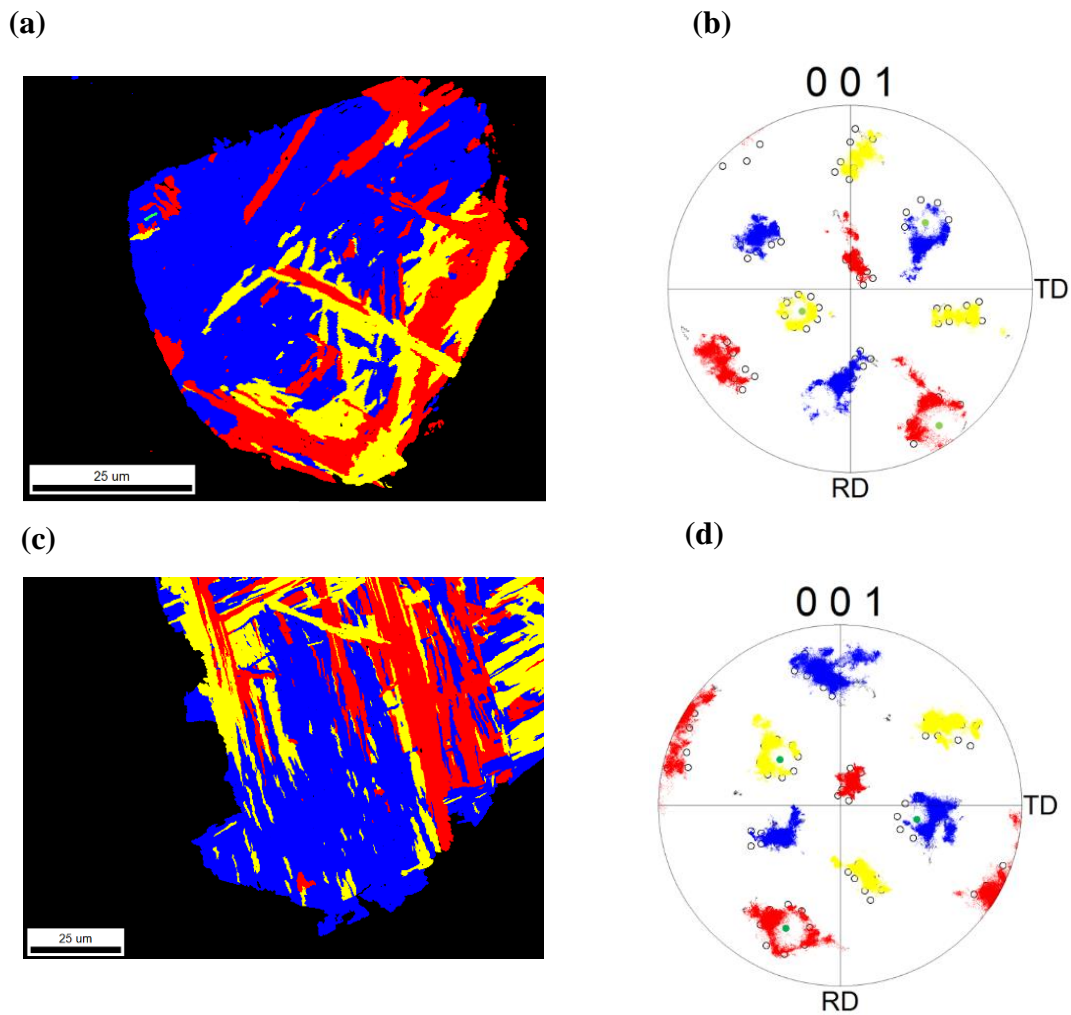


Figure 5.18: Bain group maps and corresponding pole figures cooled at 100°C/s for (a, b) L04C08NbMo and (c, d) L04C08NbMoCr

5.6.4 Spatial distribution of misorientation

Figure 5.19 shows the misorientation angle maps for L06C06NbMo at different cooling rates. High angle grain boundaries, shown in black, have rotation angles greater than 15°. It is observed that the structure is refined with an increase in cooling rate. At the slowest cooling rate of 3°C/s, HAGBs are mostly outlining the prior austenite grain boundaries. Within a prior austenite

grain, some coarse lath structures can be seen in black. As cooling rate increases from 3°C/s to 100°C/s, the microstructure gets progressively more refined with higher amounts of HAGB.

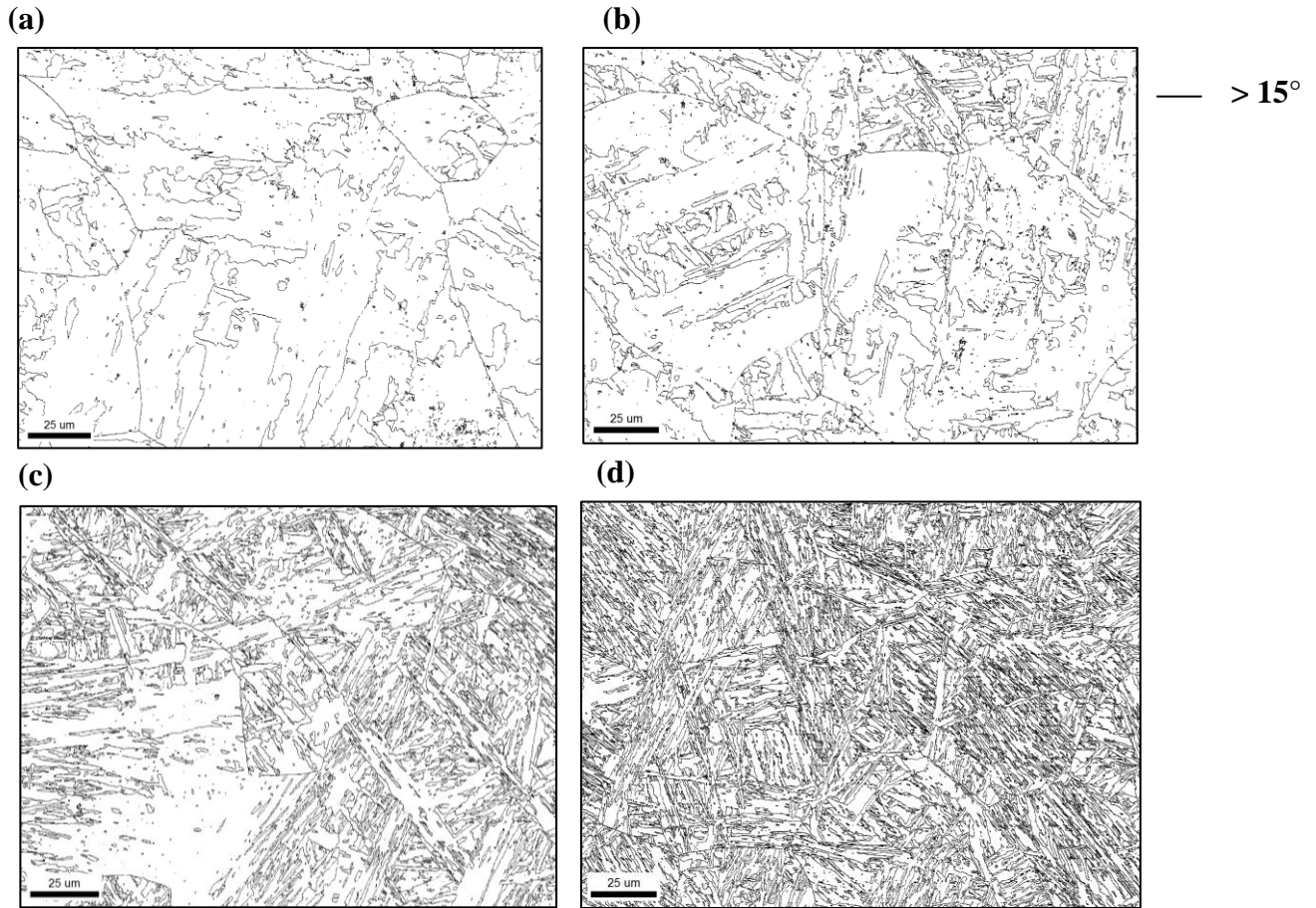


Figure 5.19: Misorientation angle maps for L06C06NbMo at different cooling rates

(a) 3°C/s, (b) 10°C/s, (c) 30°C/s and (d) 100°C/s

Figure 5.20 presents the misorientation map for L04C08NbMo and L04C08NbMoCr cooled at 100°C/s. Both these conditions have less HAGB density compared to higher carbon steel, L06C06NbMo cooled at 100°C/s (Figure 5.19d), indicating that an increase in carbon content leads to an increase in HAGB density. The two lower carbon steels, L04C08NbMo and L04C08NbMoCr, appear to have relatively similar misorientation distribution.

(a) L04C08NbMo

(b) L04C08NbMoCr

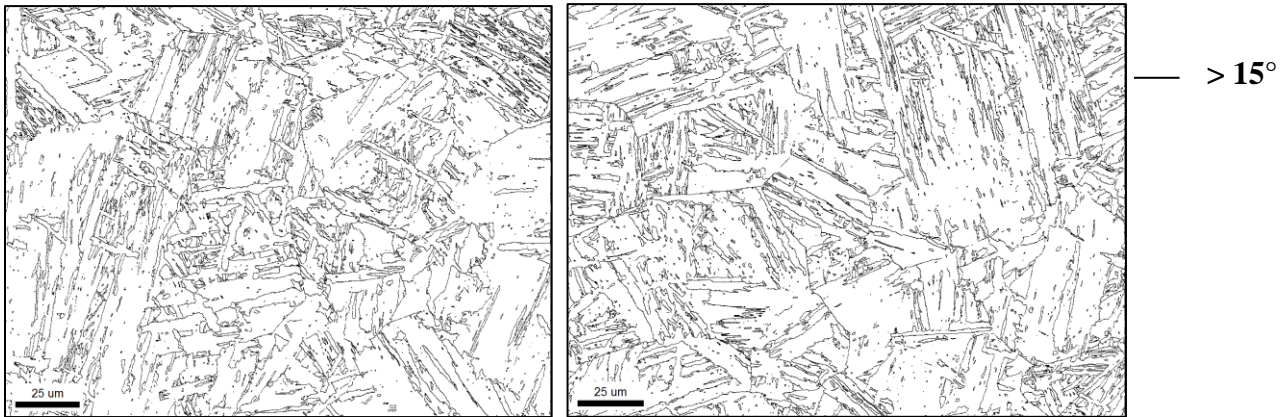


Figure 5.20: Misorientation angle maps at 100°C/s for

(a) L04C08NbMo and (b) L04C08NbMoCr

The quantitative distribution of misorientation angles for all three steels cooled at four different cooling rates is shown in Figure 5.21. Figure 5.21a presents the fraction of given misorientation angles occurring in all three steels cooled at 3°C/s. The figure shows that there is a peak for LAGB, followed by absence of any major misorientation peak till 50°. Two peaks with similar intensity are observed at ~54° and ~59° for all three steels with similar intensity, indicating that the microstructure is relatively similar at 3°C/s, irrespective of the chemistry. This is consistent with the observation that the transformation start temperature is similar for all three steels at 3°C/s. The two peaks observed at ~54° and ~59° are consistent with the peaks reported by Takayama [80] during bainitic transformation.

With an increase of cooling rate to 10°C/s, the intensity of the peak at 59° increases for all three steels compared to 3°C/s, but the increase is more pronounced in the higher carbon steel L06C06NbMo (Figure 5.21b). As the cooling rate increases to 30°C/s (Figure 5.21c) and then to 100°C/s (Figure 5.21d), the HAGB fraction continuously increases for all three steels, with the maximum increment in the higher carbon steel. The misorientation distribution for the lower

carbon steels, L04C08NbMo and L04C08NbMoCr, is very similar for all cooling rates investigated, suggesting there is almost no effect on the microstructure due to an increase in chromium content.

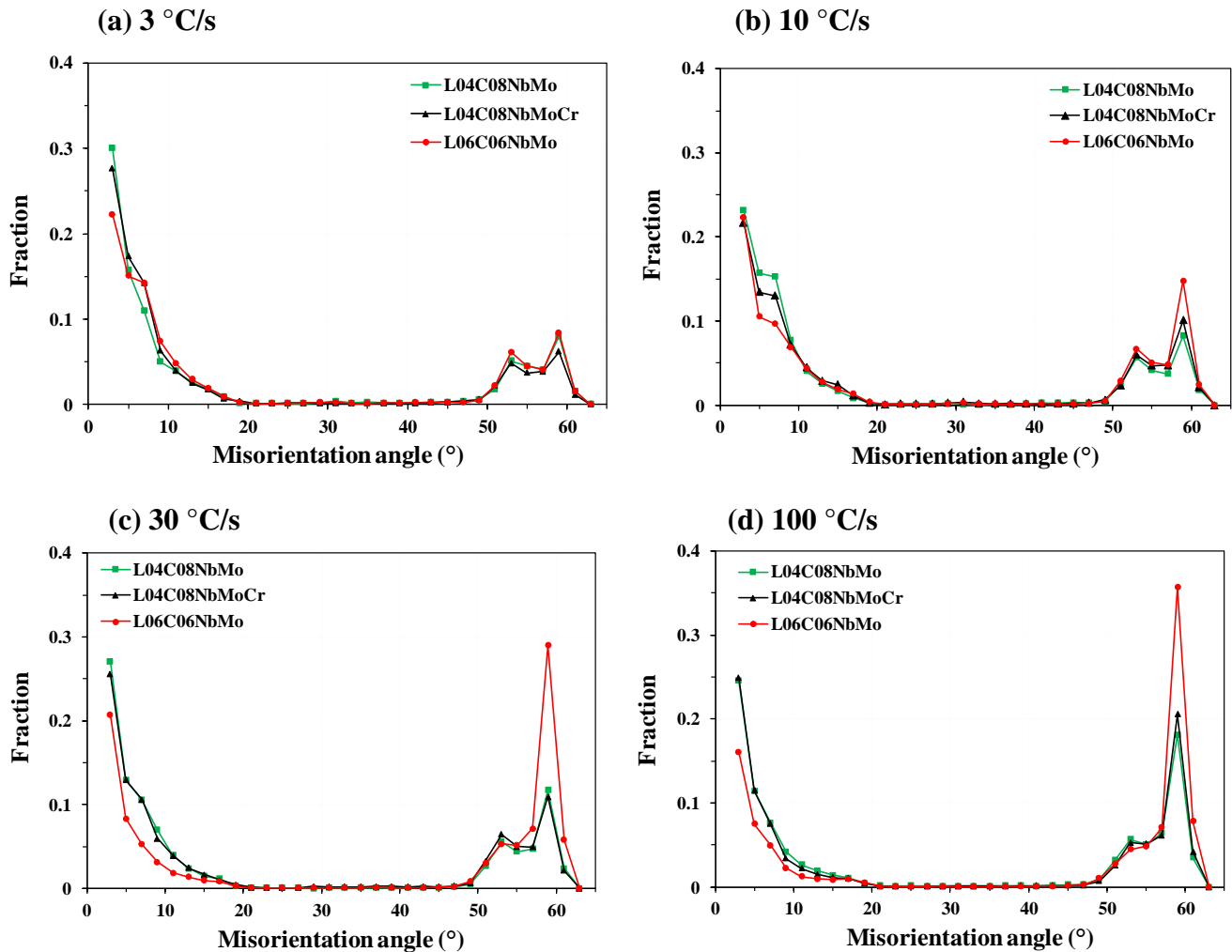


Figure 5.21: Distribution of misorientation angle for the three steel at different cooling rates (a) 3°C/s, (b) 10°C/s, (c) 30°C/s and (d) 100°C/s

Overall, Figure 5.21a-d shows that with an increase in cooling rate, there is an increase in HAGBs, leading to microstructure refinement for all steels studied, with the effect being most pronounced in L06C06NbMo. One way to quantitatively express the microstructure is by using high angle grain boundary density, which is defined as:

$$\text{HAGB density} = \frac{\text{HAGB line length}}{\text{Area of microstructure}} \quad (5.1)$$

HAGB density is plotted against cooling rate in Figure 5.22, and it is observed that this density increases with cooling rate for all steels. The density values are very similar for L04C08NbMo and L04C08NbMoCr, whereas for the higher carbon steel, L06C06NbMo, increase in cooling rate results in a more pronounced increase in the HAGB density. Each HAGB map was partitioned into four quadrants, and the standard deviation in HAGB density amongst the quadrants was calculated and reported as the error bar. The standard deviation in HAGB density represents the inhomogeneity in the microstructure.

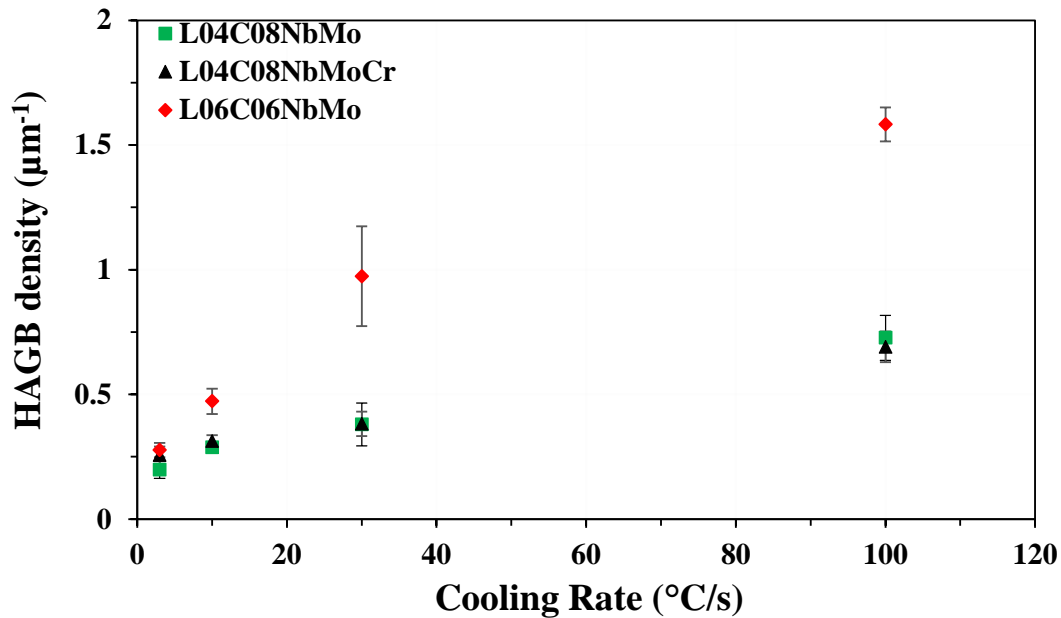


Figure 5.22: High angle grain boundary density in the product microstructure for the three steel at different cooling rates

The reciprocal of HAGB density, which represents an effective grain size or the refinement of the microstructure, was proposed by Mandal [10] as characteristic length scale, l , defined as:

$$\text{Characteristic length scale, } l = \frac{1}{\text{HAGB density}} \quad (5.2)$$

With an increase in the cooling rate it was observed that the transformation start temperature decreases, whereas the HAGB density increases. This prompted an attempt to develop a relation between the transformation start temperature and the HAGB density. A linear trend was found when the transformation start temperature, T_5 (5% transformed) is plotted against the square root of HAGB density, as shown in Figure 5.23. For the chemistries examined, the data suggests that the trend is maintained irrespective of chemistry. The following equation is obtained from the best linear fit, with R^2 value of 0.964.

$$\text{HAGB density}^{\frac{1}{2}} = 5.86 - (8.95 \times 10^{-3}) T_5 \quad (5.3)$$

where HAGB density is expressed in μm^{-1} and T_5 is in $^{\circ}\text{C}$.

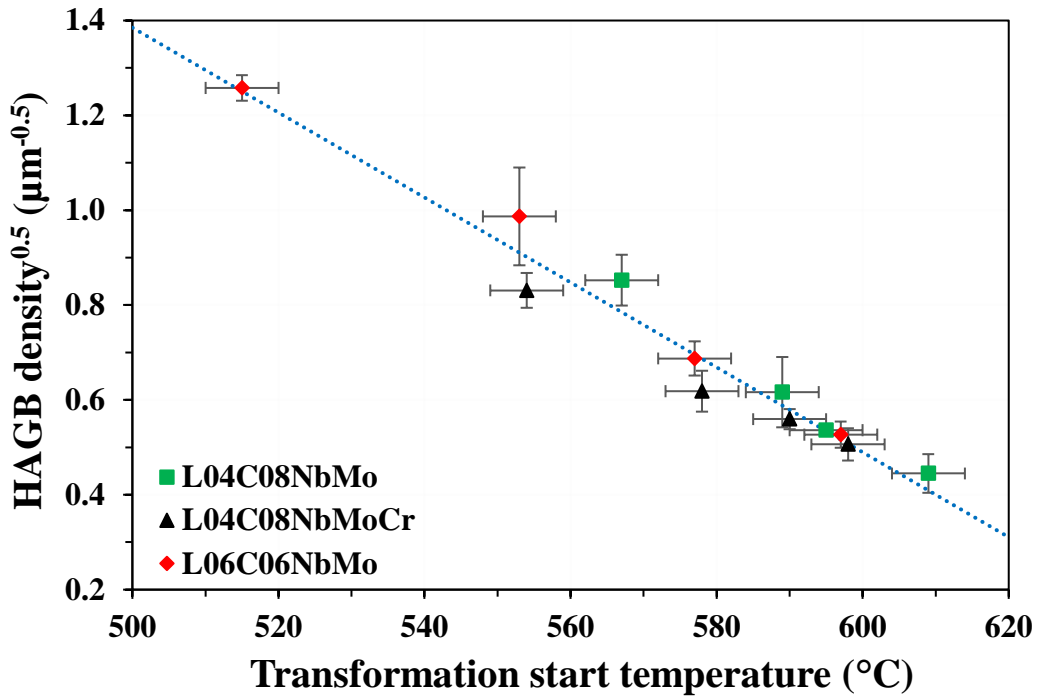


Figure 5.23: Relation between high angle grain boundary density and transformation start temperature

5.7 Hardness

Vickers hardness was measured for the decomposition products obtained under different cooling rates. Figure 5.24 shows that the hardness increases with an increase in cooling rate for all three steels. The two steels with lower carbon content, L04C08NbMo and L04C08NbMoCr, have very similar hardness, with the high chromium steel having marginally higher hardness of approximately 5 Hv for all cooling rates. L06C06NbMo, on the other hand, has similar hardness to the other two steels at 3 and 5°C/s, whereas for a higher cooling rate, the hardness measured is significantly higher compared to the other two steels. The increase in carbon content from 0.035wt% to 0.061wt% leads to an increase in hardness by about 10 Hv at 3°C/s cooling rate, whereas the increase in hardness jumps to approximately 50 Hv at 100°C/s cooling rate. The increase in cooling rate from 3°C/s to 100°C/s results in an increase in hardness by 57, 57 and 99 Hv for L04C08NbMo, L04C08NbMoCr and L06C06NbMo, respectively.

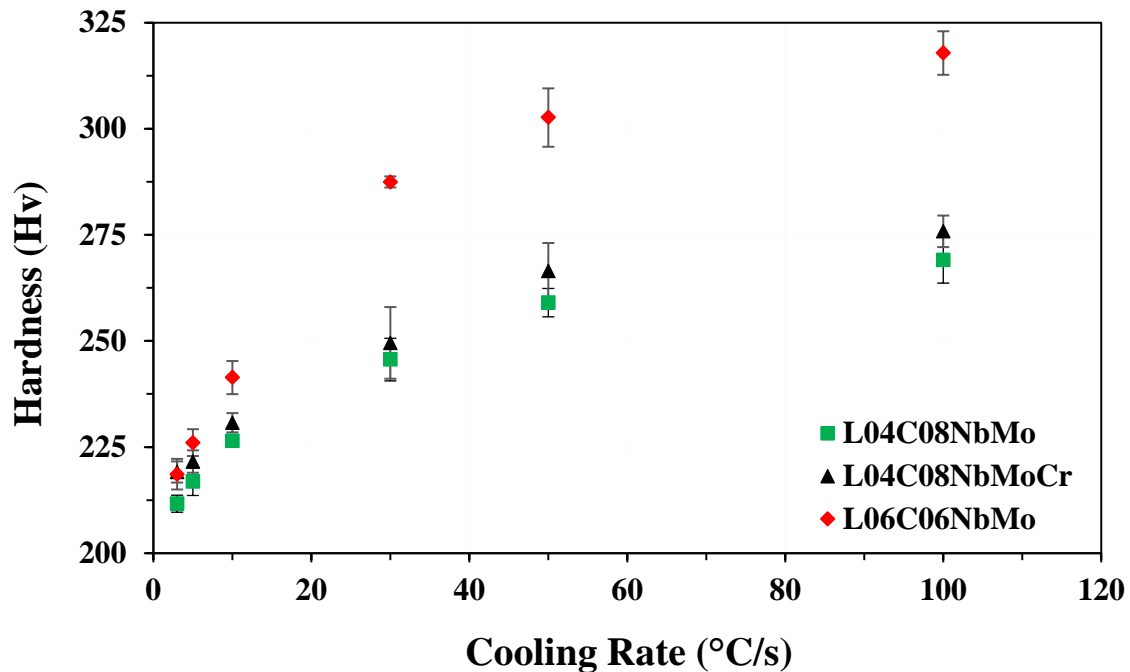


Figure 5.24: Vickers hardness of product microstructure for the three steel at different cooling rates

The error bar reported for hardness is the standard deviation calculated from 5 repeat hardness measurement for each condition. The value of hardness is reported in kgf/mm^2 . The trend in hardness with increase in cooling rate (Figure 5.24) closely follows the trend seen in HAGB density with cooling rate (Figure 5.22), and this is discussed in more detail in the following section.

5.8 Microstructure-property relationship

Figure 5.25 shows that the hardness for all the microstructures examined, irrespective of the steel, is related linearly to the square root of HAGB density as:

$$\text{Hardness (Hv)} = 156 + 133(\text{HAGB density})^{\frac{1}{2}} \quad (5.4)$$

The R^2 value for the fit is 0.963, indicating a very good fit. Equation 5.4 presents a relation that can be used to predict the hardness value for any intermediate microstructure.

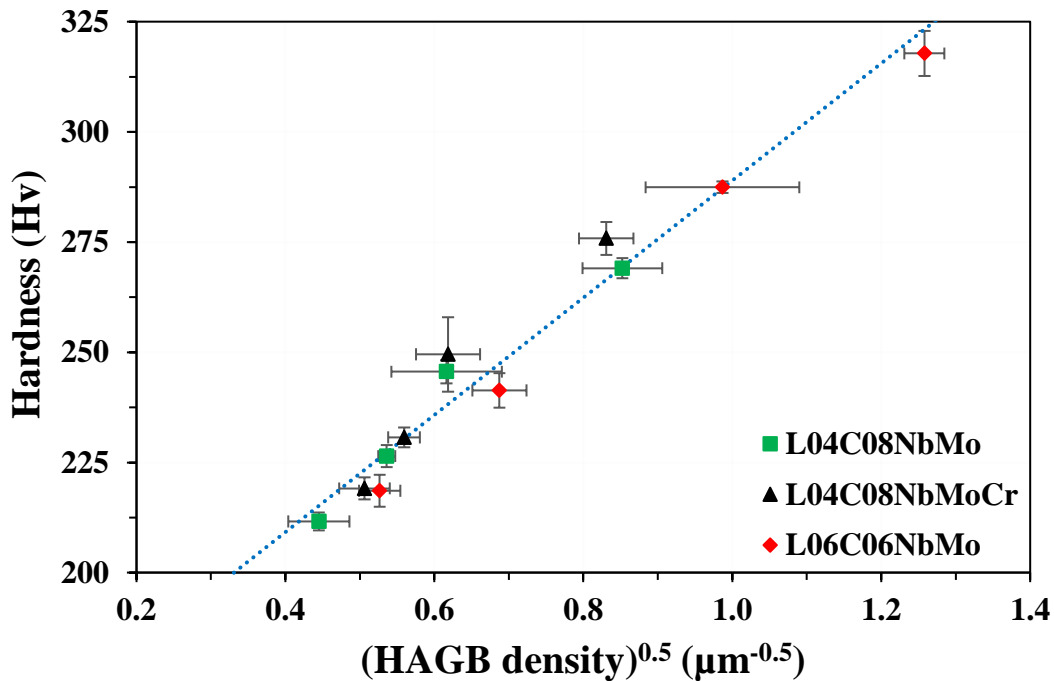


Figure 5.25: Hardness related to the high angle grain boundary density of different microstructures

In terms of characteristic length scale, l , expressed in μm , equation 5.4 can be rewritten as:

$$\mathbf{Hardness (Hv) = 156 + 133 \times l^{-0.5}} \quad \mathbf{(5.5)}$$

Equation 5.5 indicates a Hall-Petch like relation between the hardness and the characteristic length scale. From Figures 5.23 and 5.25, it can be seen that the microstructural feature, HAGB density, is related to the transformation start temperature as well as the material property i.e. hardness. Therefore, it is possible to find a relationship between the hardness and the transformation start temperature. Figure 5.26 shows hardness plotted against transformation start temperature for all eighteen conditions examined. It is worth noting that the previous relations and graphs presented in this section had twelve conditions, since EBSD analysis was carried out on those selected cases. Figure 5.26 indicates that over the complete set of eighteen conditions, irrespective of the chemistry, a linear trend with a R^2 value of 0.961 is maintained, indicating a good co-relation between the transformation start and hardness, given by the equation:

$$\mathbf{Hardness (Hv) = 962 - 1.23 \times T_5} \quad \mathbf{(5.6)}$$

The value of this relation is that the transformation start can be measured more easily than the HAGB density, thereby providing the ability to predict the property without the need to look into microstructure for a steel within the chemistry range studied.

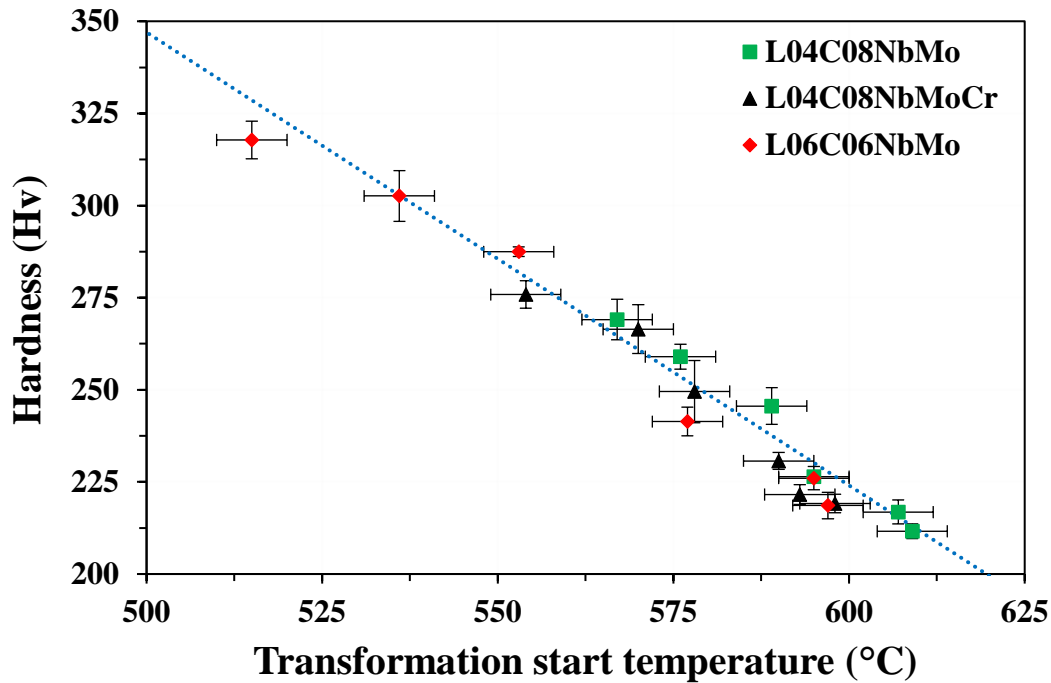


Figure 5.26: Relation between hardness and transformation start temperature

It was seen in this section that the transformation start temperature, microstructural feature (HAGB density) and material property (hardness) are related to each other for the range of chemistries studied. This would provide the potential to develop a predictive microstructure-property model if a chemistry-sensitive model were developed to predict the transformation start temperature as a function of cooling rate. In Chapter 6, such a model is developed and presented for the three steels investigated here.

5.9 Discussion

CCT tests showed that the increase in cooling rate results in a shift of the transformation curves to lower temperature. On increasing the cooling rate from 3°C/s to 100°C/s, there was a reduction in transformation start temperature by 42°C, 44°C and 82°C for L04C08NbMo, L04C08NbMoCr and L06C06NbMo, respectively. This is consistent with multiple studies which

show that faster cooling rate results in a shift of the transformation curve to lower temperature [10,40,58,59,98,113]. Since the decomposition of parent to daughter phase requires nucleation and growth, which are kinetic processes requiring time, an increase in cooling rate results in reduction of transformation temperature.

An increase in carbon from 0.035wt% to 0.061wt% resulted in a shift of the transformation curve to lower temperature. Figure 5.7 showed that the increase in carbon content lowers the transformation start temperature by 12 °C for 3 °C/s and 52 °C for 100°C/s, indicating that the effect due to increase in carbon content is amplified with increasing cooling rate. This is consistent with previous work by Robinson[59], where an increase in carbon from 0.028wt% to 0.058wt% resulted in approximately 20°C and 50°C reduction in transformation start temperature on increasing cooling rate from 10°C/s to 30°C/s with a prior austenite grain size of 35µm. Mandal[10] showed that increasing carbon content from 0.03wt% to 0.06wt% results in a depression in transformation start temperature by 18°C at 50°C/s cooling rate. This is lower than the observed reduction of 40°C in the present study for a similar change in carbon content, and the discrepancy may be due to significantly lower niobium content in the higher carbon steel compared to the lower carbon steel studied by Mandal. Table 5.3 shows the composition of the two steels studied by Mandal. In addition, the prior austenite grain size was different in Mandal's work, which might have a role to play in the observed difference. Carbon is a known austenite stabilizer, pushing the ferrite field to a lower temperature with increase in carbon content. Therefore, an increase in carbon results in reduction of the transformation temperature.

Table 5.3: Chemical composition in wt. % for the steels studied by Reichert [40] and Mandal [10]

Steel	C	Nb	Mo	Mn	Ni	Cu	Ti	N	Si	Al
I-06C03NbMo	0.06	0.035	0.24	1.65	0.42	0.13	0.012	0.005	0.11	0.027
I-03C09NbMo	0.03	0.091	0.29	1.70	0.13	0.25	0.017	0.008	0.31	0.041

An increase in chromium content from 0.023wt% to 0.24wt% resulted in a shift of transformation curves to a lower temperature. The transformation start temperature decreased by approximately 10°C irrespective of the cooling rate. Chen et. al. [114] studied the effect of chromium on austenite decomposition in CGHAZ and found that an addition of 0.269 wt% chromium resulted in a reduction of transformation start by about 5 to 15°C for cooling rates between 5°C/s and 60°C/s, which agrees with the present study. Beche et. al. [42] reported that chromium retards ferrite growth due to solute drag, which potentially explains the lowering of transformation temperature on increase of chromium content.

Figure 5.27 presents the CCT curves obtained for the austenite decomposition kinetics data and the hardness measurements for cases where cooling rates were maintained throughout transformation, i.e., up to 30°C/s. It is evident that the increase in cooling rate results in a decrease of transformation start and finish temperature for all three steels. Secondly, it can be seen that the shift in transformation to lower temperatures is consistently associated with an increase in the hardness. Finally, the effect of reduction in transformation temperature due to an increase of carbon and chromium can be seen in the CCT diagram. Reichert [40] presented a CCT diagram for a steel with similar chemistry as L06C06NbMo and same prior austenite grain size of 80µm, at cooling rates of 10°C/s and higher. Reichert’s data is added in the CCT curve in Figure 5.27 and the results in terms of transformation temperature, as well as hardness, agree closely with the L06C06NbMo

steel. The composition of the steel studied by Reichert (I-06C03NbMo) is shown in Table 5.3. CCT results presented by Chen [114] on the effect of chromium agree with the trend presented in the present study.

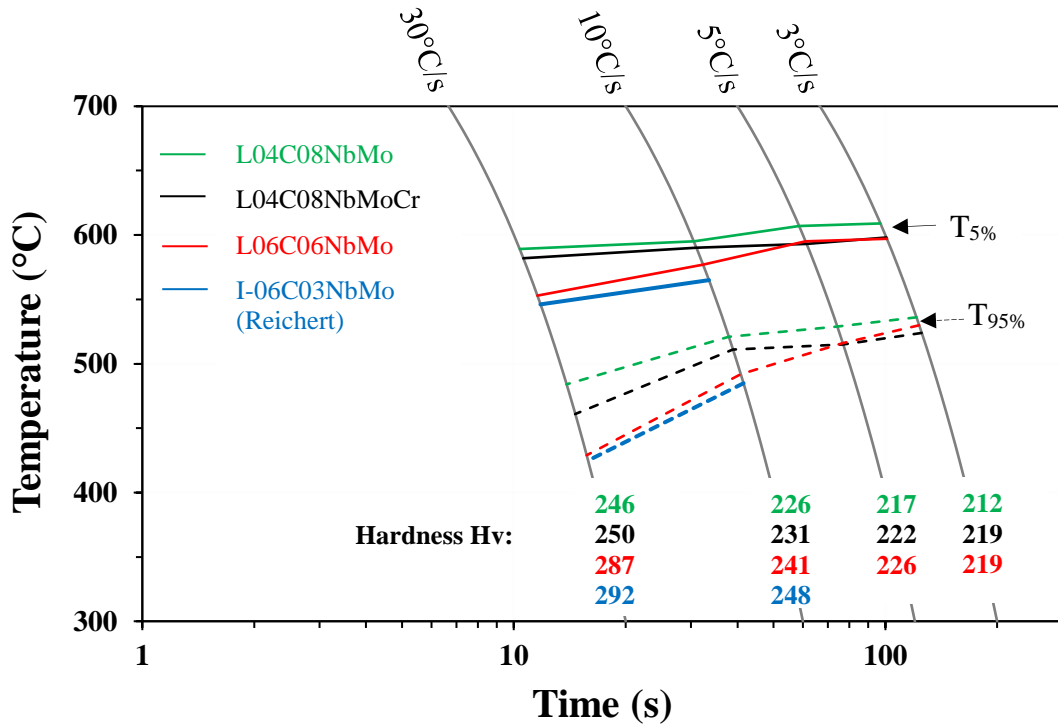


Figure 5.27: CCT diagram showing the transformation start (solid lines) and transformation finish (dashed lines) and hardness for the three steels. Data of previous work on a similar steel by Reichert [40] is included in blue

In the present work, all cases examined had the presence of all three Bain groups. However, the high temperature transformation products have coarse regions of a Bain group adjacent to the coarse regions of a different Bain groups, resulting in low HAGB density. As the transformation temperature decreases, different Bain groups are formed in close proximity to each other, resulting in fine lath-like regions, thereby increasing the HAGB density for lower transformation

temperatures. The rationale behind the variation in Bain group selection with the change in transformation temperature has been discussed in the literature review Section 2.3.3.1.

The EBSD method used in the present study to characterize the microstructure provides a way to quantify the microstructure and has been used in previous work by Mandal[10]. This method of microstructural analysis provides a way to quantitatively link the transformation kinetics to the microstructure, which in turn has been linked to the properties. In the present work, it is observed that with a decrease in the transformation start temperature, the HAGB density increases, independent of steel chemistry. In addition, the increase in HAGB density resulted in an increase in hardness. The inverse of HAGB density was defined by Mandal [10] as the characteristic length scale, and it was reported by the author that yield strength followed a Hall-Petch type-relationship with the characteristic length scale. Similarly, in the present study, comparison between hardness and characteristic length scale presents a Hall-Petch type-relation. Hodgson et. al [108] studied the change in tensile behavior with ferrite grain size in a low carbon steel. It was found that the yield stress increased from 250 MPa to 530 MPa as the grains were refined from approximately 5 μ m to 1 μ m. This highlight the significance of grain refinement on the strength of low carbon steel and the relevance of the Hall-Petch relationship for such steels.

A linear trend between transformation start temperature and hardness was found in the present work for all three steels studied. Data from previous work by Mandal[10] and Reichert[40] closely follow the trend for transformation start temperatures between 500 and 620°C, as shown in Figure 5.28. The trend starts to deviate for temperatures greater than 620°C, potentially due to the presence of ferrite, and at temperatures below 500°C, likely due to a saturation in refinement of the microstructure.

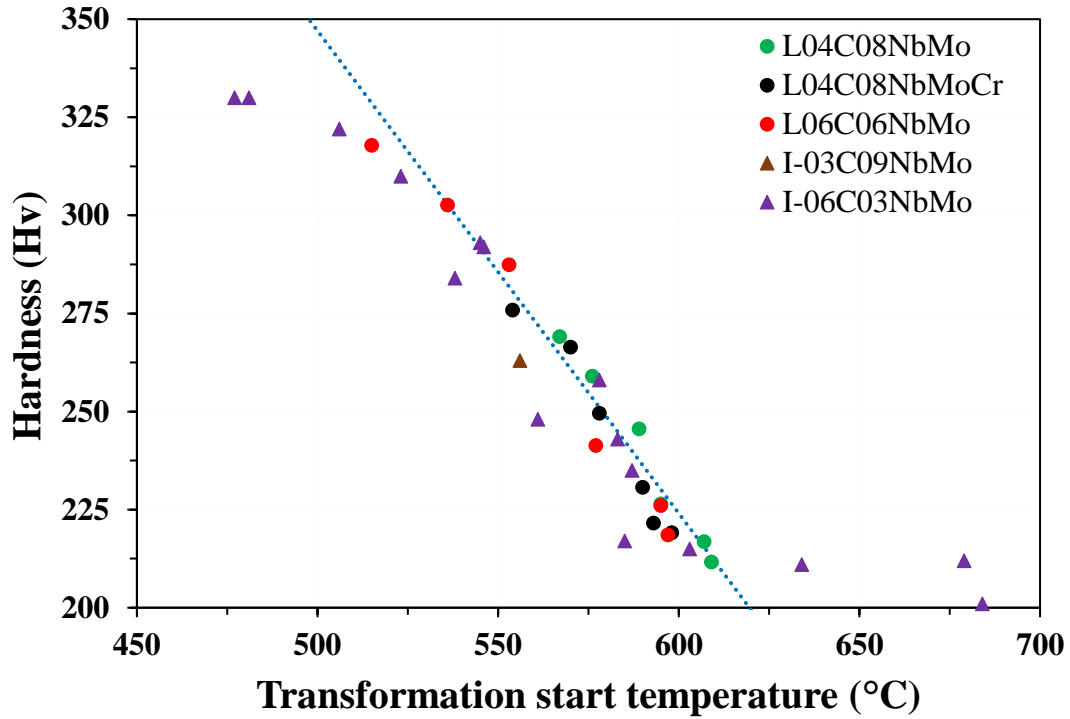


Figure 5.28: Comparison between present work (circular markers) and previous work by Mandal [10] and Reichert [40] (triangular marker) on relation between transformation start temperature and hardness

In summary, cooling rate and chemistry determine the transformation kinetics which in turn decide the variant and Bain group selection. This results in the misorientation angle distribution and microstructure refinement, which dictate the final hardness of the decomposed product. In the next chapter, a model is described to calculate the transformation start temperature for a given cooling rate and within the range of chemistries studied. This provides the critical link to calculate the microstructure and property (hardness) based on the Hall-Petch like-relation presented in this chapter.

Chapter 6: Modelling

6.1 Introduction

In the present work, it was found that all the decomposition products followed the K-S orientation relationship, indicating that the transformation product is bainite. Therefore, the model for austenite decomposition consists of two sub-models, i.e. (i) Bainite start temperature and (ii) Bainite growth kinetics.

Based on the bainite start temperature, the microstructure (HAGB density) and the property (hardness) can be calculated using equations 5.3 and 5.6, respectively. Thus, the emphasis of the model development is on the description of the bainite start.

6.2 Bainite start

Bhadeshia [78,116] proposed that the nucleation of bainite requires a driving pressure of 400 J/mol, which is the strain energy due to shear during bainite formation. Thermo-Calc database TCFE7 was used to calculate the temperature at which the critical driving pressure of 400 J/mol is obtained for the three steels studied. Based on this calculation, Table 6.1 provides the calculated bainite nucleation temperatures. It is observed that the nucleation temperature is practically the same, with very little difference between the chemistries studied.

Table 6.1: Bainite nucleation temperature (T_N) based on driving pressure of 400 J/mol

Steel	Bainite nucleation temperature
L04C08NbMo	649 °C
L04C08NbMoCr	646 °C
L06C06NbMo	644 °C

The bainite start temperature is modelled based on the approach used by Reichert [40] and Garcin[96]. It is worth noting that the niobium is lower in L06C06NbMo steel compared to the other two steels. Isasti [110] reported that the increase in niobium from 0.03wt% to 0.06wt%

resulted in a very small variation on austenite decomposition kinetics. Therefore, further increase in niobium might have a very small effect on austenite decomposition, if any. Due to this, the effect on decomposition kinetics due to the variation in niobium in investigated steels is neglected during modelling. The bainite start temperature (T_5) is calculated by solving the following equation:

$$0.05 = \int_{T_5}^{T_N} \left[\frac{\alpha_1 + \alpha_2 T}{\phi} \right] dT \quad (6.1)$$

where, ϕ is the cooling rate in $^{\circ}\text{C}/\text{s}$, T_N is the bainite nucleation temperature, 0.05 represent 5% transformation and α_1, α_2 are chemistry dependent fit parameters. Table 6.2 shows the values of the fit parameter for the three steels obtained by minimizing RMS error.

Table 6.2: Fit parameter to calculate the bainite start temperature

Steel	$\alpha_1(\text{s}^{-1})$	$\alpha_2(^{\circ}\text{C}^{-1}\text{s}^{-1})$
L04C08NbMo	1.63	-2.59×10^{-3}
L04C08NbMoCr	1.63	-2.62×10^{-3}
L06C06NbMo	0.50	-8.00×10^{-4}

Figure 6.1 compares the experimental data with the model calculations for the three steels studied, showing that the proposed model describes the experimental data within the error of measurement. The change of chromium content resulted in a shift of the transformation start temperature by about 10°C irrespective of the cooling rate, and the effect was captured by changing only the α_2 parameter. The effect of carbon was confounded by cooling rate, thereby requiring a change in both α_1 and α_2 . If the effect of carbon and chromium content is assumed to linearly change between the range of chemistry examined, the fit parameters α_1 and α_2 can be expressed as a function of chemistry according to the following equations, where X_C and X_{Cr} represent weight % of carbon and chromium, respectively:

$$\alpha_1 = 3.15 - 43.4X_c \quad (6.2)$$

$$\alpha_2 = (6.85 \times 10^{-2})X_c - (1.43 \times 10^{-4})X_{Cr} - (4.98 \times 10^{-3}) \quad (6.3)$$

It was found that the calculated transformation start temperatures lie within $\pm 6^\circ\text{C}$ of the experimentally measured values for all eighteen cases studied. This is comparable with the experimental measurement error of $\pm 5^\circ\text{C}$, indicating sufficient accuracy of the presented model.

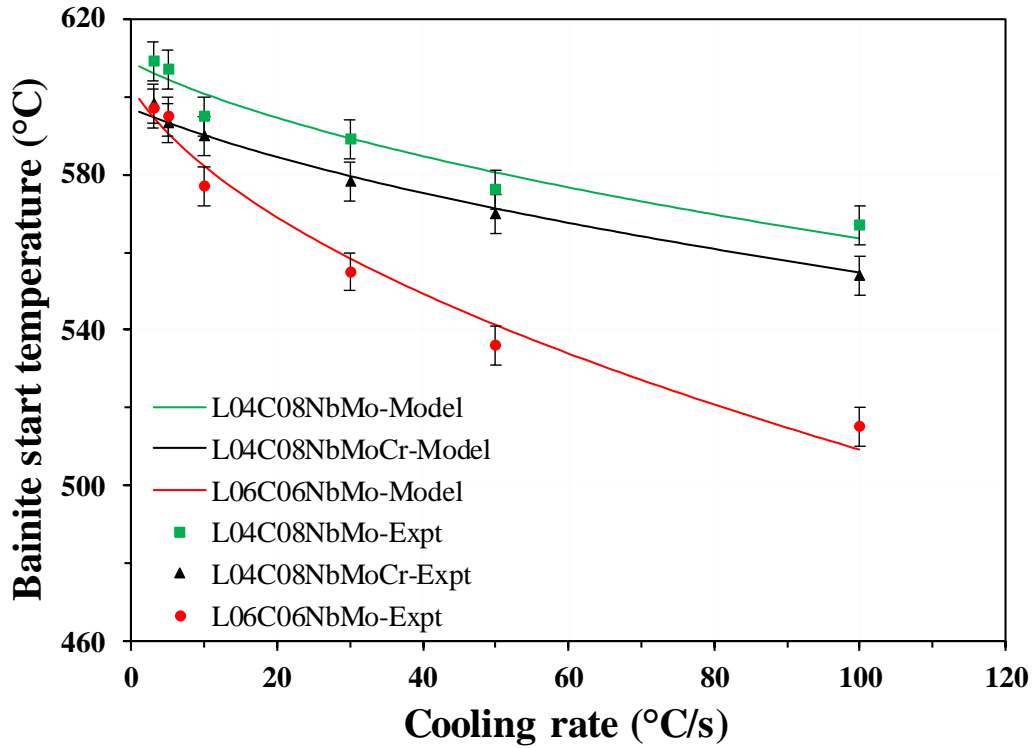


Figure 6.1: Model prediction and experimentally measured bainite start temperature for the three steels

6.3 Bainite growth

Bainite start is followed by bainite growth which is described by using the JMAK model in combination with the additivity rule, i.e.:

$$f = 1 - \exp\left(-\int_T^{T_s} \frac{\beta^n}{\phi} dT\right)^n \quad (6.4)$$

In equation 6.4, f represents the fraction transformed at any temperature T . The CCT data of the present study was best described with a JMAK exponent of $n = 0.9$ for all three steels. The rate parameter, β was taken as a temperature-dependent function as follows:

$$\beta = \exp(\beta_1 + \beta_2 T) \quad (6.5)$$

where β_1 and β_2 are fit parameters that depend on steel chemistry. Table 6.3 presents the values of the fit parameters obtained for each steel. Note that both the lower carbon steels, L04C08NbMo and L04C08NbMoCr, can be modelled using the same fit parameter with relatively good accuracy since the effect of chromium content on suppressing the transformation temperature by approximately 10°C is captured in the bainite start model, effectively reducing the total number of fit parameters.

Table 6.3: Fit parameter to calculate austenite decomposition kinetics

Steel	β_1	$\beta_2(^{\circ}\text{C}^{-1})$
L04C08NbMo	25.8	-4.82×10^{-2}
L04C08NbMoCr	25.8	-4.82×10^{-2}
L06C06NbMo	12.0	-2.48×10^{-2}

The fit parameters β_1 and β_2 are assumed as a linear function of carbon content, since only two levels of carbon are included in the present study. The fit parameters can be expressed in terms of chemistry, where X_C is the weight % of carbon content in the steel, according to the following equations:

$$\beta_1 = 44.35 - 530X_C \quad (6.6)$$

$$\beta_2 = (9 \times 10^{-1})X_C - (8 \times 10^{-2}) \quad (6.7)$$

The fit parameters were calculated using only those conditions in which cooling rate was maintained throughout the transformation, i.e., cases up to 30°C/s cooling rate. Growth of the cases

up to 30°C/s cooling rate were modelled using the constant, temperature-independent cooling rate (ϕ) value in equation 6.4.

Other cases, where the cooling rate was not maintained during transformation, i.e., for nominal cooling rates of 50 and 100°C/s, the cooling rate was treated as a temperature-dependent variable. The differential form of the JMAK with additivity, presented previously in equation 2.3, was used to take into account the varying cooling rates. The growth model begins with an initial fraction transformed, f as 0.05, since the transformation start temperature is considered at 5% transformation. Since the time-temperature profile for any case is experimentally known, the value of temperature dependent β can be calculated for any specific time. Small time step, dt , is taken and the value of temperature dependent β at that instant is calculated using equation 6.5. Sensitivity analysis is done to ascertain that a sufficiently small time step is used. The increment in fraction transformed (df) is calculated using equation 2.3 and the value is added to the previous fraction to obtain the new fraction transformed, using:

$$f_{i+1} = f_i + df \quad (6.8)$$

This iterative process using equations 2.3 and 6.8 is repeated to obtain the complete growth curve in the case of non-uniform cooling.

Figures 6.2 and 6.3 compare the experimentally measured transformation kinetics with model calculations for select cases of L04C08NbMo and L06C06NbMo, respectively. It is observed that the model matches the experimental result very closely during the majority of the transformation, with more than 10°C disagreement occurring only during the final stages of transformation (greater than 80% transformed) in some cases. Modelled growth kinetics for the rest of the cases for these two steels and all cases for L04C04NbMoCr were also in close agreement with the experimental results.

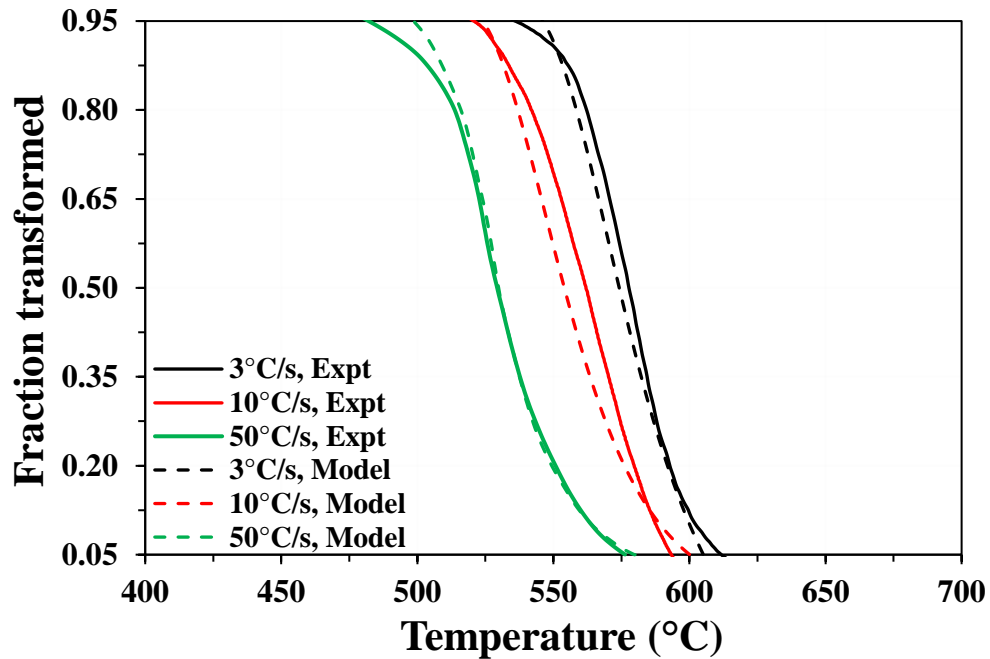


Figure 6.2: Comparison between experimentally measured transformation kinetics and model prediction for L04C08NbMo

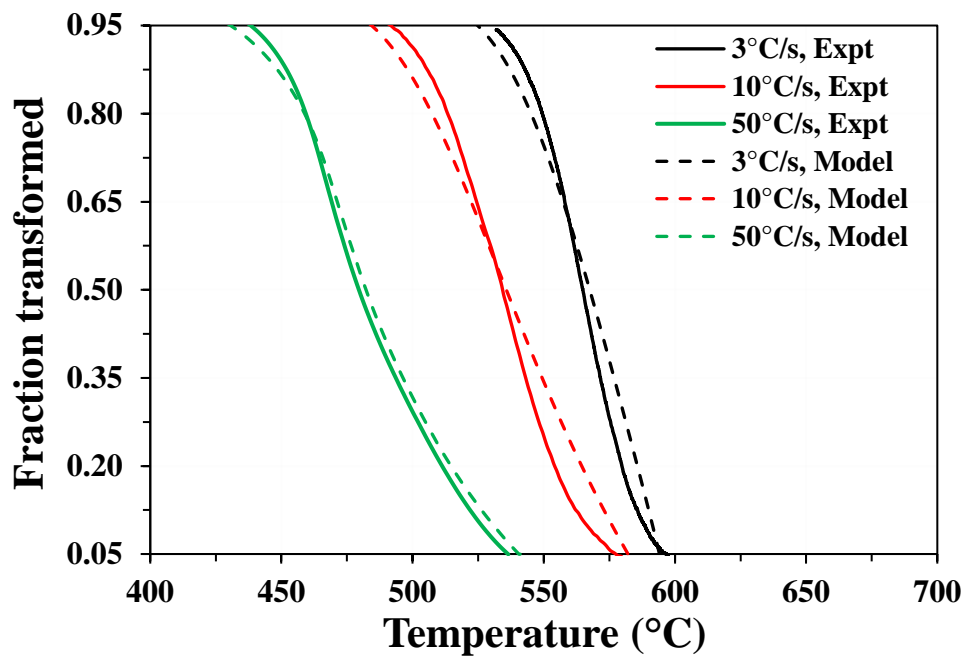


Figure 6.3: Comparison between experimentally measured transformation kinetics and model prediction for L06C06NbMo

Figure 6.4 shows the measured and calculated temperatures for 25%, 50% and 75% transformation for all three steels under all six cooling rates investigated. The dashed lines show $\pm 5^\circ\text{C}$ deviation, which is equal to experimental measurement error. It is observed that the deviation of the calculated temperature from the experimental measurement lies within or very close to the experimental error of $\pm 5^\circ\text{C}$ for all three steels, indicating sufficient accuracy of the growth model.

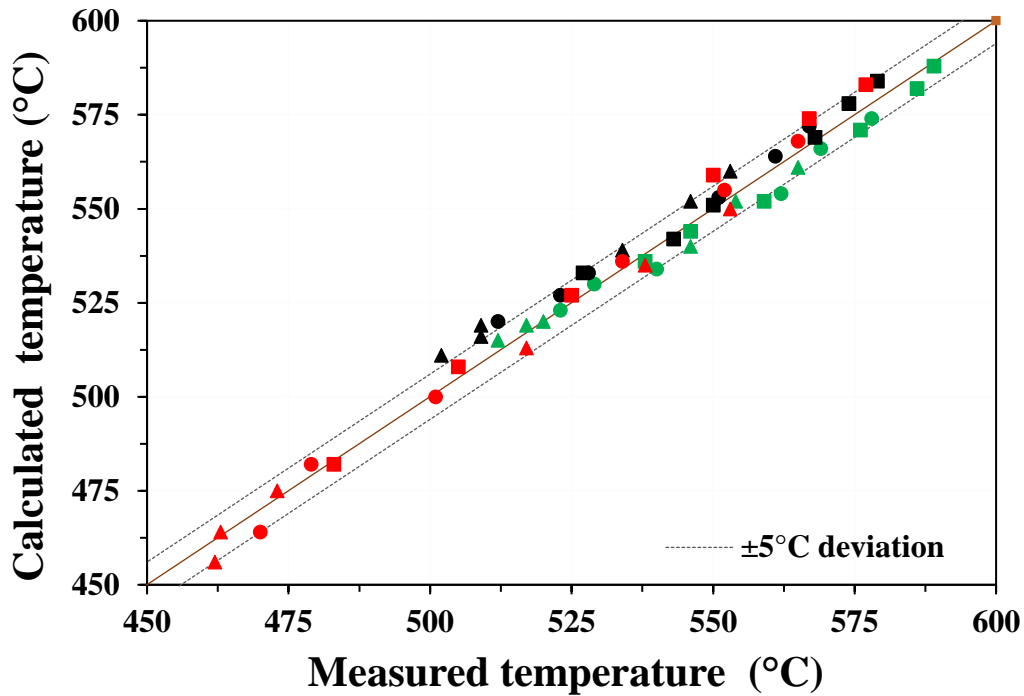


Figure 6.4: Comparison between calculated and experimentally measured 25% (square marker), 50% (circular marker) and 75% (triangular marker) transformation temperature for all three steels. L04C08NbMo, L04C08NbMoCr and L06C06NbMo shown in green, black and red, respectively

6.4 Structure and property calculation

The relationship between experimentally measured transformation start temperature, high angle grain boundary density and hardness was discussed in Sections 5.6 and 5.8. In this chapter,

Equation 5.6 provides a linear relation between the transformation start temperature and hardness. Here, the hardness values are calculated by using the transformation start temperatures as obtained with the model. Figure 6.6 presents the comparison between these calculated values of hardness against the experimentally measured values, showing good agreement within a 5% scatter band. The maximum standard deviation in experimental measurements of hardness was about 10 Hv (4% experimental error), which is comparable to the deviation between experimental and calculated values of hardness for most cases.

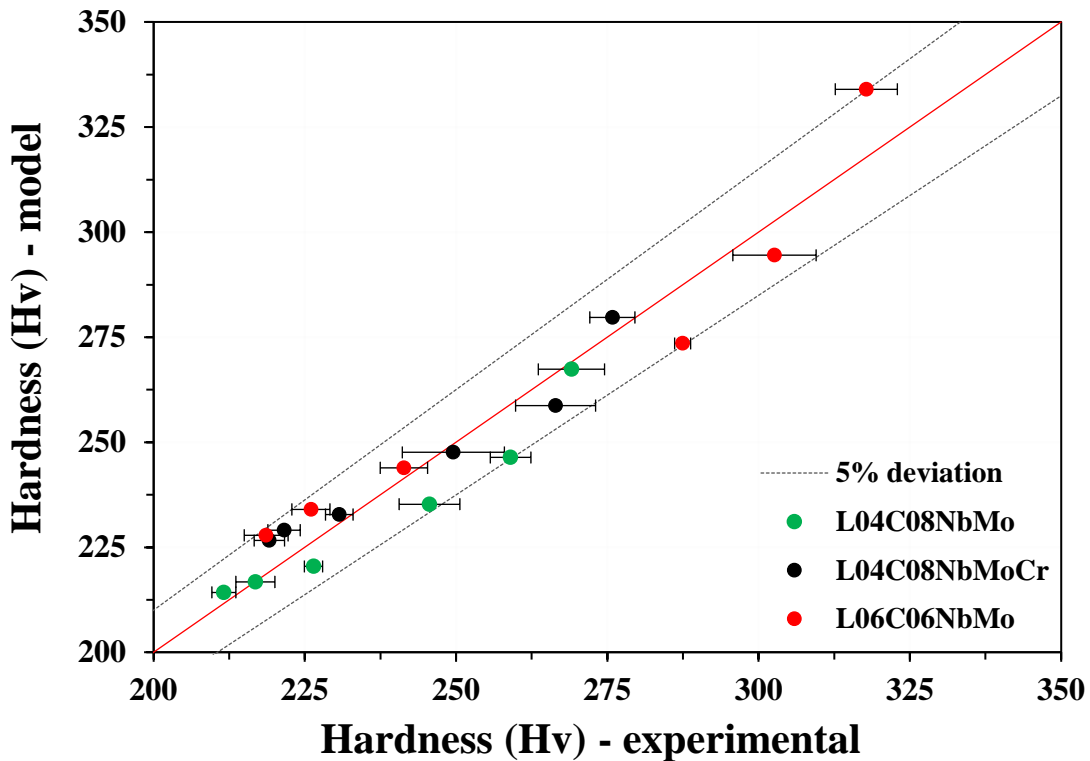


Figure 6.6: Comparison between experimental result and model calculation for hardness (dashed lines shows 5% scatter band)

6.5 Discussion

The present work captures the effect of carbon content, chromium content and cooling rate on austenite decomposition kinetics for an austenite grain size representative for the CGHAZ. The transformation start temperatures were modelled within $\pm 6^\circ\text{C}$ of experimentally measured values. In comparison, Reichert [40] looked into the effect of niobium content in solution, prior austenite grain size, cooling rate and reported that the majority of calculated transformation start temperature were within $\pm 15^\circ\text{C}$ of experimentally measured values.

It was evaluated that a JMAK exponent value of 0.9 resulted in a good description of the growth kinetics for all three steels studied in the present work. This value is very close to the values of 0.9 reported by Militzer et al. [92] for several HSLA steels and 1.1 reported by Reichert [40] for an X80 steel. Reichert reported the accuracy of the growth model by comparing the calculated 50% transformation temperature to be within $\pm 5^\circ\text{C}$ of the experimental value, for the majority of cases, which is similar to the accuracy obtained in the present work.

Fit parameters for the bainite growth model in the present work were calculated based on cases in which the cooling rates were maintained during the transformation, i.e. for cooling rates up to 30°C/s . These fit parameters were then used to model growth in non-uniform cooling rate cases, and the model calculations were in very good agreement with the experimental decomposition kinetics. This acts as a validation for the growth model. It was observed that the final stages of growth resulted in discrepancy greater than 10°C between the model and the experimental results for some cases. This could potentially be reduced by introducing additional fit parameters, but that would not add much value to the model, since the microstructure and hardness are calculated using the transformation start temperature.

Using the proposed transformation start model, in combination with the empirical relationship between transformation start temperature and hardness, the calculated hardness was found to be within 5% of experimental measurements for all cases. This is comparable to the experimental standard deviation of 4%, suggesting a good agreement between the experimental and modelled results. Several other studies in the literature have also modelled the hardness of the austenite decomposition products in low-carbon microalloyed steel. In one such study, Azghandi et al. [97] looked into the austenite decomposition of vanadium microalloyed steel. The resultant microstructure was multi-phase, which is in contrast to the single-phase bainitic microstructure obtained in the present study. The calculated hardness was reported within 11% of experimentally measured hardness. In this model, the calculation of hardness was based on the calculated phase fraction in combination with empirical formulae of hardness for each phase. In another study, Maetz et. al [117] modelled the precipitation hardening during the coiling of four different Nb-Mo steels. This model accounted for precipitation hardening of the microstructure and the softening of the microstructure due to tempering. The hardness predictions were found to be within 5% of the experimentally measured hardness for all the steels.

The current work offers a novel approach to calculate hardness using modelled transformation start temperature based on the chemistry and the cooling rate. This approach can potentially be expanded over a broader chemistry range to build a robust, chemistry-dependent model.

Chapter 7: Summary and Future work

7.1 Summary

The objective of the current work was to study austenite decomposition in X80 line pipe steels with a focus on quantifying the effect of carbon and chromium content at different cooling rates on the microstructure and hardness of the coarse grain heat affected zone. Bulk samples were subjected to thermal cycles designed to replicate CGHAZ conditions. Austenite decomposition kinetics were recorded using a contact dilatometer. Detailed microstructure characterization was carried out using optical microscopy and electron backscattered diffraction mapping. Hardness measurements were carried out using a micro-Vickers indenter. Chapter 5 presented the experimental results in details. A model was presented in Chapter 6 to calculate the transformation kinetics, microstructure and hardness. The important results found in this work are summarized below.

1. An increase in carbon content from 0.035 wt% to 0.061 wt% resulted in a reduction in transformation start temperature by approximately 10°C at 3°C/s to 50°C at 100°C/s cooling rate.
2. Increase in chromium content from a residual amount to 0.24 wt% suppresses the transformation temperature modestly by about 10°C for all cooling rates.
3. The hardness for both lower carbon steels, L04C08NbMo and L04C08NbMoCr, increases approximately 60 Hv on increasing the cooling rate from 3°C/s to 100°C/s, whereas for the higher carbon steel, L06C06NbMo, the increase is about 100 Hv.
4. The high angle grain boundary density increases with an increase in cooling rate for all three steels. The two lower carbon steels have similar microstructure at any specific cooling rate, with the HAGB density increasing from about 0.25 μm^{-1} to 0.7 μm^{-1} on increasing the

cooling rate from 3°C/s to 100°C/s for both steels. The higher carbon steel has a microstructure similar to the lower carbon steels at a slower cooling rate of 3°C/s with HAGB density of about 0.28 μm^{-1} , but the microstructure becomes much more refined at faster cooling rates. The HAGB density is approximately 1.6 μm^{-1} for the higher carbon steel at 100°C/s.

5. A linear relationship between transformation start temperature and square root of HAGB density was observed within the chemistry range studied.
6. The inverse of HAGB density was defined as an effective grain size or a characteristic length scale. A Hall-Petch like-effect is observed between the hardness and the effective grain size.
7. A chemistry-sensitive transformation start model has been proposed with accuracy within $\pm 6^\circ\text{C}$ of experimental data, which is very good considering the standard deviation for experimentally measured transformation start was 5°C . A growth model based on JMAK with additivity captured the bainite growth kinetics within $\pm 10^\circ\text{C}$ for the majority of cases.
8. The transformation start model was combined with the empirical relationships between transformation start temperature, HAGB density and hardness to compute microstructure and hardness. Hardness was calculated within 5% of the experimentally measured value, which is comparable to the experimental measurement error of 4%.

7.2 Future work

The present work looked into the effect of carbon and chromium content on austenite decomposition in the CGHAZ and established relationships between decomposition kinetics, microstructure and hardness. Future work could expand these relationships over a broader range

of chemistries and include other mechanical properties. With the aim to develop a robust chemistry dependent model, some suggestions for future work in the field are given below:

1. A systematic study should be conducted to quantify the effect of other alloying elements, mainly molybdenum and niobium on austenite decomposition kinetics. In addition, studying more steels will also reveal interaction between alloying elements, if any.
2. Additional work needs to be done to examine mechanical properties like tensile behavior, impact toughness and ductile to brittle transition temperature. It will be critical to link them to transformation kinetics and microstructure.
3. Based on austenite decomposition and property studies over a larger chemistry range, a chemistry-dependent model can be built capable of predicting the microstructure and properties in the CGHAZ of line pipe grades.

Bibliography

- [1] The oil and gas industry in energy transitions (2020). <https://www.iea.org/reports/the-oil-and-gas-industry-in-energy-transitions>
- [2] World energy outlook (2019). <https://www.iea.org/reports/world-energy-outlook-2019>
- [3] Energy and the economy (2020). <https://www.nrcan.gc.ca/science-data/data-analysis/energy-data-analysis/energy-facts/energy-and-economy/20062>
- [4] Oil and Natural gas pipelines (2020). <https://www.capp.ca/explore/oil-and-natural-gas-pipelines/>
- [5] C. Shang, F. Guo, The state of the art of long distance gas pipeline in China, International Gas Research Conference Proceedings. 2 (2017) 723–729.
- [6] C. Li, Y. Wang, T. Han, B. Han, L. Li, Microstructure and toughness of coarse grain heat-affected zone of domestic X70 pipeline steel during in-service welding, Journal of Materials Science. 46 (2011) 727–733.
- [7] X.L. Wang, Z.Q. Wang, L.L. Dong, C.J. Shang, X.P. Ma, S.V. Subramanian, New insights into the mechanism of cooling rate on the impact toughness of coarse grained heat affected zone from the aspect of variant selection, Materials Science and Engineering A. 704 (2017) 448–458.
- [8] X.L. Wang, Z.Q. Wang, X.P. Ma, S.V. Subramanian, Z.J. Xie, C.J. Shang, X.C. Li, Analysis of impact toughness scatter in simulated coarse-grained HAZ of E550 grade offshore engineering steel from the aspect of crystallographic structure, Materials Characterization. 140 (2018) 312–319.
- [9] Y.Q. Zhang, H.Q. Zhang, J.F. Li, W.M. Liu, Effect of heat input on microstructure and toughness of coarse grain heat affected zone in Nb microalloyed HSLA steels, Journal of Iron and Steel Research International. 16 (2009) 73–80.

- [10] M. Mandal, Microstructure and mechanical properties of simulated weld heat affected zones in X80 linepipe steel, PhD Thesis, The University of British Columbia, Vancouver (2020)
- [11] S. Vervynckt, K. Verbeken, B. Lopez, J.J. Jonas, Modern HSLA steels and role of non-recrystallisation temperature, *International Materials Reviews*. 57 (2012) 187–207.
- [12] T.N. Baker, Microalloyed steels, *Ironmaking and Steelmaking*. 43 (2016) 264–307.
- [13] J.G. Lenard, *Primer on Flat Rolling: Second Edition*, Elsevier Ltd., Oxford (2014).
- [14] J.M. Gray, Niobium bearing steels in pipeline projects, *Niobium, Science and Technology*. (2001) 889–906.
- [15] H. Pingz, B.S. District, S. Hai, S. Co, B.S. District, S. Hai, Research and development of Ultra-high strength X100 welded pipe, (2014) 613–614.
- [16] L.E. Collins, R. Klein, D. Bai, Development of high strength line pipe for arctic applications, *Canadian Metallurgical Quarterly*. 48 (2009) 261–270.
- [17] J.C. Villalobos, A. Del-Pozo, B. Campillo, J. Mayen, S. Serna, Microalloyed steels through history until 2018: Review of chemical composition, processing and hydrogen service, *Metals*. 8 (2018) 351.
- [18] J.Q. Wang, A. Atrens, D.R. Cousens, N. Kinaev, Microstructure of X52 and X65 pipeline steels, *Journal of Materials Science*. 34 (1999) 1721–1728.
- [19] D. Belato Rosado, W. de Waele, D. Vanderschueren, S. Hertelé, Latest developments in mechanical properties and metallurgical features of high strength line pipe steels, *International Journal Sustainable Construction & Design*. 4 (2013) 1.
- [20] D.H. Seo, C.M. Kim, J.Y. Yoo, K.B. Kang, Microstructure and mechanical properties of X80/X100 grade plates and pipes, *Proceedings of the International Offshore and Polar Engineering Conference*. (2007) 3301–3306.
- [21] J.Y. Yoo, S.S. Ahn, D.H. Seo, W.H. Song, K.B. Kang, New development of high grade X80 to X120 pipeline steels, *Materials and Manufacturing Processes*. 26 (2011) 154–160.

- [22] J.M. Zhang, W.H. Sun, H. Sun, Mechanical properties and microstructure of X120 grade high strength pipeline steel, *Journal of Iron and Steel Research International*. 17 (2010) 63–67.
- [23] J.Y. Koo, M.J. Luton, N.V. Bangaru, R.A. Petkovic, D.P. Fairchild, C.W. Petersen, H. Asahi, T. Hara, Y. Terada, M. Sugiyama, H. Tamehiro, Y. Komizo, S. Okaguchi, M. Hamada, A. Yamamoto, I. Takeuchi, Metallurgical design of ultra high-strength steels for gas pipelines, *International Journal of Offshore and Polar Engineering*. 14 (2004) 2–10.
- [24] H. Makino, T. Amano, Demonstration of Crack Arrestability of X100 Line Pipe and Development of Evaluation Technologies for Three-dimensional Fracture Process, *Nippon steel & Sumitomo metal technical report*. 107 (2015) 38–43.
- [25] X. Wu, Strain-aging behavior of X100 line-pipe steel for a long-term pipeline service condition, M.A.Sc. Thesis, University of Calgary, Calgary (2010).
- [26] S. Nafisi, M.A. Arafin, L. Collins, J. Szpunar, Texture and mechanical properties of API X100 steel manufactured under various thermomechanical cycles, *Materials Science and Engineering A*. 531 (2012) 2–11.
- [27] T. Gladman, *The Physical Metallurgy of Microalloyed Steels*, Maney for the Institute of Materials, London (1997).
- [28] C. Stallybrass, H. Meuser, F. Gerdemann, C. Kalwa, H.G. Hillenbrand, High strength large diameter UOE line pipes optimised for application in remote areas and low-temperature service, *Pipeline Technology Conference, Hannover, Germany* (2013) 368.
- [29] Y. Ito and K. Bessyo, Cracking Parameter to heat of affected High Strength zone cracking Steels related, *Journal of Japan Welding Society*. 37 (1968) 983-991.
- [30] J.W. Cahn, The impurity-drag effect in grain boundary motion, *Acta Metallurgica*. 10 (1962) 789–798.
- [31] K. Nishioka, K. Ichikawa, Progress in thermomechanical control of steel plates and their commercialization, *Science and Technology of Advanced Materials*. 13 (2012) 3.

- [32] A.J. Craven, K. He, L.A.J. Garvie, T.N. Baker, Complex heterogeneous precipitation in titanium-niobium microalloyed Al-killed HSLA steels - II. Non-titanium based particles, *Acta Materialia*. 48 (2000) 3869–3878.
- [33] P. Gong, E.J. Palmiere, W.M. Rainforth, Dissolution and precipitation behaviour in steels microalloyed with niobium during thermomechanical processing, *Acta Materialia*. 97 (2015) 392–403.
- [34] J. Moon, J. Lee, C. Lee, Prediction for the austenite grain size in the presence of growing particles in the weld HAZ of Ti-microalloyed steel, *Materials Science and Engineering A*. 459 (2007) 40–46.
- [35] K. Banerjee, M. Militzer, M. Perez, X. Wang, Nonisothermal austenite grain growth kinetics in a microalloyed X80 linepipe steel, *Metallurgical and Materials Transactions A: Physical Metallurgy and Materials Science*. 41 (2010) 3161–3172.
- [36] W. Yan, Y.Y. Shan, K. Yang, Influence of TiN inclusions on the cleavage fracture behavior of low-carbon microalloyed steels, *Metallurgical and Materials Transactions A: Physical Metallurgy and Materials Science*. 38 (2007) 1211–1222.
- [37] R. Lagneborg, T. Siwecki, S. Zajac, B. Hutchinson, Role of vanadium in microalloyed steels, *Scandinavian Journal of Metallurgy*. 28 (1999) 186–241.
- [38] T.N. Baker, Processes, microstructure and properties of vanadium microalloyed steels, *Materials Science and Technology*. 25 (2009) 1083–1107.
- [39] P. Cizek, B.P. Wynne, C.H.J. Davies, B.C. Muddle, P.D. Hodgson, Effect of composition and austenite deformation on the transformation characteristics of low-carbon and ultralow-carbon microalloyed steels, *Metallurgical and Materials Transactions A: Physical Metallurgy and Materials Science*. 33 (2002) 1331–1349.
- [40] J.M. Reichert, Structure and properties of complex transformation products in Nb/Mo-microalloyed steels, PhD thesis, The University of British Columbia, Vancouver (2016).

- [41] W.B. Lee, S.G. Hong, C.G. Park, K.H. Kim, S.H. Park, Influence of Mo on precipitation hardening in hot rolled HSLA steels containing Nb, *Scripta Materialia*. 43 (2000) 319–324.
- [42] A. Béché, H.S. Zurob, C.R. Hutchinson, Quantifying the solute drag effect of Cr on ferrite growth using controlled decarburization experiments, *Metallurgical and Materials Transactions A: Physical Metallurgy and Materials Science*. 38 A (2007) 2950–2955.
- [43] T. Imao, S. Hiroshi, T. Tomo, O. Chiaki, *Thermomechanical Processing of High-strength Low-alloy Steels*, First Edition, Butterworth and Co. Ltd., London (1988).
- [44] L.E. Collins, F. Hamad, M. Kostic, T. Lawrence, Production of High Strength Line Pipe Steel by Steckel Mill Rolling and Spiral Forming, *International Symposium on Microalloyed Steels for the Oil and Gas Industry*, TMS, Orlando (2007).
- [45] L.E. Collins, D. Bai, F. Hamad, C. Xiande, High strength spiral linepipe for strain-based pipeline designs, *Proceedings of the International Offshore and Polar Engineering Conference*. (2007) 2969–2975.
- [46] M. Kulakov, Unpublished work, 2014.
- [47] C. Liu, S.D. Bhole, Challenges and developments in pipeline weldability and mechanical properties, *Science and Technology of Welding and Joining*. 18 (2013) 169–181.
- [48] L.Y. Lan, C.L. Qiu, D.W. Zhao, X.H. Gao, L.X. Du, Effect of single pass welding heat input on microstructure and hardness of submerged arc welded high strength low carbon bainitic steel, *Science and Technology of Welding and Joining*. 17 (2012) 564–570.
- [49] A.K. Pathak, G.L. Datta, Study of grain size and microhardness of submerged arc welded joint of AISI 1060 steel, *Science and Technology of Welding and Joining*. 10 (2005) 139–141.
- [50] K.E. Easterling, *Introduction to physical metallurgy of welding*, Butterworth-Heinemann Ltd., Oxford (1992).

- [51] M.J. Gaudet, The tensile properties and toughness of microstructures relevant to the HAZ of X80 linepipe steel girth welds, PhD Thesis, The University of British Columbia, Vancouver (2015).
- [52] D. Yapp, S.A. Blackman, Recent developments in high productivity pipeline welding, *Journal of the Brazilian Society of Mechanical Sciences and Engineering*. 26 (2004) 89–97
- [53] M. Maalekian, R. Radis, M. Militzer, A. Moreau, W.J. Poole, In situ measurement and modelling of austenite grain growth in a Ti/Nb microalloyed steel, *Acta Materialia*. 60 (2012) 1015–1026.
- [54] M. Shome, O.P. Gupta, O.N. Mohanty, Effect of simulated thermal cycles on the microstructure of the heat-affected zone in HSLA-80 and HSLA-100 steel plates, *Metallurgical and Materials Transactions A: Physical Metallurgy and Materials Science*. 35 (2004) 985–996.
- [55] B. de Meester, The Weldability of Modern Structural TMCP Steels., *ISIJ International*. 37 (1997) 537–551.
- [56] S. Moeinifar, A.H. Kokabi, H.R. Madaah Hosseini, Influence of peak temperature during simulation and real thermal cycles on microstructure and fracture properties of the reheated zones, *Materials and Design*. 31 (2010) 2948–2955.
- [57] N. Romualdi, Unpublished work, (2020)
- [58] R. Tafteh, Austenite decomposition in an X80 linepipe steel, M.A.Sc. Thesis, The University of British Columbia, Vancouver (2011).
- [59] I.D.G. Robinson, Grain growth and austenite decomposition in two niobium containing line pipe steels, M.A.Sc. Thesis, The University of British Columbia, Vancouver (2016).
- [60] Z. Zhu, J. Han, H. Li, Effect of alloy design on improving toughness for X70 steel during welding, *Materials and Design*. 88 (2015) 1326–1333.

- [61] Z. Zhu, J. Han, H. Li, Influence of heat input on microstructure and toughness properties in simulated CGHAZ of X80 steel manufactured using high-temperature processing, *Metallurgical and Materials Transactions A: Physical Metallurgy and Materials Science*. 46 (2015) 5467–5475.
- [62] Z.X. Zhu, M. Marimuthu, L. Kuzmikova, H.J. Li, F. Barbaro, L. Zheng, M.Z. Bai, C. Jones, Influence of Ti/N ratio on simulated CGHAZ microstructure and toughness in X70 steels, *Science and Technology of Welding and Joining*. 18 (2012) 45–51.
- [63] B.C. Kim, S. Lee, N.J. Kim, D.Y. Lee, Microstructure and local brittle zone phenomena in high-strength low-alloy steel welds, *Metallurgical Transactions A*. 22 (1991) 139–149.
- [64] Y. Zhou, T. Jia, X. Zhang, Z. Liu, R.D.K. Misra, Microstructure and toughness of the CGHAZ of an offshore platform steel, *Journal of Materials Processing Technology*. 219 (2015) 314–320.
- [65] L. Lan, C. Qiu, D. Zhao, X. Gao, L. Du, Microstructural characteristics and toughness of the simulated coarse grained heat affected zone of high strength low carbon bainitic steel, *Materials Science and Engineering A*. 529 (2011) 192–200.
- [66] N. Huda, A.R.H. Midawi, J. Gianetto, R. Lazor, A.P. Gerlich, Influence of martensite-austenite (MA) on impact toughness of X80 line pipe steels, *Materials Science and Engineering A*. 662 (2016) 481–491.
- [67] X. Yang, X. Di, X. Liu, D. Wang, C. Li, Effects of heat input on microstructure and fracture toughness of simulated coarse-grained heat affected zone for HSLA steels, *Materials Characterization*. 155 (2019) 109818.
- [68] C. Miao, C. Shang, X. Wang, L. Zhang, Microstructure and toughness of HAZ in X80 pipeline steel with high Nb content, *Jinshu Xuebao/Acta Metallurgica Sinica*. 46 (2010) 541–546.

- [69] M.P. Singh, K.S. Arora, N. Shajan, S.R. Pandu, M. Shome, R. Kumar, D. Shukla, Comparative analysis of continuous cooling transformation behaviour in CGHAZ of API X-80 and X-65 line pipe steels, *Journal of Thermal Analysis and Calorimetry*. 137 (2019) 1155–1167.
- [70] X. Ma, X. Li, B. Langelier, B. Gault, S. Subramanian, L. Collins, Effects of carbon variation on microstructure evolution in weld heat-affected zone of Nb-Ti microalloyed steels, *Metallurgical and Materials Transactions A: Physical Metallurgy and Materials Science*. 49 (2018) 4824–4837.
- [71] G. Huang, X.L. Wan, K.M. Wu, Effect of Cr content on microstructure and impact toughness in the simulated coarse-grained heat-affected zone of high-strength low-alloy Steels, *Steel Research International*. 87 (2016) 1426–1434.
- [72] G. Krauss, S.W. Thompson, Ferritic microstructures in continuously cooled low- and ultralow-carbon steels, *ISIJ International*. 35 (1995) 937–945.
- [73] S.W. Thompson, D.J. Colvin, G. Krauss, Austenite decomposition during continuous cooling of an HSLA-80 plate steel, *Metallurgical and Materials Transactions A: Physical Metallurgy and Materials Science*. 27 (1996) 1557–1571.
- [74] M. Hillert, The Formation of Pearlite, In: Zackay VF, Aaronson HI, editors. *Decomposition of austenite by diffusional processes*. New York: Interscience/John Wiley. (1962) 197–248.
- [75] J. Ba, L. Qing, Y. Ren, S. Zhang, H. Gao, Effects of continuous cooling rate on morphology of granular bainite in pipeline steels, *Journal of Iron and Steel Research International*. 27 (2020) 681-690.
- [76] M. Hillert, The Nature of Bainite, *ISIJ international*, 35 (1995) 34–40.
- [77] H.K.D.H. Bhadeshia, D.V. Edmonds, Mechanism of Bainite Formation in Steels., *Acta Metallurgica*. 28 (1980) 1265–1273.
- [78] H.K.D.H. Bhadeshia, *Bainite in Steels*, IOM Communications Ltd, London, Second edition (2001).

- [79] X.Y. Long, J. Kang, B. Lv, F.C. Zhang, Carbide-free bainite in medium carbon steel, *Materials and Design*. 64 (2014) 237–245.
- [80] N. Takayama, G. Miyamoto, T. Furuhashi, Effects of transformation temperature on variant pairing of bainitic ferrite in low carbon steel, *Acta Materialia*. 60 (2012) 2387–2396.
- [81] A. Lambert-Perlade, A.F. Gourgues, A. Pineau, Austenite to bainite phase transformation in the heat-affected zone of a high strength low alloy steel, *Acta Materialia*. 52 (2004) 2337–2348.
- [82] T.J. Headley, J.A. Brooks, A new BCC-FCC orientation relationship observed between ferrite and austenite in solidification structures of steels, *Metallurgical and Materials Transactions A: Physical Metallurgy and Materials Science*. 33 (2002) 5–15.
- [83] G. Krauss, *Steels: Processing, Structure, and Performance*, ASM International, Second Edition, Ohio (2015).
- [84] G. Krauss, A.R. Marder, The morphology of martensite in iron alloys, *Metallurgical Transactions*. 2 (1971) 2343–2357.
- [85] S.C. Wang, J.R. Yang, Effects of chemical composition, rolling and cooling conditions on the amount of martensite/austenite (M/A) constituent formation in low carbon bainitic steels, *Materials Science and Engineering A*. 154 (1992) 43–49.
- [86] W.A. Johnson, R.F. Mehl, Reaction kinetics in processes of nucleation and growth, *Trans. JWRI*. 135 (1939) 416-458.
- [87] M. Avrami, Kinetics of phase change. I: General theory, *The Journal of Chemical Physics*. 7 (1939) 1103–1112.
- [88] A.N. Kolmogorov, On the statistical theory of metal crystallization, *Bulletin of the Academy of Sciences of the USSR, Mathematics Series* (1937) 355–360.
- [89] J.W. Cahn, Transformation kinetics during continuous cooling, *Acta Metallurgica*. 4 (1956) 572–575.

- [90] M. Lusk, H.J. Jou, On the rule of additivity in phase transformation kinetics, *Metallurgical and Materials Transactions A: Physical Metallurgy and Materials Science*. 28 (1997) 287–291.
- [91] M. Militzer, R. Pandi, E.B. Hawbolt, Ferrite nucleation and growth during continuous cooling, *Metallurgical and Materials Transactions A: Physical Metallurgy and Materials Science*. 27 (1996) 1547–1556.
- [92] M. Militzer, E.B. Hawbolt, T.R. Meadowcroft, Microstructural model for hot strip rolling of high-strength low-alloy steels, *Metallurgical and Materials Transactions A: Physical Metallurgy and Materials Science*. 31 (2000) 1247–1259.
- [93] F. Fazeli, R. Tafteh, M. Militzer, W.J. Poole, Modeling the effect of Nb on austenite decomposition in advanced steels, *International Symposium on the Recent Developments in Plate Steels*. AIST, Warrendale, PA (2011) 343–350.
- [94] S.J. Jones, H.K.D.H. Bhadeshia, Competitive formation of inter- and intragranularly nucleated ferrite, *Metallurgical and Materials Transactions A: Physical Metallurgy and Materials Science*. 28 (1997) 2005–2013.
- [95] A. Hiramatsu, M. Umemoto, Y. Higo, Computer Modelling Austenite of Phase Transformation from Work-hardened, *ISIJ International*. 32 (1992) 306–315.
- [96] T. Garcin, M. Militzer, W.J. Poole, L. Collins, Microstructure model for the heat-affected zone of X80 linepipe steel, *Materials Science and Technology (United Kingdom)*. 32 (2016) 708–721.
- [97] S.H. Mohamadi Azghandi, V. Ghanooni Ahmadabadi, I. Raoofian, F. Fazeli, M. Zare, A. Zabett, H. Reihani, Investigation on decomposition behavior of austenite under continuous cooling in vanadium microalloyed steel (30MSV6), *Materials and Design*. 88 (2015) 751–758.
- [98] M. Militzer, M. Maalekian, T. Garcin, W.J. Poole, Microstructure evolution model for the HAZ of girth welds in X80 linepipe Steel, *Proceedings of the International Seminar on Welding of High Strength Pipeline Steels*. CBMM and TMS, San Antonio, USA (2013).

- [99] T. Jia, M. Militzer, Z.Y. Liu, General method of phase transformation modeling in advanced high strength steels, *ISIJ International*. 50 (2010) 583–590.
- [100] R.A. Vandermeer, Modeling diffusional growth during austenite decomposition to ferrite in polycrystalline FeC alloys, *Acta Metallurgica et Materialia*. 38 (1990) 2461–2470.
- [101] G.P. Krielaart, J. Sietsma, S. van der Zwaag, Ferrite formation in Fe-C alloys during austenite decomposition under non-equilibrium interface conditions, *Materials Science and Engineering: A*, 237 (1997) 216–223.
- [102] T.A. Kop, Y. van Leeuwen, J. Sietsma, S. van der Zwaag, Modelling the austenite to ferrite phase transformation in low carbon steels in terms of the interface mobility, *ISIJ International*. 40 (2000) 713–718.
- [103] F. Fazeli, M. Militzer, Application of solute drag theory to model ferrite formation in multiphase steels, *Metallurgical and Materials Transactions A: Physical Metallurgy and Materials Science*. 36 (2005) 1395–1405.
- [104] J. Sietsma, S. van der Zwaag, A concise model for mixed-mode phase transformations in the solid state, *Acta Materialia*. 52 (2004) 4143–4152.
- [105] M. Toloui, Microstructural evolution in the HAZ of X80 linepipe steel: Phase field modelling, PhD Thesis, The University of British Columbia, Vancouver (2015).
- [106] W.L. Roberts, *Flat Processing of Steel*, CRC Press, (1987).
- [107] R.A. Grange, Estimating critical ranges in heat treatment of steels, *Metal Progress*. 70:4 (1961) 73–75.
- [108] P.D. Hodgson, M.R. Hickson, R.K. Gibbs, Ultrafine ferrite in low carbon steel, *Scripta Materialia*. 40 (1999) 1179–1184.
- [109] K.W. Andrews, Empirical formulae for the calculation of some transformation temperatures, *Journal of the Iron and Steel Institute*. (1965) 721–727.

- [110] N. Isasti, D. Jorge-Badiola, M.L. Taheri, P. Uranga, Phase transformation study in Nb-Mo microalloyed steels using dilatometry and EBSD quantification, *Metallurgical and Materials Transactions A: Physical Metallurgy and Materials Science*. 44 (2013) 3552–3563.
- [111] L. Zhao, T.A. Kop, V. Rolin, J. Sietsma, A. Mertens, P.J. Jacques, S. van der Zwaag, Quantitative dilatometric analysis of intercritical annealing in a low-silicon TRIP steel, *Journal of Materials Science*. 37 (2002) 1585–1591.
- [112] ASTM E384 - 17, Standard Test Method for Microindentation Hardness of Materials, ASTM International. (2017) 1–40.
- [113] P. Cizek, B.P. Wynne, C.H.J. Davies, P.D. Hodgson, The effect of simulated thermomechanical processing on the transformation behavior and microstructure of a low-carbon Mo-Nb linepipe steel, *Metallurgical and Materials Transactions A: Physical Metallurgy and Materials Science*. 46 (2015) 407–425.
- [114] X.W. Chen, G.Y. Qiao, X.L. Han, X. Wang, F. Xiao, B. Liao, Effects of Mo, Cr and Nb on microstructure and mechanical properties of heat affected zone for Nb-bearing X80 pipeline steels, *Materials and Design*. 53 (2014) 888–901.
- [115] T. Furuhashi, H. Kawata, S. Morito, T. Maki, Crystallography of upper bainite in Fe-Ni-C alloys, *Materials Science and Engineering A*. 431 (2006) 228-236.
- [116] H.K.D.H. Bhadeshia, A rationalisation of shear transformations in steels, *Acta Metallurgica*. 29 (1981) 1117–1130.
- [117] J.Y. Maetz, M. Militzer, Y.W. Chen, J.R. Yang, N.H. Goo, S.J. Kim, B. Jian, H. Mohrbacher, Modeling of precipitation hardening during coiling of Nb-Mo steels, *Metals*. 8 (2018) 758.